University of Alberta

Erosion-corrosion of 304 Stainless Steel

By

Farzad Mohammadi

A thesis submitted to the Faculty of Graduate Studies and Research
in partial fulfillment of the requirements for the degree of

Doctor of Philosophy

In

Materials Engineering

Chemical and Materials Engineering

Spring 2011
Edmonton, Alberta

ABSTRACT

Stainless steel is one of the most commonly used materials in most industries. Excellent corrosion resistance of stainless steel is due to the formation of an oxide film on the surface (passive film), which protects the material from continuous corrosion attacks. When subjected to an attack combining corrosion and erosion, the passive film is damaged and thus, higher and unpredictable degradation rates are observed, which may result in costly consequences.

In the first part of this study a model was developed for erosion enhanced corrosion of 304 stainless steel. A new device was designed and constructed, which made possible the impingement of single particles on the surface of sample material at different impact velocities and angles. Based on the electrochemical response of material to the impact of single particles, a model was proposed that considered the number of the impacting particles on the surface. The predictions made by this model were later compared with the results of a slurry jet experiment, which was used to simulate the service conditions.

The second part of the research included the basic mechanical and electrochemical studies of the interactions occurring between the particle and material surface during the particle impact. This included the effects of different impact parameters such as coefficient of friction, impact angle, impact energy and particle angular velocity on depassivation of 304 stainless steel and its erosion-corrosion. A depassivation mechanism was proposed that considered a combined effect of the friction force and its effective path of action on the surface.

In the last part improving the erosion-corrosion properties of 304 stainless steel was tried based on the results of the second part of the study. Samples were cold rolled and the effect of hardness on the coefficient of friction was investigated, which in the second part was proven responsible for the depassivation of the surface. It was found that the coefficient of friction between the particles and the surface remains unchanged in different applied percentages of cold work. Also it was shown that work hardening is an effective method for increasing the resistance of the material to erosion-corrosion.

ACKNOWLEDGMENTS

I am appreciative for the brilliant guidance and support received from my supervisor, Dr. J. Luo. I also am grateful for the individuals who were in control of the laboratory instruments and services at the University of Alberta especially Mr. Dave Parlin and Mrs. Lily Laser.

The funding for this research work was provided by National Science and Engineering Research Council of Canada (NSERC), for which the author is grateful.

Above all, I am especially thankful for my wife Laleh, who is the joy of my heart. Without her inspiration, I would not be able to accomplish my thesis.

I also appreciate my family members, including my father Mohammad, my mother Shideh, my brothers Farshad and Farhood and my sister Mahshid who have invaluably supported me. In particular, I need to thank my parents and my older brother Farshad, who have constantly encouraged and supported me to continue with my studies to higher levels.

TABLE OF CONTENTS

TABLE OF TABLES

TABLE OF FIGURES

LIST OF SYMBOLS

a	scar radius, m
A_{nozzle}	nozzle area, m^2
C_d	particle drag coefficient
C_{sand}	sand concentration, wt%
d_{eff}	effective path of action for friction force, m
e	coefficient restitution
E	young modulus of elasticity, Pa
e_0	specific energy of crater formation, J/m^3
e_n	normal coefficient restitution
E_r, E^*	reduced modulus of elasticity, i/Pa
e_t	tangential coefficient restitution
F	Faraday constant, C/mol
F	force, N
$\overline{F}_n$	average normal force, N
$\overline{F}_t$	average tangential force, N
h	scar depth, m
HV	Vickers hardness
i	current density, A/m^2
I	current, A
K	radius of gyration, m
K_{el}	elastic energy stored in material, J
K_n	particle kinetic energy due to normal component of velocity, J
L	length, m
m	mass, kg
m_{RF}	mass of the removed film, kg
M_F	molecular weight of the passive film, g/mol
P_d	dynamic flow pressure, pa
P_n	normal impulse, kg.m/s

P_t tangential impulse, kg.m/s

Q_i charge due to single particle impact, C

Q_R repassivation charge, C

Q_t total charge, C

R radius of particles, m

SCE saturated calomel electrode

S_{RF} area of the removed film, m^2

t time, s

U_{pl} dissipated incident energy, J

V velocity, m/s, or volume, m^3

V_c volume of the scar, m^3

V_{cap} volume of the cap (scar), m^3

V_i impact velocity, m/s

V_{ni} normal component of the impact velocity, m/s

V_{nr} normal component of the rebound velocity, m/s

V_P particle velocity, m/s

V_r rebound velocity, m/s

V_{RF} volume of the removed film, m^3

V_{slurry} slurry velocity, m/s

V_{scar} volume of thescar, m^3

V_{tr} tangential component of the rebound velocity, m/s

V_{ti} tangential component of the impact velocity, m/s

V_y yield velocity, m/s

W_0 initial kinetic energy of the particle, J

W_c^0 weight loss due to corrosion, kg

W_e^0 weight loss due to erosion, kg

W_e^c mass loss due to corrosion enhanced erosion, kg

W_c^e mass loss due to erosion enhanced corrosion, kg

W_t total weight loss, kg

Y yield stress, pa

Z_{el} elastic approach, m

Z_{FF} number of charges transferred

α_s ratio of the depassivatedsurface of the film to the total surface of the scar

α_V ratio of the depassivated volume of the film to the total volume of the scar

ρ_P particle density, kg/m^3

δ relative approach, m

ΔK_f change of kinetic energy due to change of tangential component of velocity, J

ΔK_n change of kinetic energy due to change of normal component of velocity, J

ϑ_i impact angle, ^{o}

σ_y yield stress, pa

μ coefficient of friction

ρ_F fluid density, kg/m^3

ρ_{slurry} density of velocity, kg/m^3

σ conductivity, S/m

σ_c^0 error in corrosion calculation

σ_e^0 error in erosion calculation

σ_c^e error in erosion enhanced corrosion calculation

σ_e^c error in corrosion enhanced erosion calculation

σ_S error in synergy calculation

ω_r angular velocity, r/s

1 Introduction and literature review

In 2001, CC Technologies Laboratories, Inc. conducted a study in a cooperative agreement with FHWA and NACE International and it was reported that the total annual direct corrosion costs for the entire U.S. industries was about $276 billion which was 3.1% of U.S. gross domestic product ($8.79 trillion) [1].

Erosion - corrosion is a major problem in most industries especially those related to fossil fuel processing and transportation, such as chemical plants, propellant systems, hydraulic mining machinery and combustion systems [2-11]. The synergistic action of erosion and corrosion causes more damage to the materials being affected and can sometimes be twice as much they separately affect materials. The premature failure of materials in service caused by erosion - corrosion is mostly a result of this synergistic action. Industries spend millions of dollars annually to reduce, replace and fix the damages caused by erosion - corrosion. Oil sands processing facilities are no exception and erosion - corrosion is observed in many stages of the process. During the process, the tailing transportation pipes are highly influenced by erosion – corrosion. Some parts of these pipes are made of stainless steel, which is expected to have reasonable resistance to corrosion; however, the degradation rate of these pipes has proved to be much higher than expected. High corrosion resistance of stainless steel is due to the formation of a passive film on the surface, which extensively reduces the rates of the electrochemical reactions on the surface. Thus, if the passive film is intact, the material loss due to corrosion is negligible.

Figure 1.1 is a schematic diagram showing different combinations of erosion, corrosion and fluid flow. As it is apparent on the diagram, erosion-corrosion is the combination of erosion, corrosion and fluid flow on the surface. However, synergy of erosion and corrosion is usually treated by dividing it into two parts: erosion enhanced corrosion and corrosion enhanced erosion. The former represents the increase in the amount of corrosion that is caused by erosion while the latter shows the increase in the amount of erosion that is caused by corrosion.

When slurry flows in the pipes, floating particles, usually hard particles, impact the surface. If the impacting particles have enough kinetic energy, the passive film will be either completely removed or locally damaged due to the mechanical forces applied on the surface during the impact. This causes bare metal exposure to the environment, which leads to subsequent anodic dissolution and repassivation on the surface.

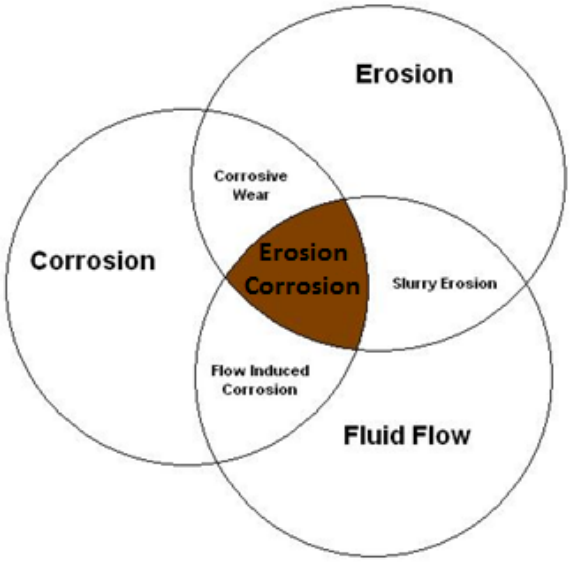

Figure 1-1 Schematic diagram of erosion, corrosion and fluid flow synergism.

Particle impacts can cause residual stresses on the surface. They can also increase the surface roughness, which promotes the anodic dissolution. In the case of 304 stainless steel, the repassivation process occurs in only a fraction of a second during which the anodic dissolution slows down. On the other hand, anodic dissolution influences the hardness of the surface and accordingly affects the erosion rate of the material. In order to obtain a better understanding of erosion – corrosion and make good predictions of material loss, effects of different parameters on erosion and corrosion and their synergism have to be studied.

The objective of this research is to do a basic study on the mechanism of erosion-corrosion of 304 stainless steel and to investigate the key parameters affecting the process of degradation of material, which will enable us to develop better strategies in controlling erosion - corrosion.

1.1 Corrosion

Substances are more stable in their lowest possible energy state, which is the reason behind many reactions in the universe. A metallic object reacts with the environment depending on the degree of its stability and forms compounds in which its energy state is the lowest possible. The occurrence of these reactions deteriorates the metal and the reaction products are called corrosion products. Since corrosion reactions include the transfer of electric charges, the corrosion reactions are electrochemical in nature and consist of the following three steps:

1- Adsorption of the reactants on the surface of the electrode.

2- Occurrence of the reactions on the surface.

3- Desorption of the reaction products from the electrode surface.

The overall process is controlled by the step with the slowest rate [12].

Depending on their ability to form passive films, metals and alloys can be divided into passive and active (non-passive) materials [13]. In active materials, the general anodic dissolution happens at all sites on the surface of the material and there are no preferred sites for reaction. But in passive materials, reaction rate on the surface is very low because of the existence of a protective layer on the surface (passive film) and corrosion may happen at sites with more reactivity and less resistance. Such localized reactivity can cause localized corrosion. Although the loss of material is much higher in an active material, localized corrosion is more dangerous, since the local area dissolves very quickly and is difficult to predict and control. In some passive materials if the

passive film is damaged or removed, repassivation occurs and the passive film reforms on the surface again.

1.1.1 Passive film

Passive films are protective films that form on the surface of the alloys when they react with the environment. Formation of these films is an electroless process, which happens in a relatively spontaneous manner. Existence of a passive layer on the surface reduces the rates of the reactions. The reduction in the reaction rate is caused by the very limited ionic and electronic conductivity of these films [14]. Previous studies on the electronic properties of the passive film on 304 stainless steel reveal that the film is made of two layers; the external layer mainly formed of iron oxide and hydroxide, which possess an n-type behavior and the p-type inner layer mainly composed of chromium oxide. Nickel oxide is shown to be equally present in both inner and outer layers [15-17]. Sato showed that a layer of hydroxides always exists on the oxide film/electrolyte interface for the requirement of stability [16, 17]. As described earlier, passive materials are always susceptible to localized corrosion. In the case of stainless steel, the implantation of cerium (Ce) has shown major improvements in the localized corrosion resistance, which is believed to be a result of cathodic reactions being inhibited by the formation and precipitation of insoluble $Ce(OH)_3$ at cathodic sites [18-21]. The thickness of the passive films on materials can be variable from monomolecular films in the case of gold to micrometer scale films in the case of aluminum [14]. In the case of stainless steel, the thickness of passive film is not more than a few nano meters.

It has been shown that in neutral solutions after one hour of passivation, the thickness of the film is linearly correlated to the applied potential during the passivation period [22, 23].

Since passive layers protect the material in corrosive conditions, it is important to be able to enhance their properties and increase their efficiency for service. In order to be able to perform such a task, a basic knowledge of the passive film formation mechanism and composition as well as its breakdown and reformation mechanisms is necessary. In more than 60 years that passive films have been studied, there is still no agreement among the scientists on their compositions, formation and breakdown mechanisms.

Scratched electrode is a common technique that is widely used in studying the passive film characteristics. In this technique the surface of the material is scratched using a sharp and hard tool that is usually made of diamond. The working electrode (sample) may be rotating or it may be fixed while the tip of the tool scratches the surface. By fixing the experimental parameters it is possible to measure the size of the scratch; however, defining the exact depassivated area can be complicated. Also great care must be taken to prevent damage to the tip of the indenter and to obtain consistent scratch results. While the surface of the sample is scratched the electrochemical signal is recorded and the repassivation kinetics can be studied from this curve. Also the scratched area can be studied and correlated to the electrochemical results [24-26]. In a potentiostatic experiment where the potential of the samples is held constant and the current is being recorded, a current transient peak is observed by

scratching the surface. Figure 1.2 shows a current transient caused by scratching the surface of 304 stainless steel in aqueous solution with near neutral pH.

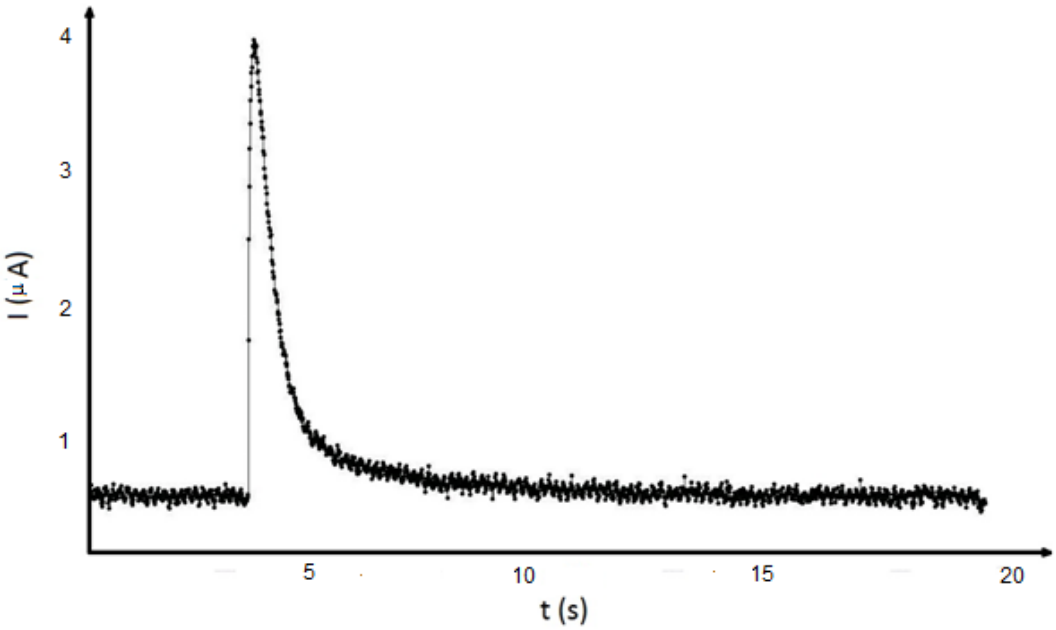

Figure 1-2 Sample current transient due to passive film breakdown in 304 stainless steel.

Two stages are observed in the repassivation curve. In the first period, current decay is very sharp, which is usually attributed to the first atomic layers of passive film formation. In the second period, the current decay is slower, which is often related to the growth of the passive film. Other methods such as abrading electrode [27-29], fractured wire [30, 31], drop weight [32, 33] and guillotined electrode [34] have been frequently used to study the repassivation behavior of materials.

1.1.2 Flow induced corrosion

The occurrence of corrosion consists of the transportation of reactants and products to and from the surface. If a reaction on the surface is dependent on the transportation rate, it will be highly influenced by the flow conditions and thus the corrosion rate. When fluid flow is present on the surface, the transportation rate of the reactants and products to and from the surface increases compared to steady state conditions. This type of increase in corrosion rate is called the flow induced corrosion [35].

1.2 Erosion

The word “erosion” is derived from the Latin word “rodene” that means wearing away gradually. This term is used in areas such as geology, politics and engineering. Erosion by solid particles is observed in many industrial processes and devices such as steam turbine blades and helicopter blades [36]. Erosion of ductile materials by small particles is the result of micro scale deformations on the surface, which eventually cause material detachment from the surface. On the other hand, erosion of brittle materials is a result of micro chipping and micro cracking of the surface due to the forces applied by particle during the impact.

Prior to 1958, many technical reports were published on problems in specific applications regarding material loss and wastage due to erosion by solid particles in special engineering conditions [37]. There were not many efforts on finding out how and why the material loss occurred. In 1958, Ian Finnie proposed a model for the erosion of

ductile metals [38]. Most of the papers published after Finnie followed the logic that he used in prediction of the erosion in ductile metals. However, the main problem with these models was that they were not able to predict the material wastage without using empirical constants that needed a considerable number of experiments to be defined. This was mainly due to the wrong assumption in all of these models where the micro-cutting mechanism was held responsible for the erosion. In 1975, scanning electron microscopy (SEM) was introduced for high resolution imaging. Later, it became possible for the scientists to observe the hills and grooves inside the craters produced by solid particle impacts, which were so small that they were impossible to observe by optical microscopy. SEM provided an opportunity for the scientists to study the mechanism of erosion in ductile and brittle materials. Based on the observations made by SEM, a platelet mechanism was later considered for erosion of ductile metals instead of the micro-cutting mechanism. Although the mechanism of erosion of materials became very well understood by scientists, it was even more difficult to provide a reasonable analytical model to predict the erosion rates, which is mainly due to the very complicated yet realistic nature of the proposed mechanisms.

1.2.1 Platelet mechanism

The micro-cutting mechanism that was proposed by Finnie considers that each particle is a cutting tool that acts on the surface. This mechanism was the accepted mechanism among scientists since it made possible prediction of the erosion phenomenon in many conditions. Later, the platelet mechanism was proposed by Levy

[39], which could explain both criteria that micro-cutting could and could not explain. Levy [40] plotted an erosion weight loss graph based on his experiments, which questioned the validity of the micro-cutting mechanism (Figure 1.3).

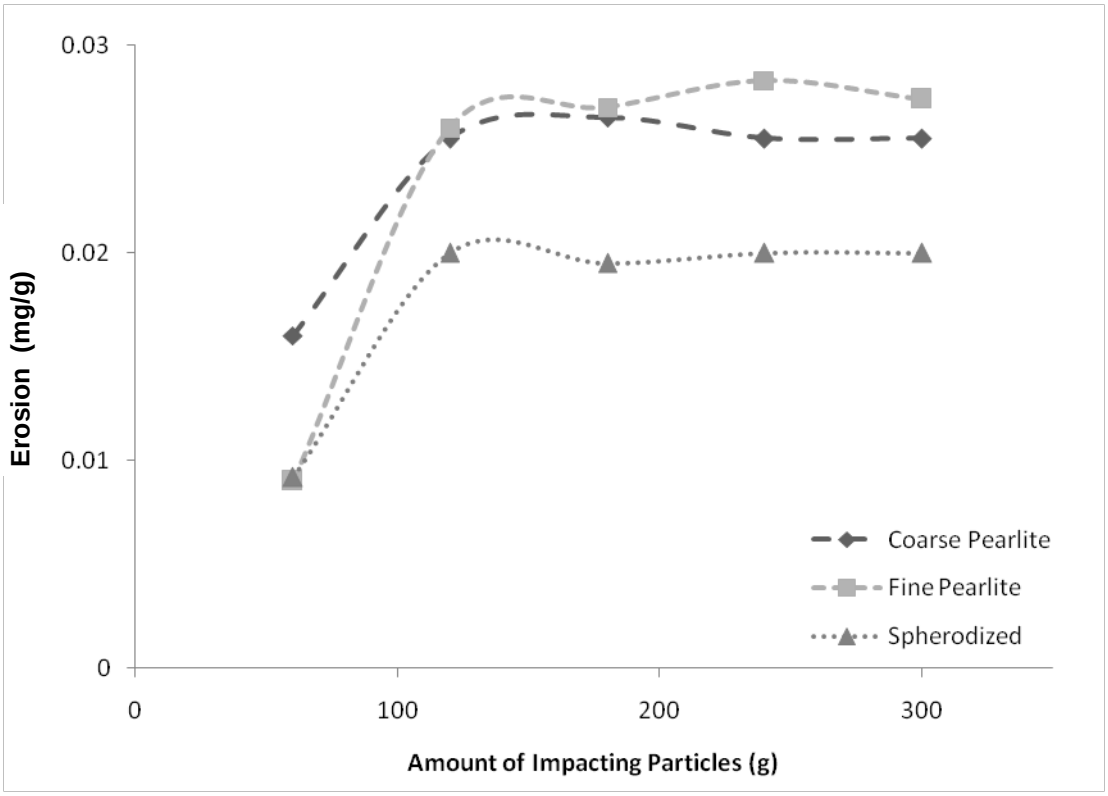

Figure 1-3 Erosion rate of 1075 steel as a function of solid loading in the slurry containing 240 µm SiC particles at 30.5 m/s and 30^{o} impact angle [40].

It can be observed that the first 60 g of the particles caused lower weight loss compared to the following 60 g of the particles that was added. Also, if the curves are extrapolated to zero erosion rates, there will still be some particles impacting the surface while causing no erosion. All of these indicated that the micro-cutting mechanism was not the main mechanism causing erosion on the surface. If micro-cutting was the major mechanism of erosion, the erosion rate of the first 60 g of particles on the surface should be higher than the subsequent batches because the effect of work hardening

caused by the initial cutting on the surface reduces the erosion rates of the following batches. Also the erosion rate should never be zero when particles are impacting the surface because they will start machining the surface upon their impact [36]. The results obtained from Figure 1.3 along with his observations and understandings from SEM pictures lead us to the platelet mechanism. This mechanism can be better described using Figure 1.4. As shown in the picture a platelet forms after the first particle impacts the surface, which is later beaten flat by the subsequent particles. The extensive strain that is caused on a platelet by multiple impacts causes the platelet to crack on its bent parts, which eventually leads to its removal from the surface. Levy also observed the formation of the platelets experimentally by using SEM mages [36]. To summarize it can be said that the initial platelets are extruded by primary particle impacts; later they are forged into a high strain condition by the following particles where they may crack or chip off from the surface. Other researchers have also found the platelet mechanism in good agreement with the experimental results [41].

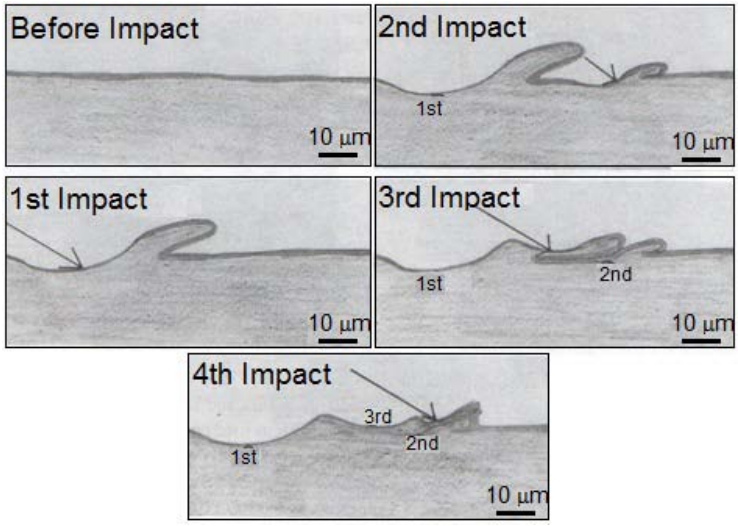

Figure 1-4 Schematic of platelet mechanism [36].

1.2.2 Effect of particle characteristics on erosion

Significant efforts have been made to understand the effect of test conditions such as particle characteristics on the erosion of materials. However, accurate analytical modeling of the erosion phenomenon is still not possible because of the limitations that apply to the test conditions in terms of controlling the experiment variables and applicability of the results of one experiment to another. Very small variations that may happen in an experiment and are not controllable may significantly influence the results. Therefore, many experimental or in service constants need to be derived for a successful analytical modeling of erosion. Particle impact angle, strength, shape and velocity are only a few of the parameters that affect the erosion rate of a material. Two of these parameters are discussed below.

1.2.2.1 Effect of particle's fracture toughness on erosion

Particle integrity and its strength are extremely important factors that affect the erosion rate. Many experiments have been previously conducted on the effect of different particles such as SiO_2, Al_2O_3 and SiC on the erosion rate [42-45]. Figure 1.5 shows the results of erosion experiments of cold rolled AISI 1020 steel [46]. Calcite, apatite, SiO_2, Al_2O_3 and SiC particles with angular shapes and sizes from 180-250 µm were used in the experiments and their hardness was used as a measure of their strength. It is observed that weak particles (calcite and apatite) cause much lower erosion rates. When the hardness of the particles reaches 700 HV the erosion rate becomes nearly constant and a further increase in the particle hardness has no effect.

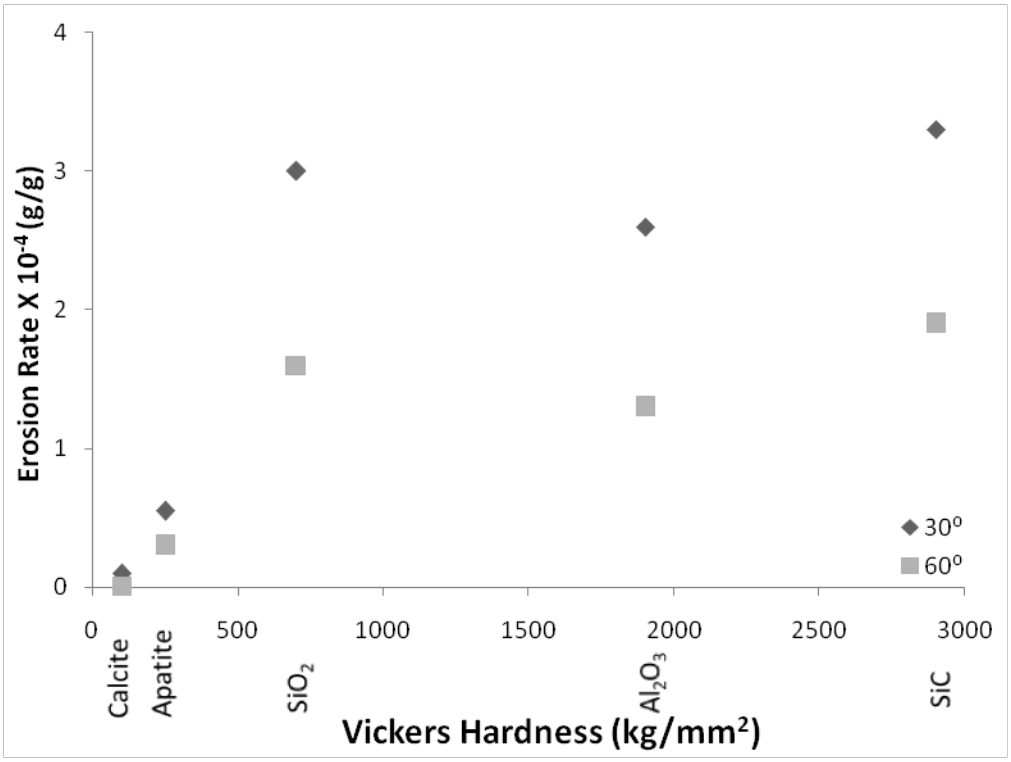

Figure 1-5 Dependence of erosion rate of 1020 steel on the particle hardness and impact angle [36].

1.2.2.2 Effect of particle size on erosion

Levy [36] used angular SiC particles to study the effect of particle size on erosion rate of 1018 steel at 20 m/s impact velocity. His metallographic observations indicated no significant change in the sharpness of the edges of the particles due to the change in their sizes. This means that the erosivity of the particles remains the same and the depth that they can penetrate the surface at the impact does not change with changing size. It is observed in Figure 1.6, which shows his experimental results, that the erosion rate is almost constant for all the particles and in different loadings.

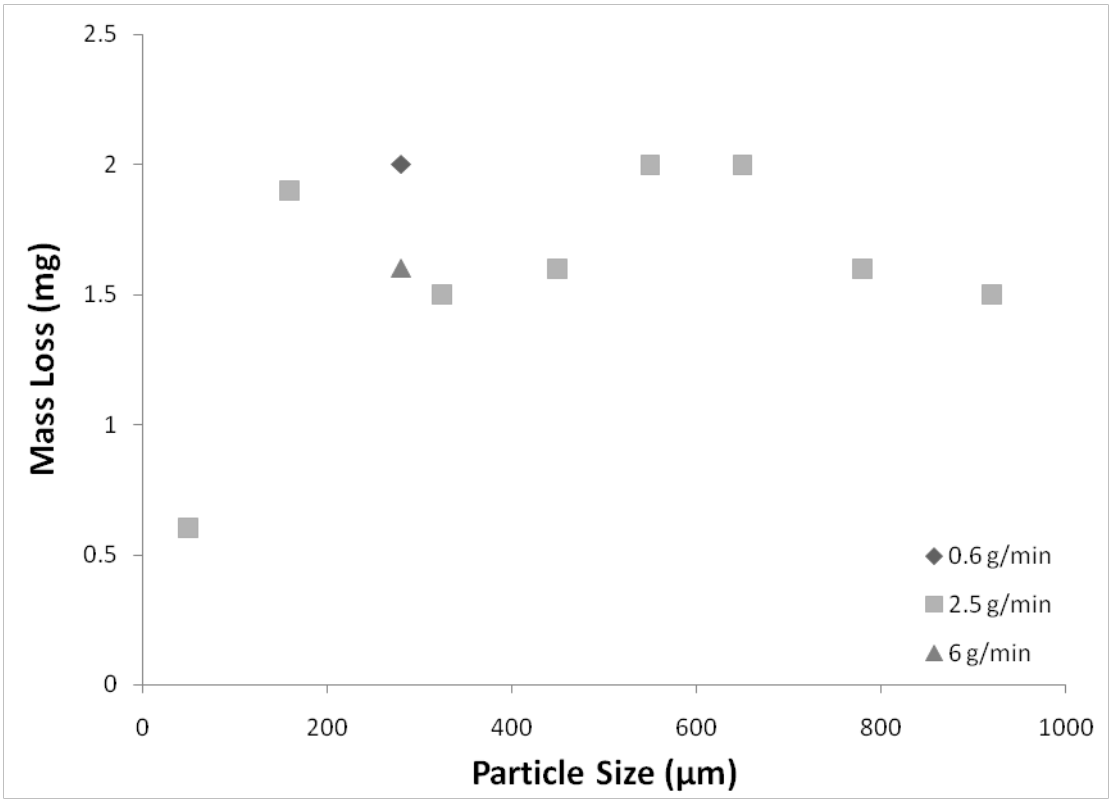

Figure 1-6 Dependence of erosion rate of 1018 steel on SiC particle size at 25^{o}C, 20 m/s impact velocity and 30^{o} impact angle [36].

1.2.3 Slurry erosion

Flow of liquids, which contain floating solid particles results in the erosion of the metals that are used in the transport or process systems in industries. The materials loss that is caused by this type of flow is called slurry erosion. The mechanisms with which slurry erosion damages the surface of ductile and brittle materials are the same as the platelet mechanism and the brittle micro fracture of the surfaces, respectively. Slurry erosion is affected by parameters such as solid particle size, solid loading, velocity, temperature and boundary lubrication. Effects of two of the above parameters will be described below.

1.2.3.1 Effect of boundary lubrication on slurry erosion

In order to study the effect of boundary lubrication of the carrier fluid on slurry erosion, Levy [36] used a long chain hydrocarbon, hexadecane, as the carrier fluid for coal particles. Adding a small amount of hexadecanoic acid, 0.5 mol%, to this carrier increases its boundary lubrication without significantly affecting its viscosity. The results of the addition of hexadecanoic acid to the carrier fluid are shown in Figure 1.7. It is apparent that increasing the boundary lubrication decreases the erosion rate on both 304 and A53 steels at room temperature.

1.2.3.2 Effect of temperature on slurry erosion

Figure 1.8 shows the erosion rate of A53 and 304 steel as a function of the test temperature [36]. Coal particles were used in a kerosene carrier fluid to perform the experiments. It is apparent that the erosion rate increases for both alloys as the test temperature increases. This can be mainly attributed to the change in the slurry viscosity rather than changes in the material's mechanical properties or erosion resistance. While the mechanical properties of the steels are not significantly altered by temperatures around 170^{o}C, viscosity of the carrier fluid is significantly decreased and the boundary layer characteristics are altered, which lead to an increased erosion rate of the material.

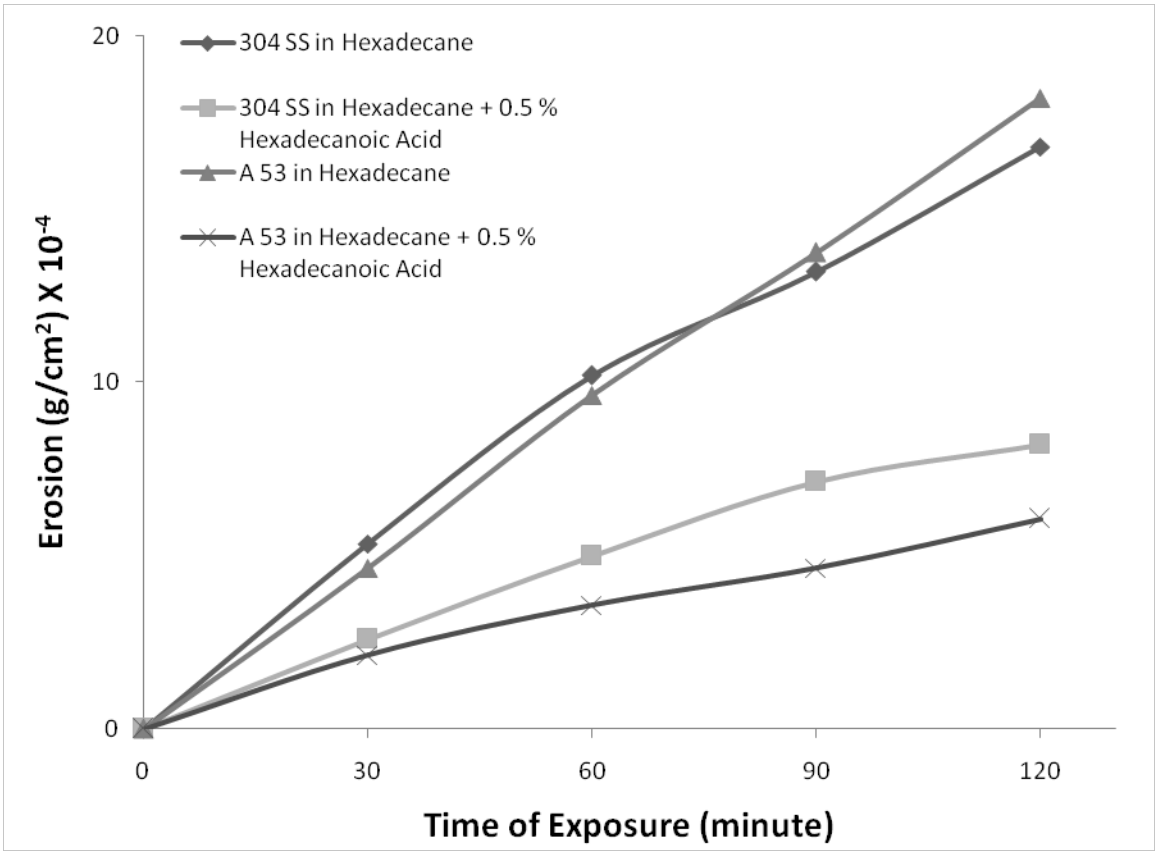

Figure 1-7 Effect of boundary lubrication on the erosion rate of A53 and 304 stainless steel with 30 wt% coal-200 mesh at 25^{o}C and 12 m/s [36].

1.3 Erosion-corrosion

Erosion-corrosion is the material wastage caused by simultaneous action of both mechanical forces and electrochemical reactions on the surface of the material. This can be often caused by liquid or slurry impingement, cavitations and solid particles in gas streams. The damage that is caused by erosion-corrosion is often much higher than the sum of the damages caused by each one of them separately. The increased damage is the result of a synergistic action between erosion and corrosion, in which erosive conditions promote corrosion and corrosive conditions enhance erosion.

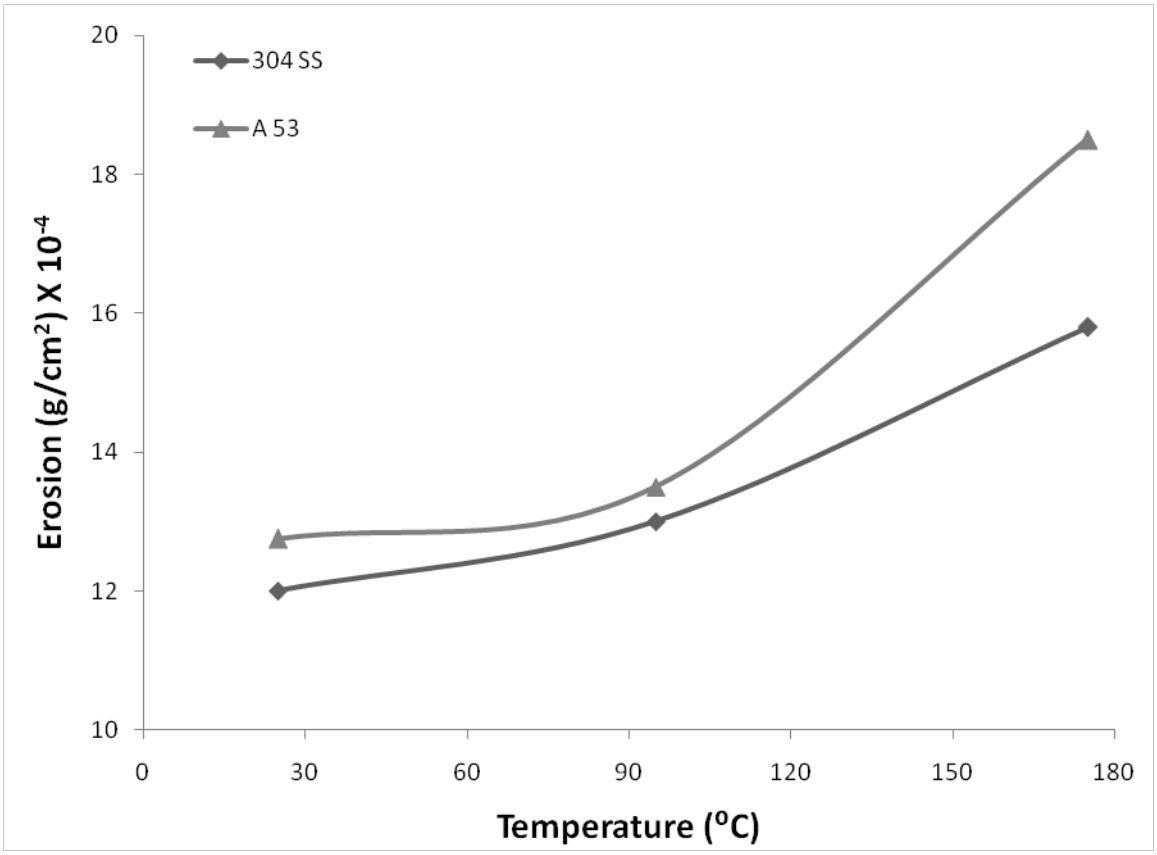

Figure 1-8 Effect of temperature on the erosion rate of 304and A53 steels eroded by 30 wt% Coal 200 mesh particles in Kerosene for 2 hours at 12 m/s. [36].

Erosion-corrosion mostly happens in turbulent flow conditions, which can be both single phase and multiphase flows [47-49]. The worst cases of erosion-corrosion are observed at elbows and bends or in compressors and turbines where a sudden change in the direction of motion of the flow causes disturbed turbulent flow conditions [50, 51]. Existence of the smallest imperfections on the surface or small surface defects such as pits created by corrosion may cause erosion-corrosion at turbulent flow conditions [52, 53]. Also if solid particles are present in the fluid flowing on the surface, erosion-corrosion can be very dangerous and can cause severe damage to the material.

1.3.1 Slurry erosion-corrosion of passive materials

As described earlier most of the corrosion resistant metals and alloys that are used in industries have protective oxide layers on their surface. These layers can be divided to two categories; the thick and diffusible layers that are made of corrosion products deposited on the surface and the thin and invisible layers that are called passive films. The main difference between the two types of films is that the former is more easily damaged and its reformation is slow while passive layers undergo more severe service conditions without severe damage and they reform very fast.

When passive materials are exposed to the flow of slurry, impacts of the floating solid particles can cause partial or complete damage to the passive film. This is due to the mechanical forces that are applied to the surface during the impacts. Once the passive film is damaged, the rate of the electrochemical reactions on the surface in the area of the damaged film increases. Anodic dissolution and repassivation are the two competitive processes happening simultaneously in the damaged area. Depending on the electric potential of the material, the carrier fluid and the flow conditions, either one of these processes can be dominant. In most cases, repassivation is the fastest occurring process and the passive film reforms in only a fraction of a second. However, during the course of repassivation, metal is also lost through anodic dissolution. If the rate of particle impacts on the surface is high, slurry erosion, then the metal loss during the repassivation period through electrochemical reactions becomes more significant. On the other hand, when the rate of the electrochemical reactions on the surface is

increased, these reactions (corrosion) affect the mechanical properties of the surface and influence the erosion resistance of the material.

The rate of slurry erosion-corrosion of materials is highly dependent on factors such as slurry velocity, impact angle, solid loading in the slurry, solid particle characteristics, relative hardness of the particle and material and mechanical properties of the material. In the following some of these parameters are described with more detail.

1.3.1.1 Effect of material's mechanical properties on erosion-corrosion

Mechanical properties such as ductility, strength, toughness and hardness of a specific material are very important in its resistance to erosion-corrosion. Among all of these characteristics, ductility and hardness have attracted more attention. It has been shown that for ductile materials, increasing the ductility of the material decreases its erosion-corrosion rate [36], which from the platelet mechanism point of view is completely consistent. The effect of a material's hardness on its erosion-corrosion resistance is rather controversial [54]. Some results indicate that harder materials are more resistant to erosion-corrosion [55-57] while others show opposite results [36, 58]. The effect of surface hardness on the erosion-corrosion is also dependent on the impact velocity and temperature since they define the regime in which erosion-corrosion occurs [36].

1.3.1.2 Effect of particle characteristics on erosion-corrosion

Relative hardness of the erodent particle to the eroded surface is extremely important in the extent of erosion-corrosion. Previous studies have shown that there is a

minimum hardness difference required between the particle and surface for the erosion-corrosion to take place [59, 60]. Torrance calculated a minimum of 1.25 for the ratio of erodent particle hardness to the matrix hardness above which the surface will be eroded [61].

On the other hand, not a significant difference in the material's corrosion rate was observed by researchers when the impacting particle size was altered [62]. However, the erosion rate of the material increases by increasing the impacting particle size. In the case of steels, there is a critical particle size above which no difference in the erosion-corrosion rate is observed. Also the angularity of the particles affects the erosion-corrosion rate of materials and the more angular in shape the particles are, the higher the erosion rate [36].

1.3.1.3 Effect of solid particle concentration in the slurry on erosion-corrosion

If we assume that the floating particles in the slurry have individual interactions with the surface upon their impact and they are not affected by other particles and conditions, then a linear correlation is expected between the erosion rate of the surface and the particle concentration in the slurry [36]. This is exactly the case for the experimental results with low particle concentrations where particles interact separately with the surface. However, when the particle concentration is increased as shown in Figure 1.9, the increase in the erosion rate does not show a linear correlation with particle concentration. This is due to particle-particle and particle-surface interactions.

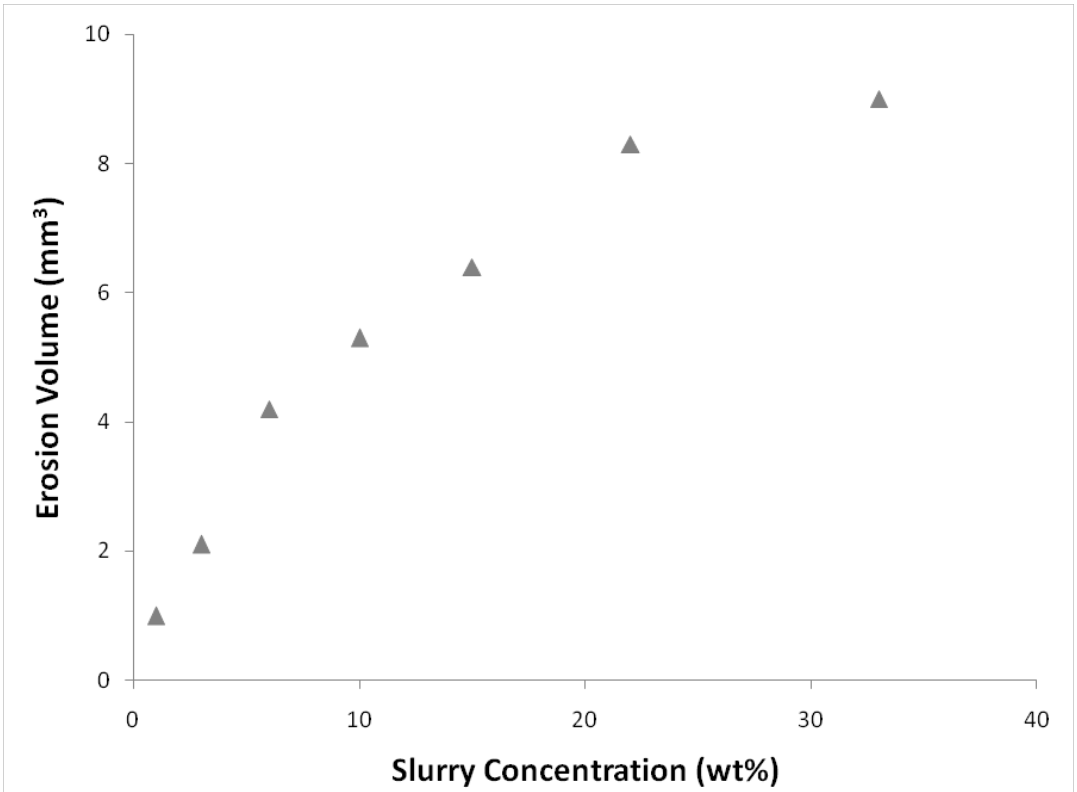

Figure 1-9 Effect of particle concentration on erosion rate [36].

For example, at higher particle concentrations it is more probable for a rebounding particle to interfere with an impacting particle's path and either reduce its impact energy or completely deflect it. These interferences result in lower erosion rates, which are experimentally observed [36].

1.3.1.4 Effect of impact angle on erosion-corrosion

Effect of impact angle on the erosion-corrosion of materials has been studied extensively by researchers [38, 63-70]. Finnie showed that ductile materials are eroded mostly at shallow angles while brittle materials are eroded most severely at normal angles of impact (Figure 1.10) [63]. The effect of impingement angle on 304L stainless

steel has been previously studied and it has been shown that the maximum erosion-corrosion rate happens at shallow impact angles around 30^{o} [36, 67, 70].

1.3.1.5 Effect of hydrodynamic characteristics on erosion-corrosion

As described earlier, the most significant effect of hydrodynamic parameters on corrosion is due to accelerating the mass transfer to and from the reaction surface. Both types of films (thick diffusible and passive) are prone to erosion-corrosion. It is not exactly known how the thick diffusible protective film is damaged in a turbulent flow of a single phase; however, the intensity of turbulence and its correlation with the shear stress that is applied on the surface are important factors that determine the extent of film breakdown [71, 72]. The passive films are not usually damaged by a single phase flow [73, 74]. The passage of slurries, however, damages both types of films. As described earlier erosion-corrosion of materials are affected by both velocity and impingement angle of the slurry. It has been previously shown that the impact of solid particles on the surface may be damped by the boundary layer on the surface [73, 75]. Both impact angle and velocity are extremely sensitive to the flow regime on the surface. The worst cases of erosion-corrosion in service are found in the areas with turbulent flow [76]. It has been shown that the impact angle in a non-disturbed flow condition is less than 5^{o} while a range of different impact angles are found in disturbed flow [76].

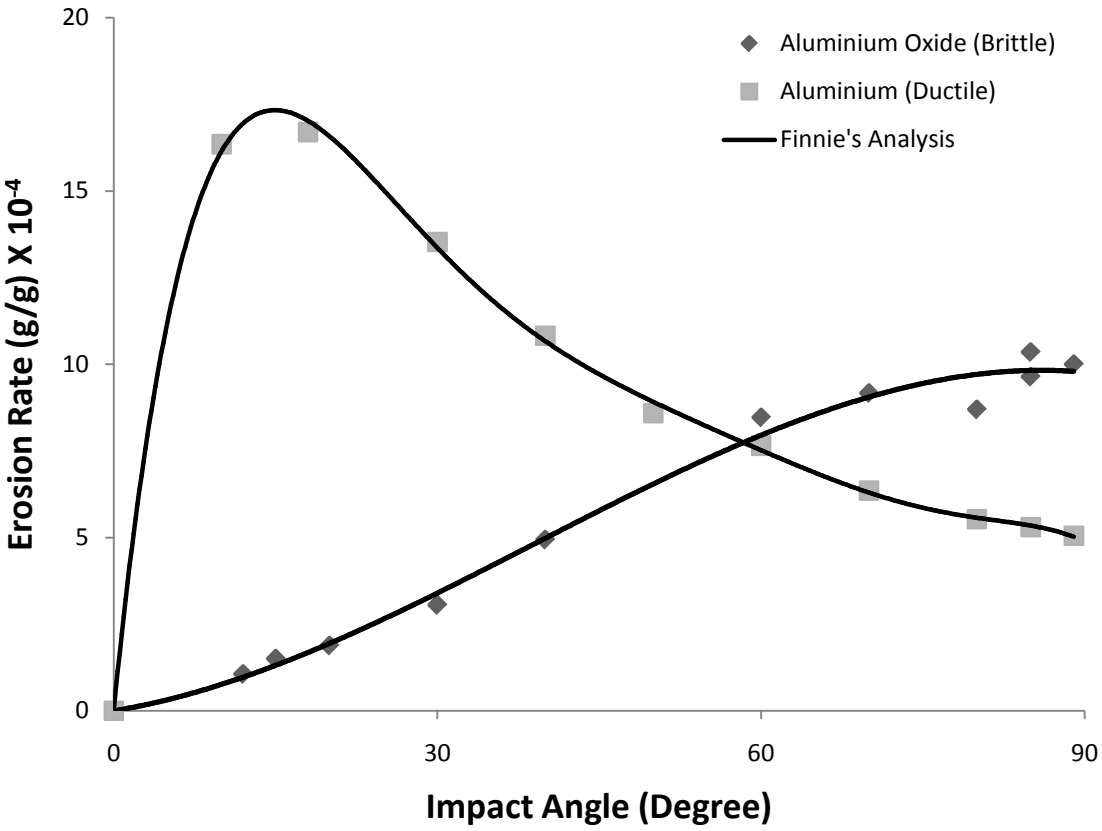

Figure 1-10 Effect of impact angle on erosion rate [63]

1.4 Suggested enhancement mechanisms in erosion-corrosion

Both erosion and corrosion enhance each other, which is why the rate of erosion-corrosion is much higher than the sum of their individual rates. It has been shown that although the corrosion rate itself is very small, the erosion rate of iron in a slurry containing NaOH is 20% more than its erosion rate in a slurry without NaOH [77]. A magnification factor was defined by Wood and Hutton as the ratio of the extent of material loss by erosion-corrosion to the extent of sum of the material losses by erosion and corrosion separately. They showed that in the case of austenitic stainless steels

subject to the flow of slurries with 2 wt% solid particle, this factor is in the range of 1.2 to 3 [78, 79]. Some of the mechanisms by which erosion and corrosion enhance each other are described below.

1.4.1 Corrosion enhanced erosion

1.4.1.1 Surface roughening

The difference in the reactivity of different parts of the surface of a material in a solution causes different dissolution rates on its surface. This non-uniformity phenomenon causes the corrosion surface to be somewhat rough. Postlethwaite used pipeline steel and silica sand slurry to study this effect [80]. He found that the surface roughness and erosion-corrosion rate of the material both decrease when corrosion inhibitors are added to the slurry. If the dimension of the surface roughness is comparable with the impacting particle diameter, the effect of corrosion on surface roughness and consequently erosion rate will be more pronounced. However, in most cases, the former is much smaller and its effect on erosion enhancement is not significant.

1.4.1.2 Preferential corrosion

As apparent from Figure 1.3 higher erosion is observed for the steel with fine pearlite microstructure while higher hardness is expected for this material comparing to the other two samples. This may be due to the anodic dissolution of the area of the matrix around the cementite phase, which makes the structure less strong. This area is

larger for the fine pearlite microstructure comparing to the other two samples. The difference in the reactivity on the surface is more significant in the case of metal matrix composites where the interface between the metal matrix and the hard particle is shown to be the most electrochemically active area on the surface [80, 81]. On the other hand, this interface plays a critical role in the mechanical properties of the composite because this is where the hard phase and the soft matrix are bound to each other. The dissolution in this preferred area lessens the strength of the bond between the hard particle and the matrix and causes the hard particle to come off more easily. Thus the erosion rate of the material will be increased.

1.4.1.3 Dissolution of work hardened surface layer and surface hardness degradation

When a material is under the flow of slurry, the constant impacts of the particles on the surface result in a thin work hardened layer on the surface, which is more resistant to erosion than the actual material itself. In the case of passive materials, this layer is protected by a passive film. Particle impacts during slurry flow damage the passive layer and thus the dissolution rate of the work hardened layer increases. This causes a thinner work hardened layer and lower erosion resistance of the material. Matsumura [77] showed that the continuous breakdown of the passive film causes an increase in dissolution rate, which results in the removal of the work hardened surface and increases the erosion rate. However, the applicability of this mechanism depends on two factors; the work hardenability of the material and the magnitude of dissolution rate comparing to the erosion rate.

Gua *et al.* used nano-indentation and studied the effect of corrosion on the surface hardness of carbon steel. They found that the surface hardness is decreased when anodic dissolution occurs on the surface [81].

1.4.1.4 Localized attack

The platelet mechanism suggested that the accumulation of strain on the roots of the platelets that are formed on the surface due to multiple particle impacts results in the breaking off of the flakes. Li *et al.* [82] suggested that the highly strained roots of the flakes are the preferred sites for corrosion to happen. This results in the formation of very sharp cracks at the roots. These cracks will propagate more quickly upon subsequent particle impacts and result in faster detachment of the flakes from the surface and higher erosion rates.

1.4.2 Erosion enhanced corrosion

1.4.2.1 Enhanced surface mass transport

Earlier it was described that the hydrodynamic properties of the slurry affect corrosion by increasing mass transfer rate on the surface. The existence of solid particles in the slurry cause more disturbances in the flow and thus increase the mass transfer rate on the surface [83, 84]. Zhou analyzed this effect and found that the corrosion rate in slurry with alumina particles is always higher than in a single phase flow [85].

1.4.2.2 Passive film breakdown

Many metals that are used in erosive corrosive applications are capable of formation of a passive layer on their surface. This film, as described earlier, reduces the rate of electrochemical reactions on the surface. When slurry flows on the surface, passive film can be damaged by particle impacts and the anodic dissolution reactions are accelerated. This mechanism is reported for many metals and their alloys such as stainless steel, titanium and cobalt alloys [86-90].

1.4.2.3 Increased pitting

When a metal is subject to the flow of slurry, each particle impact damages the surface oxide layer. This damaged area can later act as a preferred site for pitting. Burstein and Sasaki showed that the pitting potential of 304L stainless steel is reduced after a short period of exposure to slurry [91]. It is suggested that an increase in the surface roughness caused by particle impingements increases the number of suitable pitting sites on the surface [92, 93].

1.4.2.4 Increased roughness

It has been previously shown that the corrosion rate of a surface in a certain solution is influenced by the surface roughness usually in a way that the greater the surface roughness is, the greater the corrosion rate will be [94]. Flow of slurry on the surface of materials increases the surface roughness and thus higher corrosion rates are expected to be observed. Kim *et al.* studied the corrosion rate of titanium and stainless

steel alloys coated with TiN [94]. They showed that the surface with a lower roughness shows much better corrosion resistance. Also Sasaki studied the effect of roughness on the pitting potential of 304 stainless steel and found out that a surface with higher roughness has a lower pitting potential [91].

1.5 Common experimental methods for studying erosion-corrosion

1.5.1 Weight loss

Samples are weighed before and after experiments and the difference between the two values shows the amount of erosion-corrosion that occurred in a specific time. Since there might be corrosion or impurity deposits remaining on the surface of the samples after the tests, standard washing and weighing methods for different materials are provided by ASTM. Weight loss method is a very common method among erosion-corrosion specialists since it directly provides information about the extent of the material loss due to erosion-corrosion.

Weight loss cannot be used to determine the localized material loss, which is the biggest shortcoming of this method since it can only provide general material wastage information. While the general material loss may be small the localized attacks may still cause the material to fail. However, by using this technique and by applying certain conditions it is possible to separately measure the corrosion free erosion rates and erosion free corrosion rates. The latter can also be measured by electrochemical techniques.

1.5.2 Surface analysis

As described earlier, the platelet mechanism was only proposed after the SEM technique was introduced for high magnification imaging [39]. Since corrosion usually affects the surface layer of the materials, modern surface analysis techniques play a very important role in erosion-corrosion studies. X-ray diffraction, scanning electron microscopy, transmission electron microscopy, X-ray photoelectron spectroscopy and secondary ion mass spectroscopy are some of the techniques that are frequently used in erosion-corrosion studies.

1.5.3 Electrochemical techniques

Electrochemical techniques have the advantages of first providing *in situ* information on the current/voltage response of the material in specific experimental conditions, and second they provide the opportunity to control the reactions occurring on the surface. Two of the most commonly used electrochemical techniques are briefly described below.

1.5.3.1 Polarization diagrams

The deviation from the equilibrium potential of an electrochemical reaction is called polarization. Polarization diagrams of systems can be plotted by performing a cyclic polarization scan at a fixed voltage scan rate [95]. Critical data such as corrosion potential and corrosion current of a system can be easily calculated from the polarization diagram of that system. Also valuable information about the pitting

potential of a material in a specific environment can be obtained from its polarization diagram. At a certain applied potential the anodic current starts to increase sharply. This potential is called the breakdown potential at which pitting starts. Generally, a higher pitting potential is more favorable since the material is less susceptible to pitting.

In erosion-corrosion, polarization diagrams are often used to study the erosion enhanced corrosion behavior of the material. Two polarization diagrams of the material are plotted; one with a solution containing solid particles and the other with only the solution. Comparison between the two curves shows the enhancing effect of erosion on material corrosion rate.

1.5.3.2 Potentiostatic and galvanostatic diagrams

The two methods have been widely used in studying erosion-corrosion. It is known that in a specific electrochemical system there is a correlation between the current and potential. Therefore, if connected to a potentiostat/galvanostat, either one of the potential or current can be recorded while the other is controlled. Many researchers have previously used these techniques to investigate the enhancing effect of erosion on corrosion in different systems [96].

1.6 Common experimental setups for studying erosion-corrosion

There are usually three types of devices that are commonly used to perform erosion-corrosion experiments: rotating cylinder electrode (RCE), jet impingement and pipe flow loop. Before describing these three devices, it is worth mentioning that

despite many efforts done to correlate the results of different methods, it is still not possible to do so. This is due to different test conditions applied in each method such as different flow conditions, impact angles and mass transport conditions on the surface. Similar problems exist in correlating the results of these test methods with practical service conditions.

The RCE method is a relatively inexpensive method comparing to other methods. This method is often used in laboratories since it can be easily constructed. This device consists of a cylindrical container with a concentric cylindrical electrode installed inside it. While it is inexpensive and easy to construct, this method has one main disadvantage: the difficulty of maintaining a uniform particle distribution in the slurry during the test. Several modifications have been made to the system to obtain uniform particle distributions by increasing the turbulence of the flow; however, the hydrodynamic properties of the system and their effect on the results become very difficult to determine in a turbulent system.

A jet impingement system consists of a submerged nozzle impinging slurry to the surface of a sample. The main disadvantage of this method is that the shape of the crater constantly changes throughout the experiment and, therefore, the hydrodynamic properties in the vicinity of the crater, which make it difficult to obtain a uniform condition comparable to the service condition of the material. The main advantage of the system is that the angle and velocity of the impingement can be controlled. This method has been constantly used to study the effect of slurry impact angle on erosion-corrosion of different materials [97].

The pipe flow loop test device is a system very similar to the actual service [98]. This loop provides flow conditions and geometries very similar to the practical condition and thus provides very comparable results. The main disadvantage of this system is that the cost of preparation of this device is very high.

A common problem with all of the devices mentioned above is particle degradation during experiments since the erosion rates are only independent of time if the test conditions remain unchanged [99].

1.7 Impact of spherical particles on flat surfaces

After Hertz proposed a solution for the frictionless impact of elastic objects [100], the theoretical and experimental understanding of the particle-surface collision and its mechanism was significantly improved. These advancements started with incorporation of additional parameters to the common impact mechanics. For example, tangential loading and sliding of the objects were considered in the calculations [101, 102], friction forces at the contact patch were also included [103, 104], the effect of elastic wave propagation and the corresponding energy loss were studied [105, 106] and plastic deformation of the surface and particle were considered in the equations [3, 107]. In this section, first the elastic impact of a sphere on a flat surface is presented briefly and it is followed by a discussion on the elastic plastic impact condition.

1.7.1 Normal elastic impact

In 1882, Hertz used his static elastic contact theory and came up with a solution for the elastic impact of the objects [100]. He assumed that elastic wave propagation causes negligible energy loss and also that the total mass of the impacting objects move with the same velocities. In addition to these assumptions, the deformation was assumed to be only in the vicinity of the contact patch.

Here, it is necessary to introduce the concept of coefficient of restitution, which represents the amount of energy that is dissipated during the impact of objects and is defined as the ratio of the rebound and impact velocities. This argument is based on the Hertzian theory of impact and his assumption that the coefficient of restitution is unity, which means that the impact and rebound velocities are equal.

Hertz assumed two spherical particles with masses m_1 and m_2 approaching each other on a line that connects their centers with no spin and at velocities V_1 and V_2. If δ is their relative approach then:

$$V = V_2 - V_1 = \frac{d\delta}{dt} \qquad (1.1)$$

where V is the relative velocity of the two centers of the particles. After the particles first contact the contact force can be written as:

$$F = m_1 \frac{dV_1}{dt} = -m_2 \frac{dV_2}{dt} \qquad (1.2)$$

with the definition of m* as:

$$\frac{1}{m^*} = \frac{1}{m_1} + \frac{1}{m_2} \qquad (1.3)$$

one can write:

$$F = -m^* \frac{dV}{dt} = -m^* \frac{d^2\delta}{dt^2} \quad (1.4)$$

In his static elastic contact, Hertz defined the correlation of force and approach as:

$$F = \frac{4}{3} E^* R^{*1/2} \delta^{3/2} \quad (1.5)$$

E* and R* are defined like m* and it is obvious that in the case of the impact of a spherical particle against a flat surface these values are equal to that of the spherical particle. Also the relative velocity of approach will be equal to the particle impact velocity at each time. Combining Equations 1.4 and 1.5 for the case of the impact of a spherical particle against a flat surface results in:

$$m \frac{d^2\delta}{dt^2} = -\frac{4}{3} E^* R^{*1/2} \delta^{3/2} \quad (1.6)$$

knowing that at t=0 the impact velocity is the initial particle velocity V_i and that when the relative velocity is zero the relative approach, δ, is at its maximum value, Equation 1.6 will result in:

$$\delta_{max} = \left(\frac{15 m {V_i}^2}{16 E^* R^{\frac{1}{2}}}\right)^{2/5} \quad (1.7)$$

Further integration of Equation 1.6 results in the definition of the contact time during the impact [108]. It has been shown that the assumption of insignificancy of the energy loss by elastic waves is only valid if the thickness of the plate is much larger than the contact area [109, 110]. This means that higher energies are dissipated by elastic wave propagation when a thin plate is impacted by a particle. It was also reported that the contact time during the impact depends on the impact velocity. Both in the elastic impact regime and in the elastic plastic impact regime the contact time is decreased

when the impact velocity is increased [111-112]. Figure 1.11 shows the contact time during the impact as a function of impact velocity.

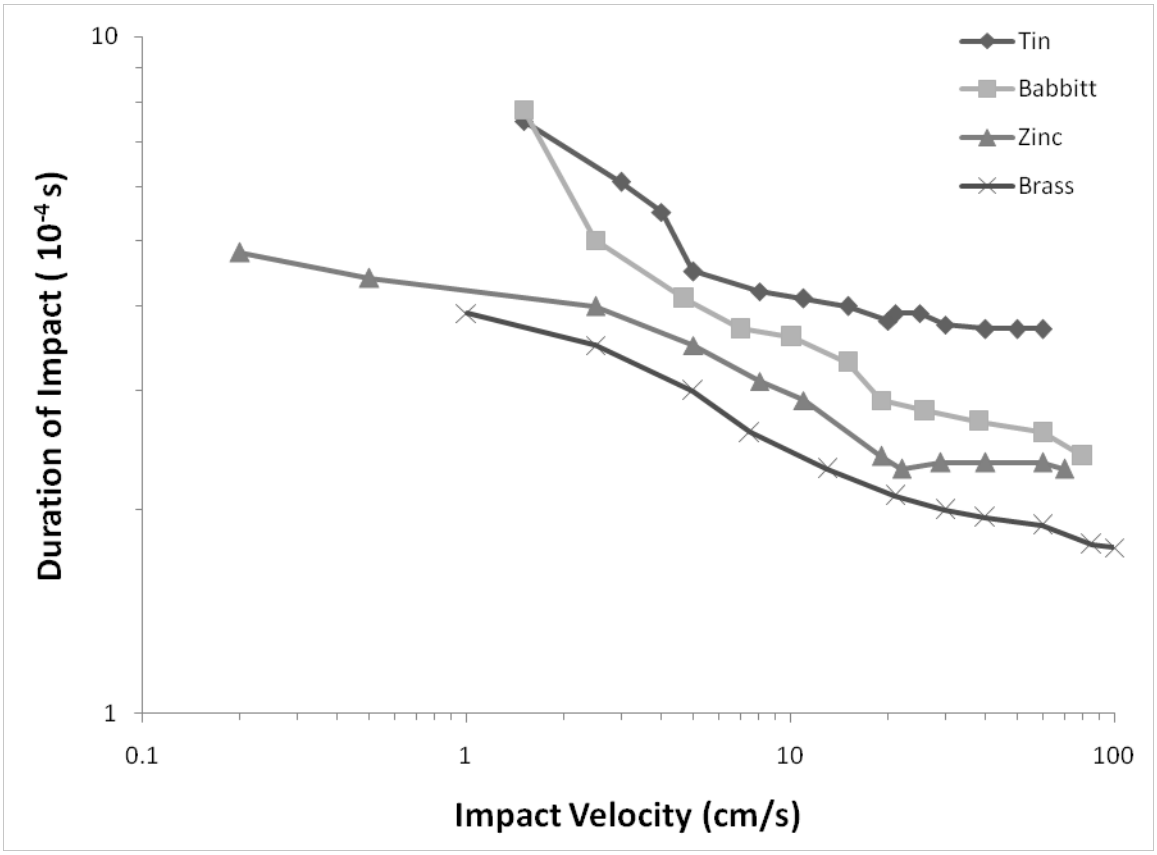

Figure 1-11 Contact time during the impact as a function of impact velocity [113].

1.7.2 Oblique elastic impact

During the oblique impact of the elastic objects, there is a high probability of slipping and sliding between the two surfaces, which makes it very difficult to define the impact characteristics. Mindlin *et al.* showed that the impact condition at any moment during the impact depends on both that moment loads and the history of loading before that moment [102]. On the other hand, Johnson showed that the load-displacement

correlation in the normal and tangential directions can be dealt with separately and that their effect on each other is very small and negligible [110].

Maw *et al.* showed that for normal impact angles sliding does not occur during the impact; however, when the impact angle is decreased to shallower angles the sliding occurs at the beginning and end of the contact while slipping occurs in between. When the impact angle is very low, sliding happens all along the contact period [114]. Also Thornton performed computer simulations and reported that the results are in good agreement with Maw *et al.* results [115, 116].

Based on the experimental results in the elastic impact velocity range, it can be concluded that although Hertzian theory is not completely correct and accurate, it can provide a good approximation for the elastic impact of the particles. However, at higher impact velocities where plastic deformation occurs during the impact, necessary modifications were needed to the Hertzian theory since it does not consider plastic deformation at all.

1.7.3 Elastic plastic impact

Bitter showed that the elastic plastic process of the impact of objects can be divided into three stages [2]. First, there is an elastic period, which is the duration between the moment that the objects touch each other and the moment that the force between them reaches the elastic limit or the yield point of the softer object. This is a pure elastic stage and can be dealt with by Hertzian theory. The next stage starts when plastic deformation starts and ends when the objects have no relative movement while

still in contact. The last stage is when the elastic energy that is stored in the objects during the first two elastic and plastic periods is released and transferred to the objects in the form of their rebound velocity. When the impact velocity increases past the elastic yielding limit of the materials, the coefficient of restitution decreases from unity. Elastic yielding limit of a material is reached when the impact velocity exceeds the elastic yield limiting velocity, V_y [117]:

$$V_y = \left(\frac{\pi}{2E^*}\right)^2 \left(\frac{2}{5\rho_P}\right)^{1/2} {\sigma_y}^{5/2} \qquad (1.8)$$

where ρ_P is the density of the particle and σ_y is the yield stress of the target material. Thus, the stored energy in the material due to plastic deformation at the beginning of the second stage is:

$$K_{el} = \frac{1}{2} m {V_y}^2 \qquad (1.9)$$

Also by using the Hertzian theory of elastic impacts the relative approach of the particle and the surface is:

$$\delta_y = R\left(\frac{\pi\sigma_y}{2E^*}\right)^2 \qquad (1.10)$$

where R is the radius of the impacting particle. Johnson *et al.* developed a model by assuming a full plastic state during the impact and calculated the coefficients of restitution and studied their dependence on the impact velocity [110]. They showed that the normal coefficient of restitution is correlated to the impact velocity by a power of -1/4. Rogers and Reed proposed a model based on the Bitter calculations [107]. They assumed that the only mechanism that consumes energy during the impact is plastic deformation on the surface and that the third stage of the impact is completely elastic.

Wall *et al.* [118] compared the results of Rogers and Reed with experimental results and found some inconsistencies. Therefore, they modified the model and in the calculations they replaced the static yield stress by dynamic yield stress of the material, which improved the existing model so that the experimental and theoretical results matched very well. Figure 1.12 shows the both models in comparison with the experimental results.

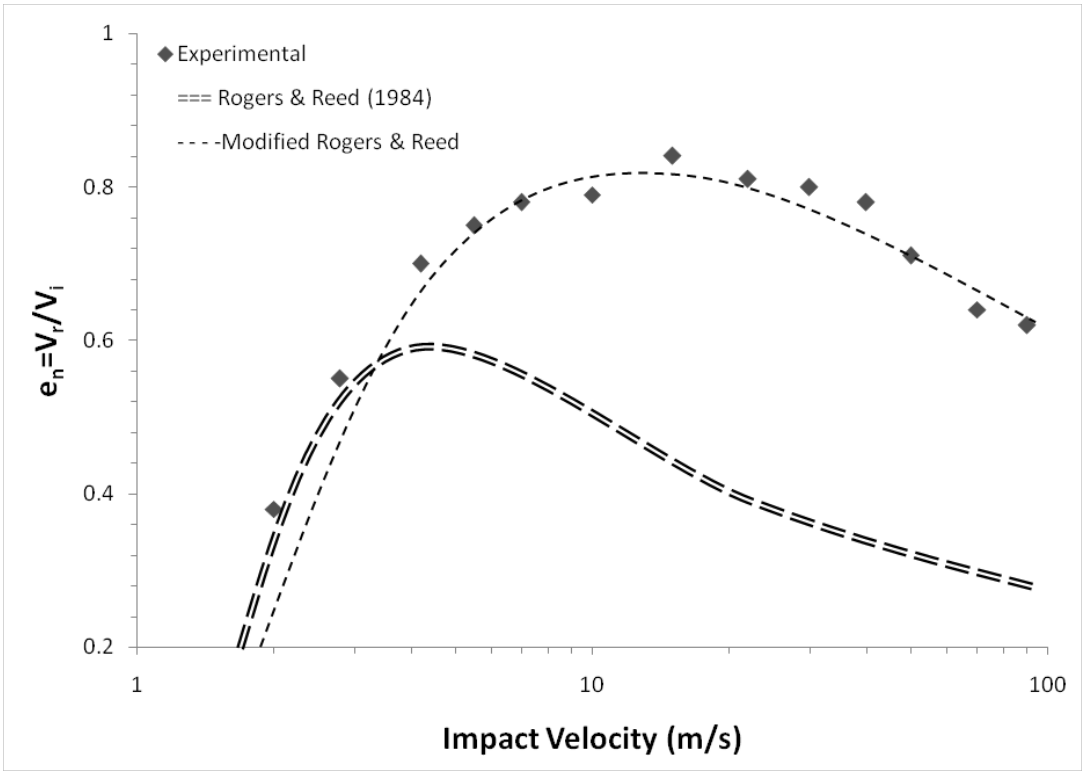

Figure 1-12 Normal coefficient of restitution as a function of impact velocity [107, 118].

1.8 Velocity of solid particles in fluid flow

A solid particle introduced to a fluid stream can have quite different direction of motion and velocity than the containing fluid. Also obstacles in the fluid flow path can cause different changes of direction especially for smaller particles. Tilly defined an

effective spherical size for randomly shaped particles and analyzed their velocities after they were introduced to fluid streams [119].

Consider a particle with diameter *d* and mass density of ρ_P that is introduced to a fluid stream with a density of ρ_F. If the velocity of the particle is V_P and the velocity of fluid is V_F then the equations of motion of the particle in two dimensions can be written as:

$$\frac{\pi d^3 \rho_P}{6}\frac{\mathrm{d}V_x}{\mathrm{d}t} = \frac{C_\mathrm{d}}{2}\rho_\mathrm{F}\frac{\pi d^2}{4}\,(Vx_\mathrm{P} - Vx_\mathrm{F}) \qquad (1.11)$$

$$\frac{\pi d^3 \rho_P}{6}\frac{\mathrm{d}V_y}{\mathrm{d}t} = \frac{C_\mathrm{d}}{2}\rho_\mathrm{F}\frac{\pi d^2}{4}\,(Vy_\mathrm{P} - Vy_\mathrm{F}) \qquad (1.12)$$

where C_d is the particle drag coefficient and can be calculated through either empirical or theoretical equations [120].

Finnie assumed a one dimensional motion for a spherical particle that is introduced in a fluid stream at one point and impacts the surface of an obstacle at distance *X* from its introduction point and calculated the particle impact velocity [121]. In this case Equation 1.11 can be written as:

$$\frac{\mathrm{d}(V_\mathrm{F} - V_\mathrm{P})}{\mathrm{d}t} = -K(V_\mathrm{F} - V_\mathrm{P})^2 \qquad (1.13)$$

where

$$K = \frac{3C_\mathrm{d}\,\rho_\mathrm{F}}{4\rho_\mathrm{P} d} \qquad (1.14)$$

If the initial condition of t=0 and V=0 is considered then:

$$V = \frac{KV_F{}^2 t}{1+KV_F t} \qquad (1.15)$$

Application of another initial condition of t=0 and X=0 results in:

$$x = \frac{1}{K}(KV_\mathrm{F}t - \ln[1 + KV_\mathrm{F}t]) \qquad (1.16)$$

Using Equations 1.11 to 1.16 it is possible to calculate the velocity of a spherical particle in a fluid stream at any point of its path. A visual basic code was developed and is presented in appendix A based on the above calculations. This code was used by the author to design a new device for studying erosion-corrosion of 304 stainless steel, which is described in the following chapter.

1.9 Current status in erosion-corrosion research and objectives

Significant progress is observed in the field of erosion-corrosion, mostly in the determination of the important factors. However, the extensive number of the relevant parameters influences the prediction of the material degradation rate in practical conditions. On the other hand, the differences between the experimental results obtained through different methods in comparison with each other and with practical conditions add to the difficulty of providing accurate and useful predictions. Further studies on the erosion-corrosion phenomenon and the important parameters are necessary in order to increase the extent of our knowledge in the field and to provide a firm basis for the prediction of material deterioration rates in practice.

Studying the particle-surface interactions during slurry erosion-corrosion can provide us an insight into what basically goes on in the erosion-corrosion of passive materials. This can be extremely helpful in understanding the mechanisms by which erosion and corrosion enhance each other. Also this information can be used in the development of new models and better material loss predictions. These purposes were among the main objectives of the present work. Therefore, a device was designed and

constructed for single particle impingement, which provided the opportunity of studying particle-surface interactions both mechanically and electrochemically. The next goal of this project was to use the information obtained from the particle impacts to study the mechanism of the damage that is caused on the surface by these impacts and to develop a model based on this information that could reasonably predict the erosion-corrosion of the materials in practical conditions. Finally, it was suitable to use the particle surface interaction information to study common methods that are used for enhancing erosion-corrosion properties of the materials.

1.10 References

[1] FWHA, Corrosion costs and preventive strategies in the united states, Publication no. FWHA-RD-01-156.

[2] J.G.A. Bitter, A study of erosion phenomena part I, Wear 6 (1963) 5.

[3] J.G.A. Bitter, A study of erosion phenomena: Part II, Wear 6 (1963) 169.

[4] H. Neilson and A. Gilchrist, An experimental investigation into aspects of erosion in rocket motor tail nozzles, Wear 11 (1968) 123.

[5] I.G. Wright, High temperature erosion in coal combustion and conversion processes: Review, Mater. Sci. Engg. 88 (1987) 261.

[6] W.J. Tomlinson, R. T. Moule and G. N. Blount, Cavitation erosion in a dilute emulsion, Tribology International 20 (1987) 150-152.

[7] G.F. Truscott, A literature survey on abrasive wear in hydraulic machinery, Wear 20 (1972) 29-50.

[8] J. Stringer, Practical experience with wastage at elevated temperatures in coal combustion systems, Wear 186-187 (1995) 11-27.

[9] A.V. Levy, The erosion-corrosion of tubing steels in combustion boiler environments, Corros. Sci. 35 (1993) 1035-1039, 1041-1043.

[10] B. Wang, Erosion-corrosion of thermal sprayed coatings in FBC boilers, Wear 199 (1996) 24-32.

[11] C.G. Scott, A. T. Riga and H. Hong, The erosion-corrosion of nickel-base diesel engine exhaust valves, Wear 181-183 (1995) 485-494.

[12] M.G. Fontana, Corrosion engineering: third edition, McGraw-Hill, New York, 1987.

[13] J.R. Davis (Editor), Corrosion: understanding The Basics, ASM international, Materials Park, Ohio, 2000.

[14] J.W. Schultze and; A. W. Hassel, Encyclopedia of electrochemistry: corrosion and oxide films, Willey, Weinheim, 2003.

[15] M.D. Cunha Belo, N. E. Hakiki and M. G. S. Ferreira, Semiconducting properties of passive films formed on nickel–base alloys type Alloy 600: influence of the alloying elements, Electrochim. Acta, 44 (1999) 2473-2481.

[16] N. Sato, Toward a more fundamental understanding of corrosion processes, Corrosion 45 (1989) 354-368.

[17] B.T. Lu, B. Peng, J.L. Luo and Y.C. Lu, Passivity of nuclear steam generator tube alloy in lead-contaminated crevice chemistries with different pH, Proc. 13th Int. Conf. Env. Deg. Met. Nucl. Sys. (2007) 172, Whistler, BC, Canada.

[18] S. Virtanen, M.B. Ives, G.I. Sproule, P. Schmuki and M.J. Graham , A surface analytical and electrochemical study on the role of cerium in the chemical surface treatment of stainless steels, Corros. Sci. 39 (1997) 1897-1913.

[19] C.B. Breslin, C. Chen and F. Mansfeld, The electrochemical behaviour of stainless steels following surface modification in cerium containing solutions, Corros. Sci. 39 (1997) 1061-1073.

[20] Y.C. Lu and M. B. Ives, Chemical treatment with cerium to improve the crevice corrosion resistance of austenitic stainless steels, Corros. Sci. 37 (1995) 145-155.

[21] Y.C Lu and M.B Ives, The improvement of the localized corrosion resistance of stainless steel by cerium, Corros. Sci. 34 (1993) 1773-1781, 1783-1785.

[22] B. Elsener and A. Rossi, XPS investigation of passive films on amorphous Fe-Cr alloys, Electrochim. Acta 37 (1992) 2269-2276.

[23] C.M. Abreu, M. J. Cristobal, X. R. Novoa, G. Pena and M. C. Perez, Characterisation of the electrochemical behavior of cerium implanted stainless steels, Electrochim. Acta 47 (2002) 2215-2222.

[24] G.T. Burstein and D. H. Davies, The electrochemical behavior of scratched iron surfaces in aqueous solutions, J. Electrochem. Soc. 128 (1981) 33-39.

[25] F.P. Ford, G. T. Burstein and T. P. Hoar, Bare surface reaction rates and their relation to environment controlled cracking of aluminum alloys, J. Electrochem. Soc. 127 (1980) 1325-1331.

[26] D.J. Lees, T. P. Hoar, Use of the scratching electrode technique to interpret the stress corrosion cracking behavior of α-brass in ammoniacal copper sulphate solutions, Corros. Sci. 20 (1980) 761-771, 773-780.

[27] T. Kodama and J. R. Ambrose, Effect of molybdate ion on the repassivation kinetics of iron in solutions containing chloride ions, Corrosion 33 (1977) 155-161.

[28] S.-I. Pyun and M. Hong, The repassivation kinetics of pure nickel in a Na2SO4 solution using abrading electrode technique, Electrochim. Acta 37 (1992) 2437-2442.

[29] J.-J. Park, S. -I. Pyun, K. -H. Na, S. -M. Lee, and Y. -T. Kho, Effect of passivity of the oxide film on low-pH stress corrosion cracking of API 5L X-65 pipeline steel in bicarbonate solution, Corrosion 58 (2002) 329-337.

[30] D.G. Kolman and J. R. Scully, On the repassivation behavior of high-purity titanium and selected α, β and α+β titanium alloys in aqueous chloride solutions, J. Electrochem. Soc. 143 (1996) 1847-1860.

[31] T.R. Beck, Electrochemistry of freshly generated titanium surfaces: rapid fracture experiments, Electrochim. Acta 18 (1973) 815-827.

[32] R.B. Diegle and D. A. Vermilyea, A study of transient corrosion in the iron-caustic system by use of a drop weight apparatus, J. Electrochem. Soc. 122 (1975) 180-188.

[33] T.M. Angeliu, P.L. Andresen and M.L. Pollick, Repassivation and crack propagation of alloy 600 in 288°C water, Corrosion 53 (1997) 114-120.

[34] G.T. Burstein and R. J. Cinderey, The potential of freshly generated metal surfaces determined from the guillotined electrode: a new technique, Corros. Sci. 32 (1991) 1195-1211.

[35] A.W. Batchelor, L. N. Lam and M. Chandrasekaran, Materials degradation and its control by surface engineering, Imperial college press, London, 2002.

[36] A.V. Levy, Solid Particle Erosion and Erosion-corrosion of materials, ASM international, Materials Park, Ohio, 1995.

[37] H. Wahl, Standardization in the field of wear, Wear 1 (1957) 222-224.

[38] I. Finnie, The mechanism of erosion of ductile metals, Proc. 3rd Nat. Cong. Appl. Mech., ASME (1958) 527-532.

[39] A.V. Levy, The erosion of metal alloys and their scales, Proc. NACE Conf. Corrosion-Erosion-Wear of materials in emerging fossil material systems, Berkeley (1982) 298-376.

[40] A.V. Levy, The solid particle erosion behavior of steel as a function of microstructure, Wear 68 (1981) 269-287.

[41] S. Endo and M. Nagae, Comparison of experimentally measured and theoretically predicted erosion rates of steels in slurries of low, ISIJ Int. 36 (1996) 87-94.

[42] N.W. Gulden, Influence of brittle to ductile transition on solid particle erosion behavior, Proc. 5th Int. Conf. Eros. Sol. & Liq. Impact, Cambridge (1979) no. 31.

[43] G. Sargent, The erosion of plain carbon steels by ash particles from a coal gasifier, Proc. Int. Conf. Wear Mat., San Francisco, ASME (1981).

[44] T. Quadir and P. Shewmon, Solid particle erosion mechanisms in copper and two copper alloys, Metall. Trans. A 12 (1981) 1163-1176.

[45] W. Tabakoff, A. Hamed and J. Ramachandrin, Study of metals erosion in high temperature coal gas streams, J. Eng. Power 102 (1980) 148-152.

[46] A.V. Levy and P. Chik, The effects of erodent composition and shape on the erosion of steel, wear 89 (1983) 151-162.

[47] U. Lotz, Velocity effects in flow induced corrosion, Proc. Symp. Flow Induced Corros., NACE, Houston (1991) 1-8.

[48] H.J. Wiesmann, Two phase flow patterns, Handbook of fluids in motion, Ann Arbor Sci. Pub., Michigan (1983) 409-424.

[49] G.W. Govier and K. Aziz, The flow of complex mixtures in pipes, Van Nostrand Co., New York (1972) 324-326.

[50] W. Blatt, T. Kohley, U. Lotz and E. Heitz, The influence of hydrodynamics on erosion-corrosion in two phase liquid particle flow, Corrosion 45 (1989) 793-803.

[51] U. Lotz and J. Postlethwaite, Erosion-corrosion in disturbed two phase liquid/particle flow, Corros. Sci. 30 (1990) 95-106.

[52] G. Bianchi, G. Fiori, P. Longhi and F. Mazza, ”Horse shoe” corrosion of copper alloys in flowing sea water: mechanism, and possibility of cathodic protection of condenser tubes in power stations, Corrosion 34 (1978) 396-406.

[53] G.A. Schmitt, W. Bucken and R. Fanebust, Modeling micro turbulences at surface imperfections as related to flow induced localized corrosion, Corrosion 48 (1992) 431-440.

[54] I.M. Hutchings, A model for the erosion of metals by spherical particles at normal incidence, Wear 70 (1981) 269-281.

[55] Y.P. Purandare, A. P. Ehiasarian, M. M. Stack and P.Eh. Hovsepian, CrN/NbN coatings deposited by HIPIMS: a preliminary study of erosion–corrosion performance, Surf. Coat. Technol. 204 (2010) 1158-1161.

[56] M.M. Stack, Y. Purandare and P. Hovsepian, Impact angle effects on the erosion-corrosion of superlattice CrN/NbN PVD coatings, Surf. Coat. Technol. 188-189 (2010) 556-565.

[57] Y.P. Purandare, A. P. Ehiasarian and P. Eh. Hovsepian, Deposition of nanoscale multilayer CrN/NbN physical vapor deposition coatings by high power impulse magnetron sputtering, J. Vac. Sci. Technol. 26 (2008) 288-296.

[58] T. Foley and A. Levy, The erosion of heat-treated steels, Wear 91 (1983) 45-64.

[59] R.C.D. Richardson, The wear of metals by relatively soft abrasives, Wear 11 (1968) 245-275.

[60] D. Tabor, Mohs's hardness scale: a physical interpretation, Proc. Phys. Soc. B 67 (1954) 249.

[61] A.A. Torrance, An explanation of the hardness differential needed for abrasion, Wear 68 (1981) 263-266.

[62] M.M. Stack, J.S. James and Q. Lu, Erosion–corrosion of chromium steel in a rotating cylinder electrode system: some comments on particle size effects, Wear 256 (2004) 557-564.

[63] I. Finnie, Some observations on the erosion of ductile metals, Wear 19 (1972) 81-90.

[64] Erosion of surfaces by solid particles, Pages 87-103, Wear 3 (1960) 87-103.

[65] A.V. Levy, Mostafa Aghazadeh and G. Hickey, The effect of test variables on the platelet mechanism of erosion, Wear 108 (1986) 23-41.

[66] A.V. Levy and P. Yau, Erosion of steels in liquid slurries, Wear 98 (1984) 163-182.

[67] G.T. Burstein and K. Sasaki, Effect of impact angle on the slurry erosion-corrosion of 304L stainless steel, Wear 240 (2000) 80-94.

[68] B.D. Jana and M. M. Stack , Modelling impact angle effects on erosion-corrosion of pure metals: construction of materials performance maps, Wear 259 (2005) 243-255.

[69] M.M. Stack, N. Corlett and S. Zhou, Impact angle effects on the transition boundaries of the aqueous erosion–corrosion map, Wear 225-229 (1999) 190-198.

[70] D. López, J.P. Congote, J.R. Cano, A. Toro and A.P. Tschiptschin, Effect of particle velocity and impact angle on the corrosion erosion of AISI 304 and AISI 420 stainless steels, Wear 259 (2005) 118-124.

[71] B.C. Syrett, Erosion-corrosion of copper-nickel alloys in sea water and other aqueous environments - a literature review, Corrosion 32 (1976) 242-252.

[72] J. Postlethwaite,Y. Wang, G. Adamopoulos and S. Nesic, Relationship between modelled turbulence parameters and corrosion product film stability in disturbed single-phase aqueous flow, in: modeling aqueous corrosion, NATO ASI Series, Kluwer Academic Publ. Dordrecht, The Netherlands (1994).

[73] E. Heitz, Chemo-mechanical effects of flow on corrosion, Corrosion 47 (1991) 135-145.

[74] J.P. Gudas, G. J. Danek and R. B. Niederberger, Accelerated corrosion of copper-nickel alloys in polluted waters, Corros. 76, Int. corros. forum devoted exclusively to the prot. and perform of mater., Houston (1976).

[75] J. Postlethwaite, B. J. Brady, M. W. Hawrylak, E. B. Tinker, Effects of corrosion on the wear patterns in horizontal slurry pipelines, Corrosion 34 (1978) 245-250.

[76] S. Nesic, Erosion-corrosion in disturbed flow, Ph. D. Thesis, University of Saskatchewan, Saskatoon (1991)

[77] M. Matsumura, Y. Oka, H. Hiura and M. Yano, The role of passivating film in preventing slurry erosion-corrosion of austenitic stainless steel, ISIJ Int. 31 (1991) 168-176.

[78] R.J.K. Wood, S. P. Hutton, The synergistic effect of erosion and corrosion: trends in published results, Wear 140 (1990) 387-394.

[79] F. Aiming, L. Jinming, T. Ziyun, An investigation of the corrosive wear of stainless steels in aqueous slurries, Wear 193 (1996) 73-77.

[80] S. Das, D.P. Mondal, R. Dasgupta and B. K. Prasad, Mechanisms of material removal during erosion-corrosion of an Al–SiC particle composite, Wear 236 (1999) 295-302.

[81] H.X. Guo, B.T. Lu and J.L. Luo, Interaction of mechanical and electrochemical factors in erosion–corrosion of carbon steel, Electrochimica Acta 51 (2005) 315–323.

[82] Y. Li, G.T. Burstein and I. M. Hutchings, The influence of corrosion on the erosion of aluminium by aqueous silica slurries, Wear 186 (1995) 515-522.

[83] R. Malka, S. Nesic and D.A. Gulino, Erosion-corrosion and synergistic effects in disturbed liquid particle flow, Wear 262 (2007) 791-799.

[84] Y. Zheng, Z. Yao, X. Wei and W. Ke, The synergistic effect between erosion and corrosion in acidic slurry medium, Wear 186 (1995) 555-561.

[85] S. Zhou, M.M. Stack and R.C. Newman, Electrochemical studies of anodic dissolution of mild steel in a carbonate-bicarbonate buffer under erosion-corrosion conditions, Corros. Sci. 38 (1996) 1071-1084.

[86] B.W. Madsen, Measurement of erosion-corrosion synergism with a slurry wear test apparatus, Wear 123 (1988) 127-142.

[87] D. Li, X. Mao and R. Zhu, Kinetics of passive film formation on scratched bare surfaces of stainless steels in magnesium chloride solutions, Corrosion 49 (1993) 877-884.

[88] M.D. Bermudez, F. J. Carrion, G. M. Nicolas and R. Lopez, Erosion-corrosion of stainless steels, titanium, tantalum and zirconium, Wear 258 (2005) 693-700.

[89] A. Neville and X. Hu, Mechanical and electrochemical interactions during liquid solid impingement on high-alloy stainless steelsWear 251 (2001) 1284-1294.

[90] A. Neville, M. Reyes, T. Hodgkiess and A. Gledhill, Mechanisms of wear on a Co-base alloy in liquid solid slurries, Wear 238 (2000) 138-150.

[91] K. Sasaki and G.T. Burstein, The generation of surface roughness during slurry erosion-corrosion and its effect on the pitting potential, Corros. Sci. 38 (1996) 2111-2120.

[92] G.T. Burstein and K. Sasaki, The birth of corrosion pits as stimulated by slurry erosion, Corros. Sci. 42 (2000) 841-860

[93] G.T. Burstein and K. Sasaki, Detecting electrochemical transients generated by erosion–corrosion, Electrochim. Acta 46 (2001) 3675-3683

[94] H.D. Kim, Designing processing and properties of advanced engineering materials, Mat. Sci. Forum: 449-454 (2004) 781.

[95] Wear and erosion; metal corrosion, Annual book of ASTM standards 03.02, ASTM.

[96] A. Neville and T. Hodgkiess, Characterisation of high-grade alloy behaviour in severe erosion–corrosion conditions, Wear 233-235 (1999) 596-607.

[97] G.T. Burstein and K. Sasaki, Effect of impact angle on the slurry erosion-corrosion of 304L stainless steel, Wear 240 (2000) 80-94.

[98] R. Malka, S. Nesic and D.A. Gulino, Erosion-corrosion and synergistic effects in disturbed liquid-particle flow, Wear 262 (2007) 791-799.

[99] I.M. Hutchings, The erosion of materials by liquid flow, Cambridge, MTI Pub. no. 25 (1986).

[100] H. Hertz,.Über die Berührung fester elastischer Körper, J. Reine Angew. Mat. 92 (1882) 156-171.

[101] R.D. Mindlin, Compliance of elastic bodies in contact. Trans. ASME: Journal of Applied Mechanics 16 259-269.

[102] R.D. Mindlin and H. Deresiewicz, Elastic spheres in contact under varying oblique forces, Trans. ASME: Journal of Applied Mechanics 20 (1953) 327-344.

[103] E. McEwen, Stresses in elastic cylinders in contact along a generatrix, Philosophical Magazine 40 (1949) 454.

[104] J.O. Smith and G.K. Liu, Stresses due to tangential and normal loads on an elastic solid, Trans. ASME: Journal of Applied Mechanics 21 (1953) 371-378.

[105] S.C. Hunter, Energy absorbed by elastic waves during impact, Journal of Mechanics and Physics of Solids 5 (1957) 162-171.

[106] J. Reed, Energy losses due to elastic wave propagation during an elastic impact, J. Phys. D: Appl. Phys. 18 (1985) 2329-2337.

[107] L.N. Rogers and J. Reed, The adhesion of particles undergoing an elastic plastic impact with a surface, J. Phys. D: Appl. Phys. 17 (1984) 677-689.

[108] H. Deresiewicz, A note on Hertz impact, Acta Mechanica 6 (1968) 110-112.

[109] A.E.H. Love, A Treatise on the Mathematical Theory of Elasticity Dover, New York (1944).

[110] K.L. Johnson, Contact Mechanics, Cambridge University Press (1985).

[111] J.E. Sears, On the longitudinal impact of metal rods with rounded ends, Proc. of the Camb. Phil. Soc. 14 (1908) 257.

[112] J.M. Lifshitz and H. Kolsky, Some experiments on anelastic rebound, J. Mech. and Phys. Solids 12 (1964) 35-43.

[113] J.P. Andrews, Theory of collision of spheres of soft metals, Phil. Magazine 9 (1930) 593-610.

[114] N. Maw, J. R. Baeber and J. N. Fawcett, The oblique impact of elastic spheres, Wear 38 (1976) 639-646.

[115] C. Thornton and C. Randall, Applications of theoretical contact mechanics to solid particle system simulation, Micromechanics of Granular Materials, Elsevier, Amsterdam (1988) 133-142.

[116] C. Thornton and K.K. Yin, Impact of elastic spheres with and without adhesion. Powder Technology, Vol. 65 (1991) 153-166.

[117] R.M. Davies, The determination of static and dynamic yield stresses using a steel ball, Proceedings of the Royal Society of London A 197 (1949) 416-432.

[118] S. Wall, W. John and S.L. Georen, Application of impact adhesion theory to particle kinetic energy loss measurements, Particles on Surfaces, Plenum Publishing Corporation (1989) 19-34.

[119] G.P. Tilly, Erosion caused by airborne particles, Wear 14 (1969), 63-79.

[120] I. Langmuir, US Army Airforce Tech., Report 5418 (1946).

[121] I. Finnie, Erosion of surfaces by solid particles, Wear 3 (1960) 87-103.

2 Single particle impingement current transients for prediction of erosion enhanced corrosion on 304 stainless steel

2.1 Introduction

As described earlier, erosion-corrosion, the simultaneous action that is a consequence of mechanical forces on the surface due to particle impacts and electrochemical corrosion, is a major problem in most fossil fuel related and mineral processing industries. The damage to materials caused by the synergism of erosion and corrosion is sometimes twice the sum of the damage caused by erosion and corrosion separately. It is well known that the erosion rate of metals depends on impact angle and impact velocity of the particles impacting on the surface [1, 2, 3, 4], and the effects of these parameters on erosion-corrosion rate of materials have been quantified [5, 6, 7, 10]. Burstein *et al.* reported that the current transients detected from single impacts at oblique angles are larger than those observed at normal angles of impact [4, 8]. It is known that both erosion and corrosion enhance one another. In a recent study performed by us using an *in situ* nanoindentation device, it was shown that increasing the applied anodic current reduces hardness on the surface of a metal [9]. We also have studied the repassivation behaviour of passive materials during erosion-corrosion. We found that repassivation current transients usually develop in two steps; one very fast initial step of passive film nucleation on the surface and then the consequent growth of the film [11]. Sundararajan reported that when a single spherical particle impacts a flat metal surface, in air and at a normal impact angle, the produced scar volume correlates well with kinetic energy of the particles impacting on the surface of materials [12].

F. Mohammadi, J. Luo, B. Lu and A. Afacan, Corros. Sci. 52 (2010) 2331-2340.

The primary objective of the work presented in this chapter was to correlate the mechanical characteristics of a single particle impact on a passive metal surface with the consequent electrochemical response of the surface to this impact in an aqueous medium. A second objective, based on the above correlation and the flowing slurry characteristics, was to determine whether the correlation could be used to predict the erosion-enhanced corrosion rate of the passive metal in different slurry flow conditions.

2.2 Experimental methods

An apparatus was designed to impinge single particles on the surface of the samples while they are kept at desired passive potentials. This device is capable of impinging particles of various sizes up to 3 mm in diameter at different angles and different velocities. Experiments can be run in corrosive environments since the whole device is made of stainless steel. Figure 2.1 shows a schematic diagram of the single impingement system. Single particles are inserted into the fluid stream using two pistons. These pistons are designed so they can be removed completely from their cylinder. One of the pistons blocks the fluid stream while the particle is inserted from the other. Then a change in the position of the pistons introduces the particle along the wall into the stream towards the nozzle.

As it was difficult to determine values for the low current peaks when particle velocities were below 5 m/s, a velocity range between 5 m/s and 11 m/s was chosen to

F. Mohammadi, J. Luo, B. Lu and A. Afacan, Corros. Sci. 52 (2010) 2331-2340.

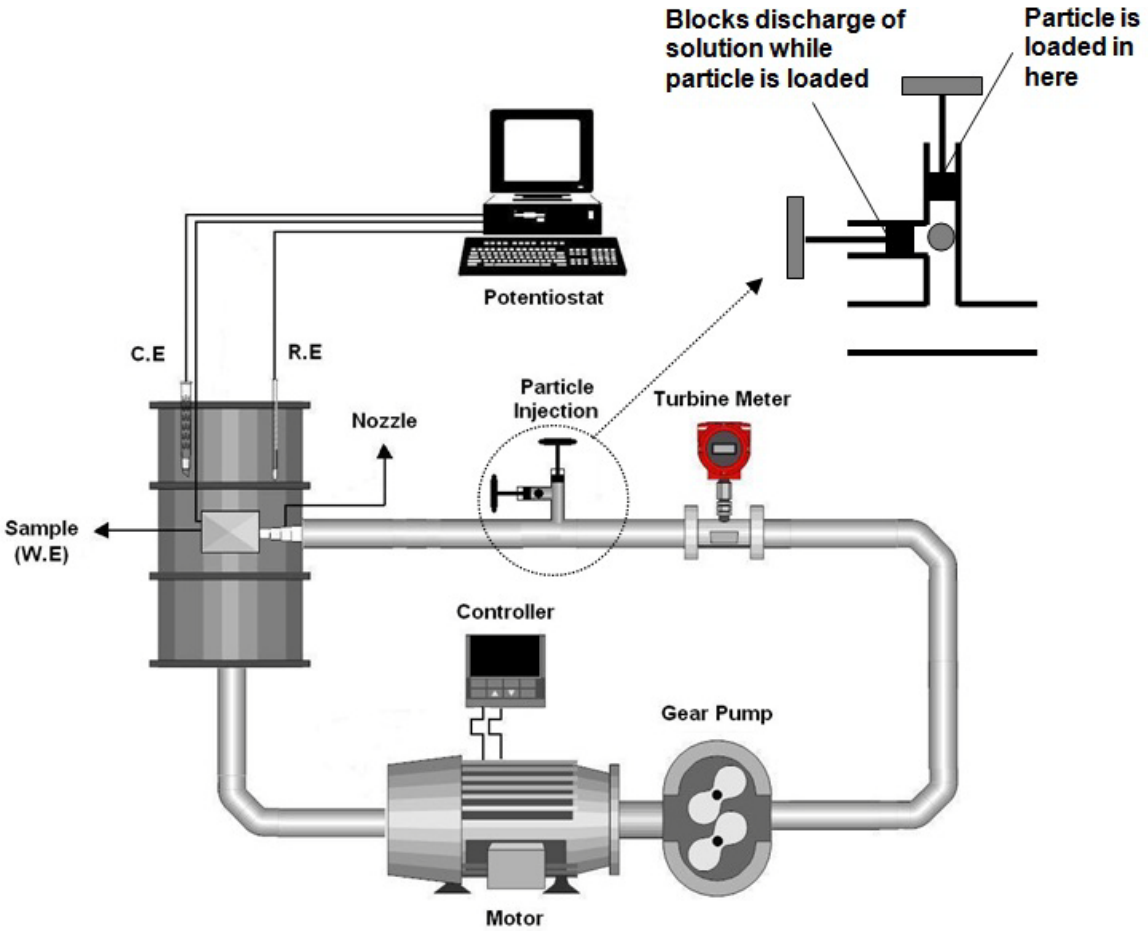

Figure 2-1 Schematic representation of single impingement system.

conduct experiments. A cone-shaped nozzle was used to accelerate single particles. To confirm that the particles reached the desired velocities at the nozzle tip, a conical nozzle 0.2 m in length was required based on the equations of motion of a particle introduced in a fluid stream (Equation 2.1) [13, 14].

$$\frac{\pi d^3 \rho_P}{3}\frac{dV_P}{dt} = \frac{C_d \rho_a \pi d^2}{4}\left(V_P - V_F\right)^2 \qquad (2.1)$$

Where V_P is particle velocity, ρ_P is particle density, d is particle diameter, C_d is drag coefficient and V_F is fluid velocity.

F. Mohammadi, J. Luo, B. Lu and A. Afacan, Corros. Sci. 52 (2010) 2331-2340.

A Motion Scope PCI 8000S high speed camera also was coupled to the system to measure the impact and rebound angles and velocities of particles before and after impacting on the surface of the samples. The high speed camera velocity measurements of the particles also confirmed that the theoretical calculations for nozzle design were sufficiently accurate. Table 2.1 represents the calculated and measured particle velocities in comparison with fluid velocities at the nozzle tip.

Table 2-1 **Comparison of theoretical particle velocities and velocity measured at nozzle tip using high speed camera for 2.18 mm zirconia particles.**

V_{Fluid} (m/s)	5.5	7.5	8.9	10.2
$V_{Particle\ Theory}$ (m/s)	5.2	7.1	8.5	9.7
$V_{Particle\ Camera}$ (m/s)	5.3	7.2	8.7	10

A REF 600 Gamry Potentiostat was connected to the system for keeping the samples at desired passive potentials and recording the current transients generated by single particle impacts. A high data acquisition rate (1000 Hz) was required to collect enough data points and record the current transients accurately. Samples were passivated at 200 mV w.r.t. SCE for 600 seconds so that a stable passive film formed on the surface. A saturated calomel electrode was used as the reference electrode and a platinum mesh 4 x 6 cm was chosen as the counter electrode in all experiments.

A 5 mm diameter grinding disk rotating at 2250 rpm and a small sample having an accurately known area of 2.2 mm^2 were prepared. The disk is capable of grinding the small sample surface at frequencies up to 500 Hz depending on the rpm of the disk. This setup was connected to the potentiostat, samples are kept at 200 mV w.r.t. SCE and

F. Mohammadi, J. Luo, B. Lu and A. Afacan, Corros. Sci. 52 (2010) 2331-2340.

water flowed on the surface at desired flow rates. Samples were continuously depassivated by contacting the grinding disk on the surface. When the grinding disk was removed from the surface the surface started to repassivate under the same conditions under which it repassivated after single particle impacts except that, in this case, the depassivated area was known precisely.

A slurry jet system also was used, which provided conditions close to that of service conditions. This enabled us to compare the results of single impacts with real condition erosion-corrosion in the tailings of an oil sands extraction process. A positive displacement pump was used to pump slurries with different sand concentrations onto the surface of the samples at different velocities and different angles while the samples were held at desired passive potentials and the generated current was recorded. Silica sand from Lane Mountain Company was mixed with tap water to prepare slurries. Tap water was used because its composition was very close to the water that is used in oil sands extraction. Table 2.2 shows the tap water composition and properties.

Table 2-2 Tap water composition and characteristics used in these experiments reported by EPCOR.

Aluminum (mg/L)	0.051	Iron (mg/L)	< 0.002
Dissolved Chloride (mg/L)	4.19	Lead (mg/L)	< 0.0005
Dissolved Fluoride (mg/L)	0.76	Manganese (mg/L)	< 0.001
Chromium (mg/L)	< 0.001	Conductivity (µS/cm)	375
Copper (mg/L)	0.003	pH	7.7

The mean diameter of the sand particles used to make slurries was 40 µm. One of the concerns about using tap water as electrolyte is the conductivity and the corresponding IR drop problems. However, in these experiments the reference electrode was always positioned at a fixed distance of 0.5 cm from the working electrode. Also, based on the

F. Mohammadi, J. Luo, B. Lu and A. Afacan, Corros. Sci. 52 (2010) 2331-2340.

conductivity of the solution (Table 2.2), the maximum current of 4 μA (Figure 2.2) and the sample area of 0.54 cm^2, the maximum contribution of IR drop in the applied potential was calculated to be below 10 mV:

$$\text{IR drop} = I\frac{l}{\sigma A} \le 4\times10^{-6}(\text{A})\times\frac{0.5\,\text{cm}}{375\times10^{-6}\,(\text{S/cm})\times0.54\,\text{cm}^2} \le 10\,\text{mV}$$

This means that a maximum error of 10 mV in the 200 mV applied potential can be caused by IR drop, a value which is less than 5% and so is negligible.

Three kinds of spherical particles with two different sizes were chosen to conduct single impingement experiments. Table 2.3 presents the properties of the particles used in these experiments. The particles were selected in a manner that the ratio of their hardness to the hardness of the samples was greater than 1.5 so that the results were independent of the hardness of the impacting particles as for the data reported by Sundararajan [15, 9].

Table 2-3 Particles characteristics reported by Ortech Advanced Ceramics Co.

Particle	Size (mm)	Density (g/cm^3)	E (GPa)	Poisson Ratio	Vickers Hardness
ZrO_2	2.00 & 2.18	6.05	210	0.3	1200
Si_3N_4	2.00 & 2.18	3.25	310	0.26	1650
Glass	2.00	2.52	74	0.23	620

Glass particles were used to study only the effect of impact angle on repassivation charge, since these particles were less perfectly spherical than the other particles. Table 2.4 shows several diameter measurements performed on different spots of randomly selected particles. As apparent from the data in Table 2.4, glass particles were not suitable for comparing charge consumption during repassivation since they produced

F. Mohammadi, J. Luo, B. Lu and A. Afacan, Corros. Sci. 52 (2010) 2331-2340.

higher current transients due to the combination of their hardness or impact energy and their angularity, which was not an independent variable in this study.

The 304 stainless steel plates were purchased from AK Steel Corporation (C: 0.08%, Mn: 2%, P: 0.045%, S: 0.03%, Si: 0.75%, Cr: 18%, Ni: 8%, N: 0.1%), from which 3x18 mm samples were cut for use in the experiments. Before each experiment sample surfaces were ground with P1200 sandpaper. After grinding, samples were washed with distilled water and air-dried.

Table 2-4 Diameter measurements made at different spots of particles to compare their sphericity.

Manufacturer Reported Diameter (mm)	Measured Diameter (mm)	#1	#2	#3	#4	#5
Glass (2mm)	**Average**	**1.88**	**1.96**	**2.14**	**2.03**	**1.90**
	Minimum	1.76	1.83	1.88	1.91	1.75
	Maximum	1.93	2.08	2.22	2.06	2.02
Si_3N_4 (2.18mm)	**Average**	**2.18**	**2.18**	**2.18**	**2.18**	**2.18**
	Minimum	2.18	2.18	2.18	2.18	2.18
	Maximum	2.18	2.18	2.18	2.18	2.18
ZrO_2 (2.18mm)	**Average**	**2.18**	**2.18**	**2.18**	**2.18**	**2.18**
	Minimum	2.18	2.18	2.18	2.18	2.18
	Maximum	2.18	2.18	2.18	2.18	2.18

2.3 Results and discussion

2.3.1 Determination of the charge required for repassivation of unit area of the surface

Several methods have been used to study the amount of charge consumed during repassivation of depassivated materials and the mechanism and characteristics of the repassivation process under different conditions, including use of a guillotined electrode, scratched electrode and abraded electrode [16-21]. In order to determine the charge consumed during repassivation per unit area of the samples in this study, single

F. Mohammadi, J. Luo, B. Lu and A. Afacan, Corros. Sci. 52 (2010) 2331-2340.

particle impact experimental conditions were applied for a small sample to confirm that the repassivation process happens under the same conditions as used for the single impact tests. The rotating grinding disk was positioned at the surface of the small sample so that the surface was ground 500 times per second while the potentiostat was connected to the system while the sample was kept at 200 mV w.r.t SCE and the current was being recorded. After the grinding disk was removed from the surface, the sample immediately started to repassivate. The charge under the potentiostatic curve obtained for repassivation of the small sample surface accurately quantified the amount of charge required in the repassivation process per unit area of the surface since the small sample surface area was precisely known. The consumed charge during repassivation for the small sample with 2.2 mm^2 surface area was 76 μC when samples are at 0.2V w.r.t. SCE. Table 2.5 compares calculated theoretical values with experimental data obtained using the small sample grinding method, and shows the that theoretical approach is fairly accurate in determining the depassivated surface based on the consumed charge and assumptions made.

Table 2-5 **Comparison between theory and small sample grinding method showing a very close to reality prediction of depassivated area by theory for ZrO_2 particles considering a 50% Fe_2O_3 and 50% Cr_2O_3 composition for the passive film.**

Particle's Kinetic Energy (J)	Theoretically Calculated Depassivated Area (m^2)	Area Obtained by Comparison to Reference Sample (m^2)
6×10^{-5}	1.03×10^{-9}	0.88×10^{-9}
1.2×10^{-4}	2.83×10^{-9}	2.42×10^{-9}
2.0×10^{-4}	4.37×10^{-9}	3.74×10^{-9}
3.3×10^{-4}	8.74×10^{-9}	7.48×10^{-9}

F. Mohammadi, J. Luo, B. Lu and A. Afacan, Corros. Sci. 52 (2010) 2331-2340.

2.3.2 Transient dissolution during particle impingement

A series of single particle impingement experiments were done using different particles and impact angles. The transient corrosion current response of stainless steel to single particle impingement was strongly affected by the impact angle, and the transient current response reached a maximum at an angle around 30^{o} (Figure 2.2). Similar results were reported by others [4, 8]. As expected, the most severe erosion enhanced corrosion was observed at an impact angle of 30^{o}. Hence, in the following experiments, the erosion-enhanced corrosion behaviour was investigated using a fixed impact angle of 30^{o}.

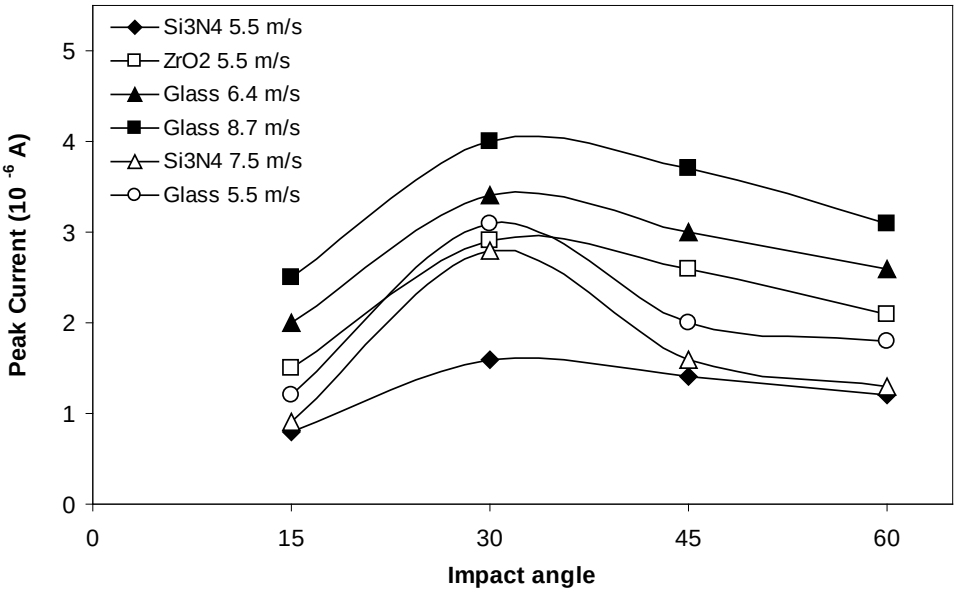

Figure 2-2 Effect of impact angle on current transients due to single particle impacts at 200mV w.r.t SCE.

The particle impingement process was recorded with a high speed camera and sequential photo frames captured by the high speed camera were combined (Figure 2.3). These photos were captured from a side view showing the particle approaching the

F. Mohammadi, J. Luo, B. Lu and A. Afacan, Corros. Sci. 52 (2010) 2331-2340.

sample surface at 45° impact angle, impacting on the surface and rebounding at a different angle.

When the particles hit the surface as shown in Figure 2.3, the passive film is either broken or removed from the surface. This causes a current transient during potentiostatic experiments (Figure 2.4). An optical micrograph of the scar produced by this impact and a SEM image of the impacting zirconia particles also are shown. The promoted anodic dissolution and repassivation over the surface of craters created by the impingement of solid particles dominated the corrosion of passivated targets in flowing slurries [11]. The local current density over the crater surface rose sharply immediately after breakdown of passive film caused by particle impingement, followed by a gradual current decay due to surface repassivation.

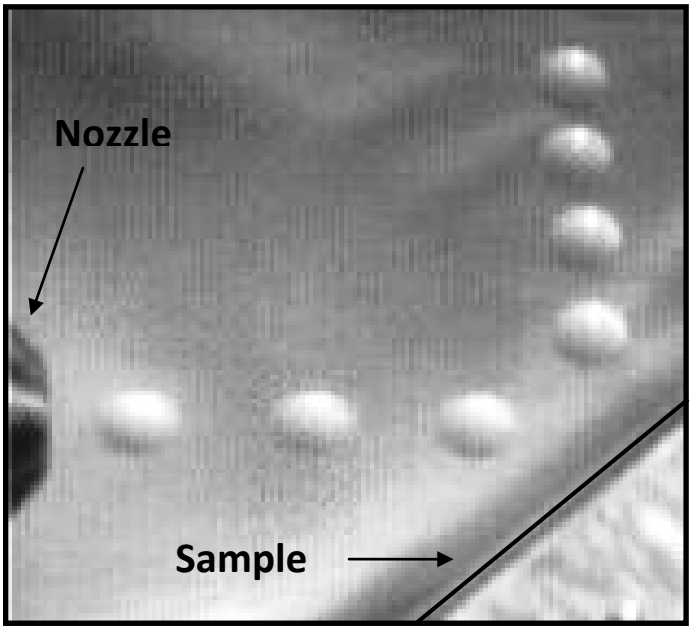

Figure 2-3 Overlap of seven high speed photo frames at 2000 fps showing impact and rebound of zirconia particles on the surface of 304 stainless steel.

F. Mohammadi, J. Luo, B. Lu and A. Afacan, Corros. Sci. 52 (2010) 2331-2340.

The repassivation curves occurred in two stages, as described previously; the first stage has a very fast current decay period assigned to the formation of the very first atomic layers of passive film and the second has a slower current decay period ascribed to formation of consequent layers of passive film. The characteristics and behaviour of current transients were described previously [11].

Erosion enhanced corrosion of passive targets is dominated by the frequency of particle impingement and the extra electrical charge consumed by the repassivation and anodic dissolution over the damaged surface. The former is a function of the dynamics of slurry flow and the latter can be evaluated by the area under the curve of transient current vs. time.

2.3.3 Charge calculation and bare metal surface generation mechanism

Hutchings [22] reported that the lips formed during single impacts of hardened spherical steel particles on mild steel are detached from the surface only at velocities equal to or higher than 180 m/s. The impingement velocity of slurries in this study was about one order of magnitude less than the critical impact velocity reported to cause material removal from a surface by a single particle impact. The formed lip is very small and is not detectable and the scar shape is almost completely circular (Figure 2.4), although the particles were impinged at the surface at 45° angle of impact. This was a consequence of the very low impact velocities used in this study and indicated that the amount of plastic deformation taking place on the surface was very far from the limits of material detachment from the surface. Hence, in the present study, we assumed that

F. Mohammadi, J. Luo, B. Lu and A. Afacan, Corros. Sci. 52 (2010) 2331-2340.

the particle was completely rigid, i.e., deformation of the particle during the impingement was negligible. To further simplify the analysis, only plastic deformation of the target caused by the normal component of impact force was considered, and so the crater shape was assumed to be a cap of the impacting spherical particle. The latter assumption was reasonable as the crater shape from all impacts was close to circular, indicating that the role of tangential force in forming the crater shape was negligible. It should be noted that the role of the tangential velocity in giving rise to the corrosion

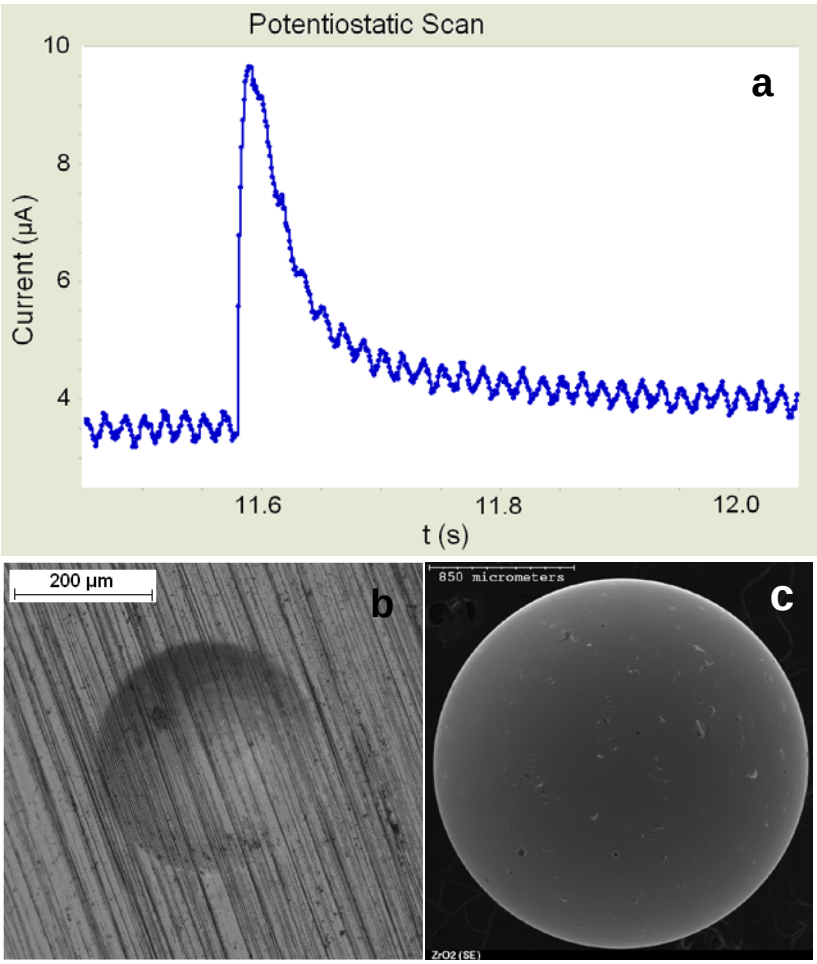

Figure 2-4(a) Sample current transient caused by single zirconia particle impact on 304 stainless steel at 8.5 m/s at 200mV w.r.t. SCE. (b) Optical image of the scar created by single zirconia particle impact on 304 stainless steel surface. (c) SEM image of a spherical zirconia particle.

F. Mohammadi, J. Luo, B. Lu and A. Afacan, Corros. Sci. 52 (2010) 2331-2340.

current transient can never be ignored. The erosion of the material at lower velocities was likely to be caused by accumulation of the plastic deformation on the surface due to multiple impacts and continuous strain, ultimately leading to final material detachment [23].

According to the discussion in the previous section, the only source of the transient current was the transient dissolution and repassivation over the damaged area of the crater surface where the passive film was removed and the bare metal surface was produced while the target surface was impacted by the particle. The size of the electrical charge of repassivation was a function of the combination of the material, corrosive medium and test conditions. During transient dissolution, part of the metallic atoms was dissolved into the solution and the rest formed insoluble compounds that became the constituents of passive films. Since the potential of 0.2 V w.r.t. SCE was in the passive region for 304 stainless steel, it was assumed, to simplify our analysis, that the electric charges consumed in the reformation of the passive film over the damaged surface was much more than those consumed in the anodic dissolution, i.e., the electrical charge calculated from the current transit was substantially the same as that consumed in the formation of the passive film. Thus, the electric charge produced in the transient current was approximately equal to the product of the damaged surface area and the electric charge required to fully repassivate the unit area of bare metal surface, as the current arising from active dissolution of metal into solution can be ignored.

After a crater is formed by a particle impact, the target surface will deform plastically and the surface area will increase (Figure 2.5). Because the passive film has

F. Mohammadi, J. Luo, B. Lu and A. Afacan, Corros. Sci. 52 (2010) 2331-2340.

much lower plastic deformation capacity when compared to the substrate, it will rupture and the bare metal surface will be equal to the increment of surface area after the formation of the crater. The surface area increment can be calculated from geometry when the size of the solid spherical particle and the diameter of the crater are known.

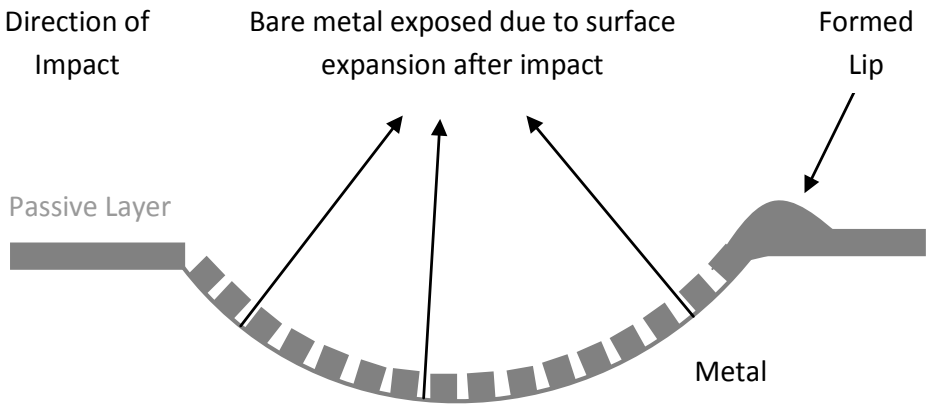

Figure 2-5 **Schematic representation of the process of bare metal exposure due to surface expansion caused by a single impact.**

When the surface area increment is known, the electric charge required for repassivation can be estimated. The Faraday equation, Equation 2.2, is used to determine the electric charge consumed in the repassivation of bare metal surface with unit area.

$$Q_{\mathrm{R}} = \frac{m_{\mathrm{RF}}\, F\, Z_{\mathrm{FF}}}{M_{\mathrm{F}}} \qquad (2.2)$$

Where Q_R is the consumed charge during repassivation, F is the Faraday constant, Z_{FF} is the number of charges, M_F is the molecular weight of the passive film, and m_{RF} is the

F. Mohammadi, J. Luo, B. Lu and A. Afacan, Corros. Sci. 52 (2010) 2331-2340.

mass of the passive film that is removed due to impact, the product of volume and passive film density, $m = \rho V$, resulting in Equation 2.3.

$$Q_{\mathrm{R}} = \frac{\rho_{\mathrm{F}} V_{\mathrm{RF}} F Z_{\mathrm{FF}}}{M_{\mathrm{F}}} \qquad (2.3)$$

The volume of passive film can be calculated from the thickness of the passive film and its area. The surface area expansion increment after impact is used to calculate volume. The thickness of the passive film was measured using an ellipsometry technique after passivating the samples at 200 mV w.r.t. SCE for 10 min with a VASE (variable angle spectroscopic ellipsometer). This device was capable of high accuracy measurement of various properties of thin films, including thickness. The change in the polarization of the incident light beam was measured accurately after reflection from samples surface and further translated to thickness of the passive film, found to be 2 nm.

Since the exact values of *Z* and *M* are not known for the passive film on 304 stainless steel, the goal was to maximize *Q* using some approximations, and to find if that value was comparable with experimentally measured values for consumed charge of repassivation. If the results were comparable, then the current transients were produced only by the bare metal surface that was produced due to surface expansion after impact. Thus it was assumed that the passive film was very compact and no pores were present in its structure. These assumptions enabled maximization of ρ and thus also *Q*. Knowing that the passive film was composed mostly of iron and chromium oxides and hydroxides [24, 25, 26], the charges that were consumed for the formation of each of the above compounds varied from $Z = 2$ for $Fe(OH)_2$ to $Z = 8$ for Fe_3O_4. The

F. Mohammadi, J. Luo, B. Lu and A. Afacan, Corros. Sci. 52 (2010) 2331-2340.

density of the passive film was between 3400 kg/m^3 and 5170 kg/m^3, the densities of $Fe(OH)_2$ and Fe_3O_4, respectively [27]. The maximum value of *Q* was obtained when it was assumed that the passive film was composed of nonporous Fe_3O_4. Table 2.6 shows these calculated charges due to surface expansion along with experimentally measured charges arising from impact of particles of 2.18 mm diameter at different velocities.

Table 2-6 **Comparison of experimentally measured consumed charge for repassivation and repassivation charge consumed due to surface expansion calculation.**

Particle (2 mm)	Velocity (m/s)	Experimentally Measured Consumed Charge (C)	Charge Calculation due to Surface Expansion (C)
Si3N4	5.5	2.94 E-8	8.95 E-10
Si3N4	7.8	1.02 E-7	3.46 E-9
ZrO_2	6.9	1.2 E-7	4.6 E-9
ZrO_2	7.8	2.1 E-7	8.5 E-9

The predicted values were two orders of magnitude lower than experimental values, even after maximizing *Q* with all the approximations. This suggested that it was unlikely that the depassivated surface area was only a result of surface expansion during particle impact. Although the velocities were very low, lip formation was very small and removal of material was not observed macroscopically in either these experiments or previous erosion experiments; some portions of the passive film were detached from the surface either by attaching to the particles or breaking off into the solution. Although these parts could not be detected visually, since they were very small, the effect of their removal was observed in the magnitude of current transients.

Another method of determining the actual depassivated area inside a crater is to compare the repassivation charge under a current transient with the unit area

F. Mohammadi, J. Luo, B. Lu and A. Afacan, Corros. Sci. 52 (2010) 2331-2340.

repassivation charge obtained using the small sample grinding method described earlier. This comparison provides an estimate of the actual depassivated area that then can be compared with results obtained using other methods (Table 2.6).

2.3.4 Correlation between volume of the scar and particle kinetic energy

The total deformation that happens on the surface due to a single particle impact is the sum of the elastic and plastic deformations. The elastic portion of the deformation, in which its energy will be returned to the particle at the end of the impact period and results in a particle rebound velocity in the normal direction, Z_{el}, arising from elastic approach of the centre of the mass of particle toward the plane surface, is calculated using the Hertzian elastic theory [28]:

$$Z_{el} = 24.35\,\sigma_y{}^2\,R\,E_r{}^{-2} \qquad (2.4)$$

where, E_r is the reduced modulus of elasticity, σ_y is the yield stress of the surface material and R is the radius of the particle.

On the other hand, the extent of plastic deformation and its depth can be calculated using simple geometrical calculations, by considering that the volume of scar, V_{scar} , to be equal to the volume of a spherical cap produced by a single impact, V_{cap}. Using Figure 2.6, V_{cap} formed on the surface is calculated as follows:

$$V_{cap} = \frac{1}{3}\pi h^2 (3R - h) \qquad (2.5)$$

$$R^2 = (R-h)^2 + a^2$$

F. Mohammadi, J. Luo, B. Lu and A. Afacan, Corros. Sci. 52 (2010) 2331-2340.

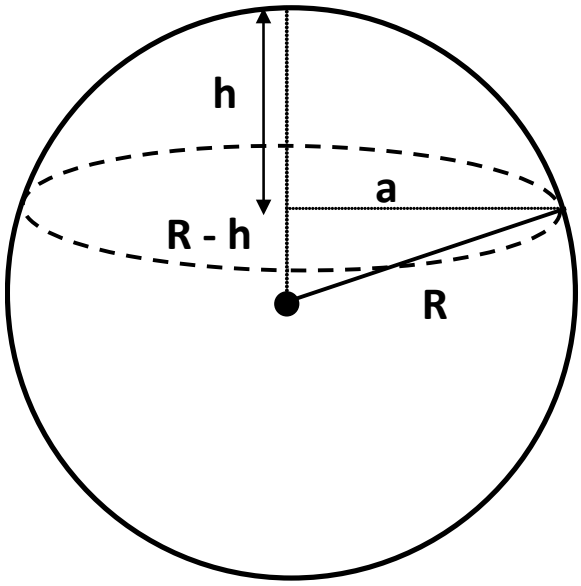

Figure 2-6 Schematic representation of the spherical cap formed due to single particle impact on the surface of the sample.

where *a* is the radius of the crater produced on the surface. The depth of elastic deformation is almost ten times smaller than plastic deformation [29, 30], and so it was ignored in this study. The deformation of target material due to elastic deformation from particle impact at subordnance velocities is negligible compared to that of plastic deformation [30].

The diameters of solid particles may affect the crater sizes. To demonstrate this effect, the volume of the scar was plotted versus particle kinetic energy (Figure 2.7) for the velocity range used in this study, and a good linear correlation was observed between the scar volume and particle kinetic energy. This suggested that the size of the particles did not affect the consumed charge for repassivation, provided that the kinetic energy of the impacting particles was the same.

F. Mohammadi, J. Luo, B. Lu and A. Afacan, Corros. Sci. 52 (2010) 2331-2340.

2.3.5 Dynamic hardness concept and linear correlation of kinetic energy of the particle with crater volume

Dynamic hardness, P_d, is the maximum dynamic flow pressure during impact of a particle on a flat surface. It can be calculated using Equation 2.6, as done by Sundararajan *et al.* [12].

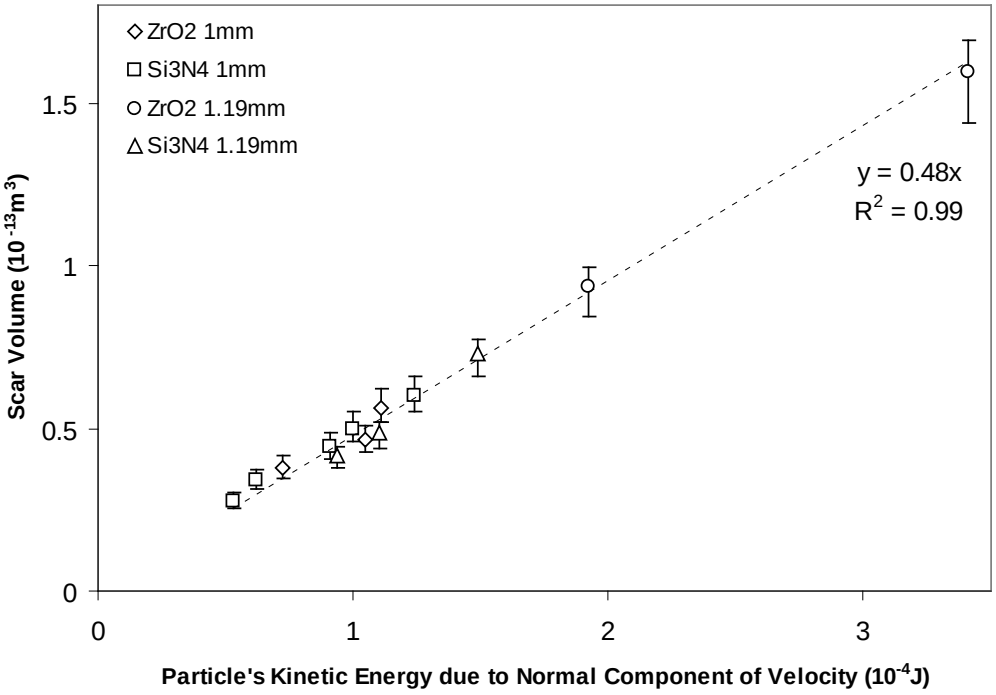

Figure 2-7 Scar volume vs. particle's kinetic energy due to normal component of velocity for silicon nitride and zirconia particles with two different diameters.

$$P_d = \frac{1}{2} m_p \left(V_{ni}^{\ 2} - V_{nr}^{\ 2} \right) / V_{cap} \qquad (2.6)$$

m_p is the mass of particle, V_{ni} is the normal component of impact velocity and V_{nr} is the normal component of rebound velocity. Note that only the normal component of velocity is used to calculate the dynamic hardness of the target material. To determine

F. Mohammadi, J. Luo, B. Lu and A. Afacan, Corros. Sci. 52 (2010) 2331-2340.

the dynamic flow pressure of the target, the dissipated incident energy, U_{pl}, due to plastic deformation is set equal to the sum of deflections of all points in the contact area in *z* direction times the flow pressure:

$$\int_{Z}\int_{S} P_{d}\, ds\, dz = U_{Pl} \qquad (2.7)$$

This integral equals the volume of the crater times the dynamic flow pressure, P_d.

Table 2.7 shows the results for dynamic flow pressure calculated at different velocities, where the ratio of dynamic hardness to the Meyer hardness of 304 stainless steel was also included. It was concluded from these results that dynamic hardness was not very different from static hardness in the case of 304 stainless steel over the velocity range used in these experiments. Under the prevailing experimental conditions, Equations 2.6 and 2.7 show that, from a theoretical point of view, the ratio of kinetic energy of the particle to the volume of the cap is *P*d which is almost constant at these velocities. This means that the volume of the cap varied linearly with the kinetic energy of the particle.

Table 2-7 Dynamic hardness and its ratio to Meyer hardness of the surface at different velocities.

Velocity (m/s)	Particle	Scar Volume(m3)	P_d	P_d/P_s
5.0	ZrO_2	$5.4X10^{-14}$	1851	1.028
7.8	Si_3N_4	$4.3X10^{-14}$	1842	1.023
9.0	ZrO_2	$1.3X10^{-13}$	1850	1.028

F. Mohammadi, J. Luo, B. Lu and A. Afacan, Corros. Sci. 52 (2010) 2331-2340.

2.3.6 Correlation of particle kinetic energy and electrical charge produced by current transient

According to Faraday's law, the electrical charge consumed in repassivation is given by Equation 2.2, which is modified to form Equation 2.3 by replacing mass with the product of density and volume. Thus, according to Equation 2.3, consumed charge for repassivation must obey a linear correlation with volume of the removed passive film as:

$$Q_{\mathrm{R}} = K_1 V_{\mathrm{RF}} \qquad (2.8)$$

where:

$$K_1 = \frac{\rho_{\mathrm{F}} F Z_{\mathrm{FF}}}{M_{\mathrm{F}}} \qquad (2.9)$$

However, experimental measurements in the velocity range of this study (Figure 2.8) indicated a linear correlation between consumed repassivation charge and scar volume, which meant that:

$$Q_{\mathrm{R}} = K_2 V_{\mathrm{Scar}} \qquad (2.10)$$

where V_{Scar} is the scar volume. Combining Equations 2.8 and 2.10 led to a linear correlation between depassivated volume, or volume of the film that was removed, and scar volume:

$$V_{\mathrm{RF}} = \alpha_{\mathrm{V30}} V_{\mathrm{scar}} \qquad (2.11)$$

where:

$$\alpha_{\mathrm{V30}} = K_2 / K_1 \qquad (2.12)$$

F. Mohammadi, J. Luo, B. Lu and A. Afacan, Corros. Sci. 52 (2010) 2331-2340.

α_{V30} is the volumetric α at 30° and its meaning is the ratio of the depassivated volume to the total volume of the scar at 30° impact angle.

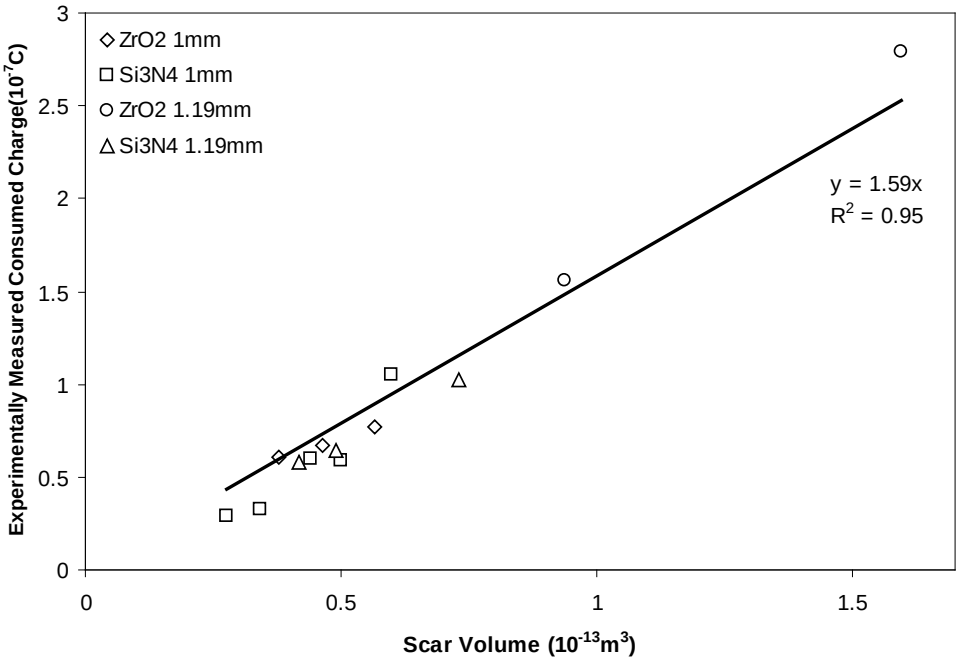

Figure 2-8 Experimentally measured consumed charge vs. Scar volume.

Knowing that the thickness of the passive film was only a few nanometers, almost all of the particle kinetic energy on the surface was consumed to deform the base metal, 304 stainless steel. Thus the portion of the energy that was consumed for deformation of the passive film, only a few atomic layers, was negligible compared to that of the base metal. Knowing this and using the concept of dynamic hardness:

$$K_{\mathrm{n}} = 0.5\, m_{\mathrm{p}}\, V_{\mathrm{n\ Particle}}^{\ 2} = P_{\mathrm{d}}\, V_{\mathrm{Scar}} \qquad (2.13)$$

In Equation 2.13, K_{n} is particle kinetic energy due to the normal component of its velocity and $V_{\mathrm{n\ Particle}}$ is the normal component of particle velocity. Combining Equations

F. Mohammadi, J. Luo, B. Lu and A. Afacan, Corros. Sci. 52 (2010) 2331-2340.

2.3, 2.11 and 2.13 results in the following correlation between consumed charge for repassivation and particle kinetic energy:

$$Q_{\mathrm{R}} = \frac{\rho_{\mathrm{F}}\, \alpha_{\mathrm{V30}}\, K_{\mathrm{n}}\, F\, Z_{\mathrm{FF}}}{P_{\mathrm{d}}\, M_{\mathrm{F}}} \qquad (2.14)$$

From the data in Table 2.7 it was known that, within the impingement velocity range of this study, dynamic flow pressure could be treated as a constant. Thus, according to Equation 2.14, it was expected that there would be a linear correlation between consumed charge and particle kinetic energy in the normal direction. This expectation was confirmed by the experimental data in Figure 2.9.

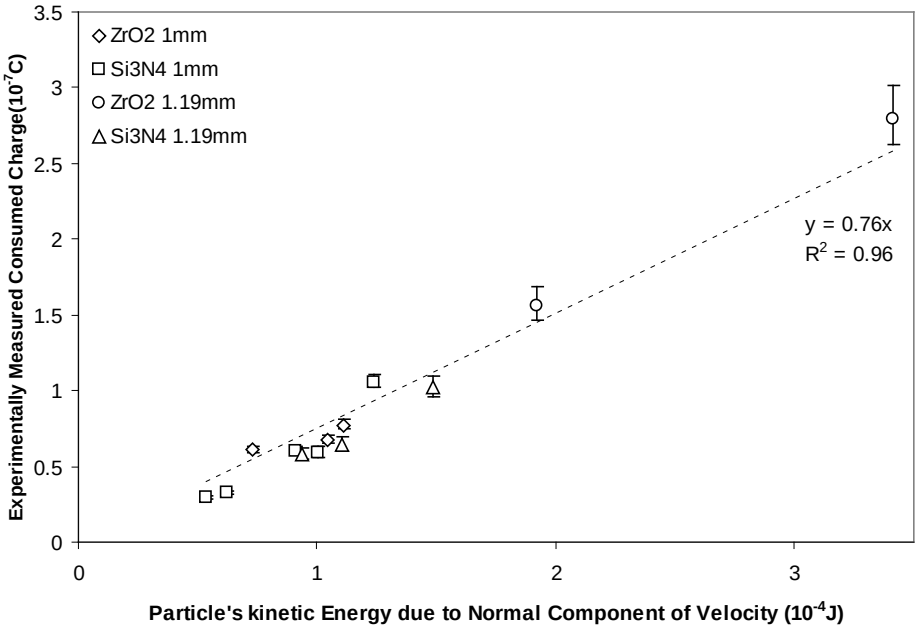

Figure 2-9 Experimentally measured consumed charge vs. particle's kinetic energy in normal direction.

The results in Figure 2.9 also indicate that the difference in particle hardness did not affect the transient current response as long as the particles had the same kinetic

F. Mohammadi, J. Luo, B. Lu and A. Afacan, Corros. Sci. 52 (2010) 2331-2340.

energies. It should be noted that particles were chosen so that the ratio of particle to sample hardness was greater than 1.5 in all experiments.

Equation 2.12 shows that α depends on two parameters, K_1 and K_2. The former can be determined theoretically and the latter experimentally. It was difficult to calculate the exact value of K_1 since it depended on passive film density and the number of transferred charges in the repassivation process, each of which were not known exactly. However, it was obvious that K_1 had a constant value for any specific condition. On the other hand, K_2 was determined from the slope of the plot of the experimental curve for consumed charge of repassivation versus scar volume (Figure 2.8). Thus, α is the ratio of an experimental constant to a theoretical constant for each angle of particle impact. The value of α was not a constant for all angles, although it was shown to be a constant for a particular angle within the velocity range of this study. Consequently, these values were designated as α_{V30}.

An approximate value of α was obtained by assuming that the passive film was composed equally of Cr_2O_3 and Fe_2O_3, (5210 kg/m^3 and 5240 kg/m^3 respectively[27]), which gave a value of 8 x 10^{-5} for α. The physical meaning of this value was that the depassivated volume of the film was less than 0.01% of the total scar volume that was created by a single impact at 30°. Note that the above estimated value of α was the ratio of the depassivated volume of the film to the volume of the scar, not the ratio of the surfaces. For calculation of the ratio of the depassivated surface to the scar surface the volumes in Equation 2.11 were replaced by the corresponding surfaces as follows.

F. Mohammadi, J. Luo, B. Lu and A. Afacan, Corros. Sci. 52 (2010) 2331-2340.

Assuming that passive film thickness was uniform over the surface of the sample and that passive film was totally removed in the areas where depassivation happened:

$$S_{\mathrm{RF}} = V_{\mathrm{RF}} \,/\, 2\times10^{-9}\left(\text{thickness of the film}\right) \qquad (2.15)$$

The corresponding surface area of the created scar in a spherical cap as shown in Figure 2.6 was calculated using simple geometry:

$$V_{\mathrm{cap}} = S_{\mathrm{cap}}\left(h\left(3R-h\right)/6R\right) \qquad (2.16)$$

Since in these experiments the depth of the scar was very small(μm) in comparison to the radius of the particle(mm), *h* was very small compared to 3*R*, and so *(*3*R*-*h)* was approximately equal to 3*R*, so that:

$$V_{\mathrm{cap}} = S_{\mathrm{cap}}\left(\frac{h}{2}\right) \qquad (2.17)$$

h in all impacts varied between 3 to 11 μm. Now, replacing Equations 2.15 and 2.17 in Equation 2.11 for an impact with 8 μm scar depth resulted in the following equation:

$$S_{\mathrm{RF}} \times 2\times10^{-9} = \alpha_{\mathrm{V30}} \times S_{\mathrm{cap}} \times 8\times10^{-6} \qquad (2.18)$$

A new coefficient, α_{S30}, is defined to correlate S_{RF} and S_{cap}. α_{S30} is the planar α at 30° and its meaning is the ratio of the depassivated area to the total area of the scar at 30° impact angle. Rewriting Equation 2.18 leads to the approximate value of 0.3 for α_{S30}, as shown in Equation 2.19:

$$S_{\mathrm{RF}} = 0.3\, S_{\mathrm{cap}} \qquad (2.19)$$

This means that almost 30% of the scar surface was depassivated due to a single impact at 30°. Different values of α were expected to be observed with changing impact angle. One of the key factors that affected the value of α was the ratio of normal and

F. Mohammadi, J. Luo, B. Lu and A. Afacan, Corros. Sci. 52 (2010) 2331-2340.

tangential forces on the surface, which was a constant for each angle. This effect could be investigated by comparing impacts at different impact angles.

2.3.7 Prediction of current on 304 stainless steel in flowing slurry

It was observed in the previous section that the experimentally measured consumed charge during repassivation varied linearly with particle kinetic energy at low velocities. When the kinetic energy of the sand particles in a slurry was calculated, the charge consumed during repassivation by each of their impacts could be read from the curve in Figure 2.9, and so it was possible to predict the total current on a sample in flowing slurry. When the sand concentration and flowing velocity of slurry were low, the interaction between the impingements of different particles could be ignored and the linear superposition model was valid, i.e., the total electrical charge resulting from multiple impingements was equal to the sum of electric charge created by individual impacts. The average kinetic energy of individual particles was calculated using the mean diameter of silica sand particles in the slurry, 40 μm, and different velocities of slurry. From the calculated values for the kinetic energy of each particle, Figure 2.9 was used to find the corresponding consumed charge during repassivation (extrapolation of the curve to other energies). A simple calculation using the particle concentration in the slurry gave an estimate for the current, *i*, that was produced while the slurry was flowing on the sample. The method is described in detail below;

$$i = \frac{Q_t}{t} \qquad (2.20)$$

F. Mohammadi, J. Luo, B. Lu and A. Afacan, Corros. Sci. 52 (2010) 2331-2340.

where *t* is time duration that the target is subjected to the impacts of *n* particles and in these calculations it has the value of unity. Total charge Q_t per unit of time is:

$$Q_t = \sum_{1}^{n} Q_i \qquad (2.21)$$

where *n* is the total number of the particles impacting on the surface in unit of time and Q_i is the charge that is produced by each of those impacts. Total number of particles impacting on the surface in unit of time, *n*, is;

$$n = \frac{V_{slurry}\ A_{nozzle}\ \rho_{slurry}\ C_{sand}}{m_{particle}} \qquad (2.22)$$

where *V* is the slurry velocity, *A* is nozzle tip area, ρ is density of slurry, *C* is sand concentration in slurry and *m* is the average mass of particles. Using the above approach, the estimated current for slurries containing different sand concentrations at two velocities of 10 m/s and 15 m/s was calculated (Figure 2.10) along with the results from slurry jet experiments. The above calculations and comparison were viable at the low velocities used in this study and in low sand concentrations where it was possible to assume that particles acted seperately on the surface and they did not have an interaction with each another on or near the surface. As observed from Figure 2.10, at very low sand concentrations up to 1 wt%, the calculated data obtained through the described approach was very close to the experimental values obtained using slurries.

As the sand concentration increased, the calculated current prediction had a higher value than the experimental current under real conditions at both 10 m/s and 15 m/s velocities. One major possible reason for this deviation was that particle interactions became more significant at higher sand concentrations.

F. Mohammadi, J. Luo, B. Lu and A. Afacan, Corros. Sci. 52 (2010) 2331-2340.

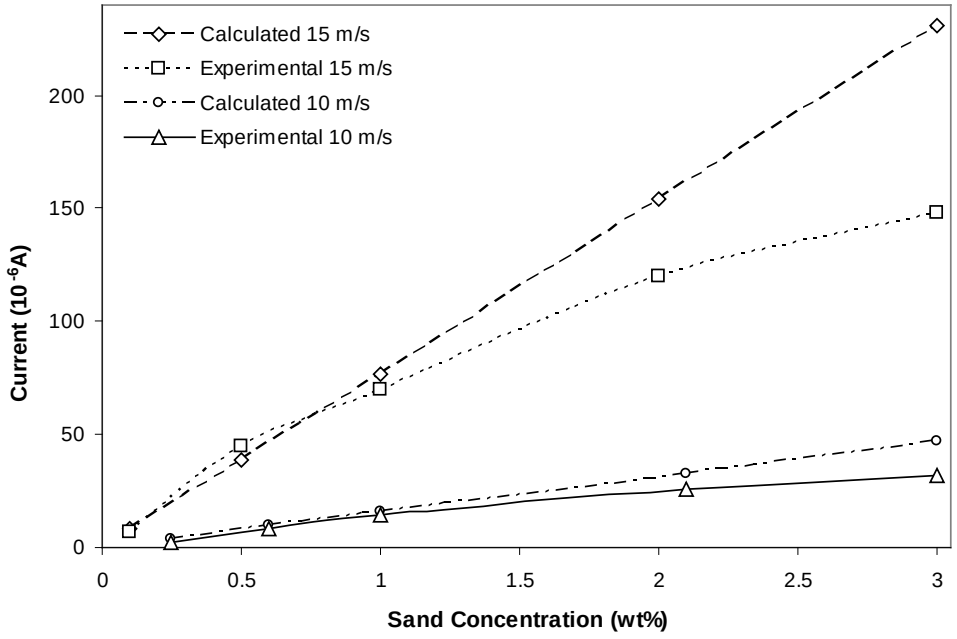

Figure 2-10 Comparison between predicted current using single impingement consumed charge vs. kinetic energy curve and experimentally measured current on 304 stainless steel in flowing slurry.

2.4 Conclusions

(1) Both theoretical analysis and experimental measurements showed that the volume of the crater created by individual particle impingement, in the impingement velocity range between 5 m/s and 11 m/s, correlated linearly with particle kinetic energy.

(2) Even at low velocities where it was not expected that material would be removed from the surface in a single particle impingement process, the passive film on some parts of the crater surface was removed by a single impact. It was found that the freshly bared metal surface area fraction of the crater was about 30% when the impingement angle was fixed at 30^{o}.

F. Mohammadi, J. Luo, B. Lu and A. Afacan, Corros. Sci. 52 (2010) 2331-2340.

(3) The electric charge required to repassivate the damaged surface area created by the particle impingement was a linear function of the crater volume or the particle kinetic energy, in the impact velocity range between 5 m/s and 11 m/s.

(4) The electrical charge required to repassivate the unit bare metal surface determined from the single particle impingement could be used to predict the average corrosion current density of target material in flowing slurry at low slurry sand concentrations up to 1 wt%. When the sand concentration or impact velocity was low, the linear superposition model gave a good prediction.

2.5 References

[1] I. Finnie, The mechanism of erosion of ductile metals, Proc. of 3rd U.S. Natl. Congr. of Appl. Mech. ASME, NewYork (1958) 527–532.

[2] A.V. Reddy and G. Sundararajan, Erosion behaviour of ductile materials with a spherical non-friable erodent, Wear 111 (1986) 313–323.

[3] I. Finnie, G.R. Stevick and J.R. Ridgely, The influence of impingement angle on the erosion of ductile metals by angular abrasive particles, Wear 152 (1992) 91–98.

[4] G.T. Burstein and K. Sasaki, Effect of impact angle on the slurry erosion–corrosion of 304L stainless steel, Wear 240 (2000) 80-94.

[5] J.B. Zu, I.M. Hutchings and G.T. Burstein, Design of a slurry erosion test rig, Wear 140 (1990) 331–344.

[6] M. Matsumura, Y. Oka, H. Hiura and M. Yano, The role of passivating film in preventing slurry erosion-corrosion of austenitic stainless steel, ISIJ Int. 31 (1991) 168–176.

[7] Y.Li, G.T. Burstein and I.M. Hutchings, The influence of corrosion on the erosion of aluminium by aqueous silica slurries, Wear 186–187 (1995) 515–522.

[8] A.J. Smith, M. Stratmann and A. W. Hassel, Investigation of the effect of impingement angle on tribocorrosion using single impacts, Electrochimica Acta 51 (2006) 6521-6526.

[9] K. Wang, B.T. Lu and J.L. Luo, Surface Hardness degradation of iron in corrosion media with different pHs, NACE International, Northern Area Western Conference, Edmonton, (2008).

[10] A.V. Levy and G. Hickey, Liquid-solid particle slurry erosion of steels, Wear 117 (1987) 129 – 146.

[11] B.T. Lu, J.L. Luo and F. mohammadi, K. Wang and X.M. Wan, Correlation between repassivation kinetics and corrosion rate over a passive surface in flowing slurry, Electrochimica Acta 53 (2008) 7022-7031.

[12] Y. Tirupataiah and G. Sundararajan, The volume of the crater formed by the impact of a ball against flat target materials— the effect of ball hardness and density, Int. J. Imapct Engng. 9 (1990) 237-246.

[13] I. Finnie, Erosion of surfaces by solid particles, Wear 3 (1960) 87-103.

[14] G.P. Tilly, Erosion caused by airborne particles, Wear 14 (1969) 63-79.

[15] A.A. Torrance, An explanation of the hardness differential needed for abrasion, Wear 68 (1981) 263-266.

[16] G.T. Burstein and P.I. Marshall, Growth of passivating films on scratched 304L stainless steel in alkaline solution, Corrosion Science 23 (1983) 125-137.

[17] G.T. Burstein and R.J. Cinderey, The potential of freshly generated metal surfaces determined from the guillotined electrode-a new technique, Corrosion Science 11 (1991) 1195-1211.

[18] J.-D. Kim and S.-I. Pyun, The effects of applied potential and chloride ion on the repassivation kinetics of pure iron, Corrosion Science 38 (1996) 1093-1102.

[19] S. Ahila, A.B. Reynders and H.J. Grabke, The evaluation of the repassivation tendency of Cr-Mn and Cr-Ni steels using scratch technique, Corrosion Science 38 (1996) 1991-2005.

[20] J.H. Nordlien, S. Ono, N. Masuko and, K. Nisancioglu, A TEM investigation of naturally formed oxide films on pure magnesium, Corrosion Science 39 (1997) 1397-1414.

[21] G.T. Burstein and R.M. Organ, Repassivation and pitting of freshly generated aluminium surfaces in acidic nitrate solution, Corrosion Science 47 (2005) 2932–2955.

[22] I.M. Hutchings, Particle erosion of ductile metals: A mechanism of material removal, Wear 27 (1974)121-128.

[23] J.G.A. Bitter, A study of erosion phenomena part I, Wear 6 (1963) 5-21.

[24] C.M. Abreu, Characterization of the electrochemical behaviour of cerium implanted stainless steels, Electrochimica Acta 47 (2002) 2215-2222.

[25] C.-O.A. Olsson, Passive films on stainless steels—chemistry, structure and growth, Electrochimica Acta 48 (2003) 1093-1104.

[26] N.E. hakiki, The electronic structure of passive films formed on stainless steels, Corrosion Science 37 (1995) 1809-1822.

[27] Knovel Critical Tables (2nd Edition), Norwich, N.Y. Knovel, 2005.

[28] P.A. Engel, Impact wear of materials, Elsevier scientific publishing company, Amsterdam-Oxford-NewYork, 1976.

[29] D. Tabor, The hardness of metals, Oxford Univ. Press, London, 1951.

[30] G. Sundararajan and P. G. Shewmon, The use of dynamic impact experiments in the determination of the strain sensitivity of metals and alloys, Acta Metallurgica 31 (1983) 101-109.

3 Effects of particle angular velocity and friction force on erosion enhanced corrosion of 304 stainless steel

3.1 Introduction

It was previously mentioned that erosion-corrosion occurs when solid particles suspended in the slurry impact the surface of the material. The synergistic interaction between the electrochemical reactions and mechanical forces applied by solid particles cause damage much more than the sum of individual damages caused by each of these phenomena [1]. Also several factors, which significantly affect the wear due to erosion-corrosion, were discussed in previous chapters [2-9]. In the case of passive materials in an aqueous medium, the rate of electrochemical reactions on the surface is very low; however, if solid particles impact the passive layer, depending on their velocity, direction of impact, shape and mechanical properties, the passive film either breaks off or is partly damaged [8-11]. When the passive film is damaged and depassivation occurs, the rate of electrochemical reactions on the surface increases dramatically. One part of this increase in electrochemical reactions is correlated with the repassivation process while another part is correlated with metallic dissolution [12, 13]. If the passive material is held in the passive potential range, the rate of repassivation will be much higher than the rate of metallic dissolution. After the impact, the increased current rapidly reduces to its original value before particle impact and a current transient peak is observed in just a fraction of a second before repassivation is completed. The magnitude of this peak which represents the erosion enhanced corrosion is dependent on the extent of the depassivation of the surface. Thus, in order to obtain better understanding of the

F. Mohammadi and J. Luo,Corros. Sci. 52 (2010) 2994-3001.

effects of different parameters on the depassivation process and erosion-corrosion rate, it is important to study the problem of a particle impacting a flat surface and the corresponding damage mechanisms.

Due to the very short impact periods and the highly localized deformations included in the impact phenomenon, studying the impact becomes a very complicated problem. The linear and angular velocities of the particle and its direction of motion after impact depend on many factors. Linear and angular velocities of the particle before impact, its impact angle on the surface, the hardness and the roughness of the surfaces in contact and the friction force between the particle and the surface are some of the relevant factors. It has been shown by Kharaz *et al.* that when a particle impacts a flat surface in air, most of the particle velocity in the normal direction is lost at impact angles higher than 50^{o}. Under the same impact conditions, the particle velocity in the tangential direction is mostly lost at impact angles around 60^{o} [14-17]. Also the particle angular velocity due to the impulse that is transferred to it during the impact is a maximum at 50^{o} [14-17]. Effects of the angular velocity and travelling direction of the particle before impacting the surface on its rebound direction and the angular velocity after impact have been previously studied [18, 19]. On the other hand, it has been found that the maximum erosion-corrosion damage occurs at lower impact angles around 30^{o} [20-22]. Also single impingement experiments have shown that the erosion enhanced corrosion becomes a maximum at 30^{o} impact angle [11]. In this chapter, effects of different impact parameters on the erosion enhanced corrosion of 304 stainless steel

F. Mohammadi and J. Luo,Corros. Sci. 52 (2010) 2994-3001.

and the depassivation of the surface were investigated by impingement of particles on the surface in an aqueous medium.

3.2 Experimental methods

304 stainless steel sheets (UNS S30400) were cut down to 3x18 mm samples. The original plate was purchased from AK Steel Corporation (Table 3.1). Before performing experiments each sample was finished with a *P1200* grit sand paper, washed with distilled water and air-dried.

Table 3-1 Composition of the 304 stainless steel (wt%).

C	Mn	P	S	Si	Cr	Ni	N
0.08	2	0.045	0.03	0.75	18	8	0.1

The test device used in this work has been described previously in chapter 2 (Figure 2.1). This device is capable of impinging particles with different diameters up to 3 mm at impact angles ranging from 15^{o} to 90^{o} at velocities between 1.5 m/s and 25 m/s.

Velocities between 3 m/s and 7.5 m/s were chosen to conduct experiments. In this velocity range, current transients were large enough to be detected and differentiated from each other while this velocity range was also close to the service condition in the tailings of the oil sands processing facilities. In order to accelerate the particles, a nozzle with the shape of a cone was used. The velocities of the particles were later confirmed with pictures captured by a Motion Scope PCI 8000S high speed camera that was coupled to the experimental setup. *Image J* software was used to perform the velocity measurements of particles at the nozzle tip, velocity

F. Mohammadi and J. Luo,Corros. Sci. 52 (2010) 2994-3001.

measurements of particles before and after impact, and the measurements of impact and rebound angles. The details of this design along with combined sequential photo frames that were used for velocity measurements are described in chapter 2.

Electrochemical measurements were performed in a three electrode system setup with a REF 600 Gamry potentiostat that was connected to the experimental setup. The potentiostat held the samples at 200 mV (vs. SCE) while it was recording the corresponding currents as a function of time. A saturated calomel electrode (SCE) was used as the reference electrode and a 4 x 6 cm platinum mesh was used as the counter electrode in all experiments.

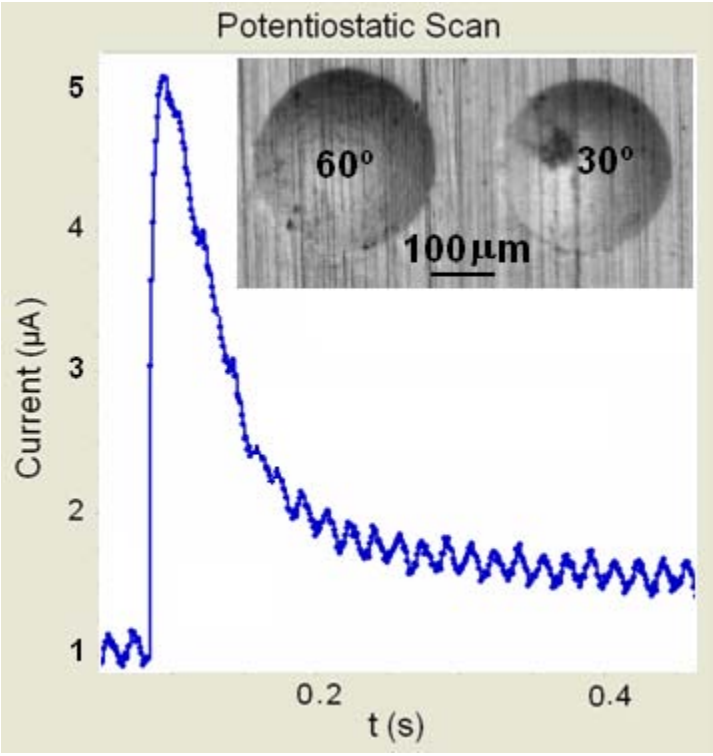

Figure 3-1 Sample current transient due to zirconia particle impact on 304 stainless steel at 7 m/s at 200mV$_{SCE}$ along with micrographs of the scars.

F. Mohammadi and J. Luo,Corros. Sci. 52 (2010) 2994-3001.

A high data acquisition rate was necessary to precisely detect the current transients, since depassivation and repassivation processes are very fast and happen in a fraction of a second. Thus a 1000 Hz data acquisition rate was used in these experiments to collect enough data points. Figure 3.1 shows a sample current transient along with two micrographs of the scars formed due to impacts of particles at different angles.

A stable and uniform passive film was required in order to study the effect of impact dynamics on depassivation. Thus, a potential of 200 mV (vs. SCE), which lies in the mid range of passive potentials for 304 stainless steel according to its dynamic polarization curve, was chosen to conduct these experiments. The passive film was formed and stabilized for 10 minutes, where a current density of 2 $\mu A/cm^2$ was recorded at the end of this period and no significant decrease in this current was recorded.

Because of the similarities between the composition of tap water and the water that is present in the tailings of the oil sands extraction process, tap water with a pH of 7.7 was chosen to conduct these experiments. Table 2.2 gives more details about the composition of the water that was used as electrolyte. One concern with using tap water as the electrolyte was its conductivity. The corresponding IR drop could cause errors during electrochemical measurements. A closer look at the current ranges that were measured in these experiments (μA), the conductivity of the solution (375 μS/cm) and 0.5 cm distance between the positions of the reference and working electrodes, reveals that the maximum IR drop contribution was not significant in these experiments

F. Mohammadi and J. Luo,Corros. Sci. 52 (2010) 2994-3001.

and the corresponding errors were less than 5%. The details of IR drop calculations are given in chapter 2.

Spherical zirconia and silicon nitride particles with 2.18 mm diameter were used to perform these experiments. More details on particle shapes can be found in table 2.3. The main factor in the selection of particles was their hardness so that the ratio of the hardness of the particles to the hardness of the target was always greater than 1.5 for both zirconia and silicon nitride particles. This allowed us to assume that the results were almost independent of particle hardness as was previously reported by other researchers [23].

3.3 Results and discussion

3.3.1 Physical and mechanical aspects of the impact

It has been reported that the energy loss due to the elastic waves produced during impact of a particle on the surface is very small and the coefficient of restitution, e, can be directly calculated by measuring the rebound and impact velocities as follows [24-26]:

$$e = \frac{V_{\text{rebound}}}{V_{\text{impact}}} \tag{3.1}$$

where V_{rebound} is the rebound velocity of the particle and V_{impact} is the impact velocity of the particle. Coefficient of restitution is a useful parameter that shows the amount of energy that is dissipated during the impact. It can also be shown as e_{n} and e_{t}, which are the normal and tangential coefficients of restitution, respectively. In this study, the

F. Mohammadi and J. Luo,Corros. Sci. 52 (2010) 2994-3001.

former was used to define the extent of plastic deformation on the surface and the latter was used to calculate the angular velocity of particles after impact. These quantities can be defined according to Figure 3.2 and through Equations 3.2 and 3.3.

$$e_{\mathrm{n}} = \frac{V_{\mathrm{nr}}}{V_{\mathrm{ni}}} \tag{3.2}$$

$$e_{\mathrm{t}} = \frac{V_{\mathrm{tr}}}{V_{\mathrm{ti}}} \tag{3.3}$$

where V_{ni} and V_{ti} are normal and tangential components of particle impact velocity and V_{nr} and V_{tr} are normal and tangential components of particle rebound velocity.

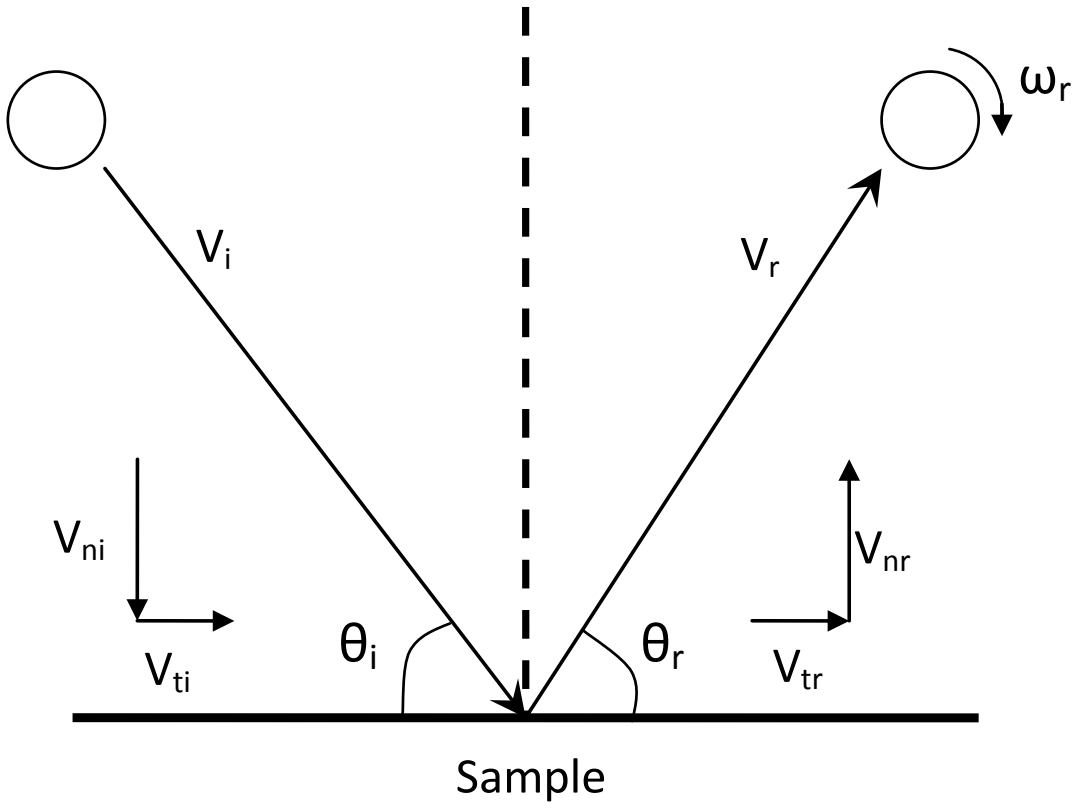

Figure 3-2 Schematic representation of a single particle impacting a flat surface and the corresponding translational and angular velocities.

F. Mohammadi and J. Luo,Corros. Sci. 52 (2010) 2994-3001.

A plot of e_n against particle impact angle for the low velocities used in this study is shown in Figure 3.3. It was found that as the impact angle increased from glancing to normal angles, the normal coefficient of restitution decreased. Increasing the impact angle at constant velocity increases the normal component of the velocity; however, the ratio of the rebound to impact velocity in the normal direction is reduced. This is mainly due to increased plastic deformation on the surface, during which more energy is dissipated.

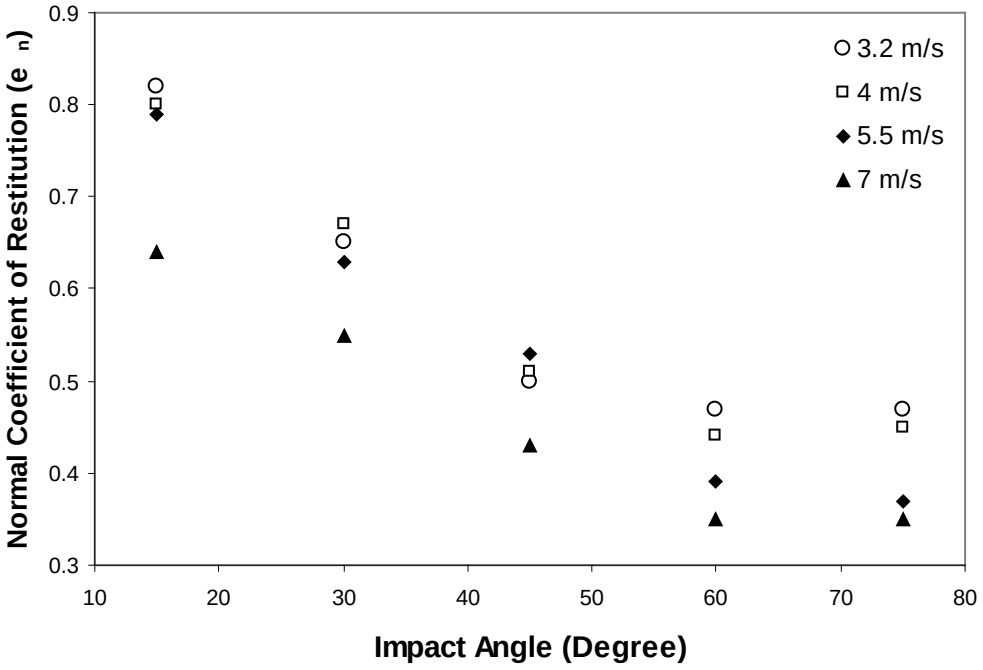

Figure 3-3 Normal coefficients of restitution as a function of impact angle for zirconia particles impacting 304 stainless steel surface at four different velocities under flow of a fluid.

As described earlier, impact and rebound velocities were calculated by analyzing the photos where the change in the position of the centre of mass of the particles with time

F. Mohammadi and J. Luo,Corros. Sci. 52 (2010) 2994-3001.

was measured. Values obtained for e_n from the velocity measurements before and after impact were between 0.3 and 0.9 depending on the impact angle. Also, following each impact a crater was observed and its dimensions were measured using an optical microscope. These results proved the existence of plastic deformation on the surface due to single particle impacts. As explained in chapter 2, the role of the tangential component of the velocity in plastic deformation on the surface is negligible in the velocity range of these experiments, since no lip formation can be observed and the scar shapes for all impact angles are circular in shape. In addition to the existence of plastic deformation, knowledge of the extent of plastic deformation was necessary to be able to define the deformation regimes and applicable theoretical models. Impacts can be divided into two groups: elastoplastic impacts, where a small amount of plastic deformation is involved, and finite plastic deformation impacts, in which larger amounts of plastic deformations are involved. The former group contains a very limited amount of piling up and sinking in during the impact and can be analyzed by classical impact theories [27]. Thus, in Figure 3.4, $e_n(E^*/Y)^{0.5}$, which represents the extent of deformation, was plotted against $(V_{ni}/V_y)/(E^*/Y)^2$, which represents the extent of the applied force on the surface. Y is the material's yield stress, V_y is the yield velocity, the velocity at which the plastic deformation starts, and E^* is the reduced modulus of elasticity as defined in Equation 3.4:

$$\frac{1}{E^*} = \frac{1}{E_{\text{Particle}}} + \frac{1}{E_{\text{Surface}}} \qquad (3.4)$$

F. Mohammadi and J. Luo,Corros. Sci. 52 (2010) 2994-3001.

where $E_{Particle}$ and $E_{Surface}$ are the moduli of elasticity of the particle and the surface, respectively. Also V_y is defined in Equation 3.5 [26, 27]:

$$V_y = 5.052\left(\frac{Y^5}{E^{*4}\rho}\right)^{0.5} \quad (3.5)$$

where ρ is the particle's density. For more clarification, the finite element analysis results that were previously reported by Wu *et al.* [24-26] are also shown in Figure 3.4. It can be concluded from Figure 3.4 that, for all the impacts that were performed in this study, the extent of plastic deformation fell within the elastoplastic domain where the sinking in and piling up were not significant and the problem could be dealt with by classical theoretical models [26]. V_y was calculated to be 2.7 mm/s for the impact conditions of this study. It is noteworthy that this velocity represents onset of plastic deformation; however, the extent of plastic deformation at this velocity is very small.

It was previously shown in chapter 2 that the shape of the craters formed due to single impacts in the velocity range of this study was almost circular and not a significant piling up could not be detected. Given all the above observations, it was possible to deal with the problem of a particle impacting a flat surface from the rigid body theory point of view. The tangential impulse that worked on the solid surface during the impact was responsible for the angular velocity that was transferred to the particle during the impact. Impulse is defined as the change in the particle's momentum (ΔmV) before and after impact [28]. Impulse is used since it is now possible to calculate the coefficient of friction. Also the angular velocity of the particles can be calculated through the impulse.

F. Mohammadi and J. Luo,Corros. Sci. 52 (2010) 2994-3001.

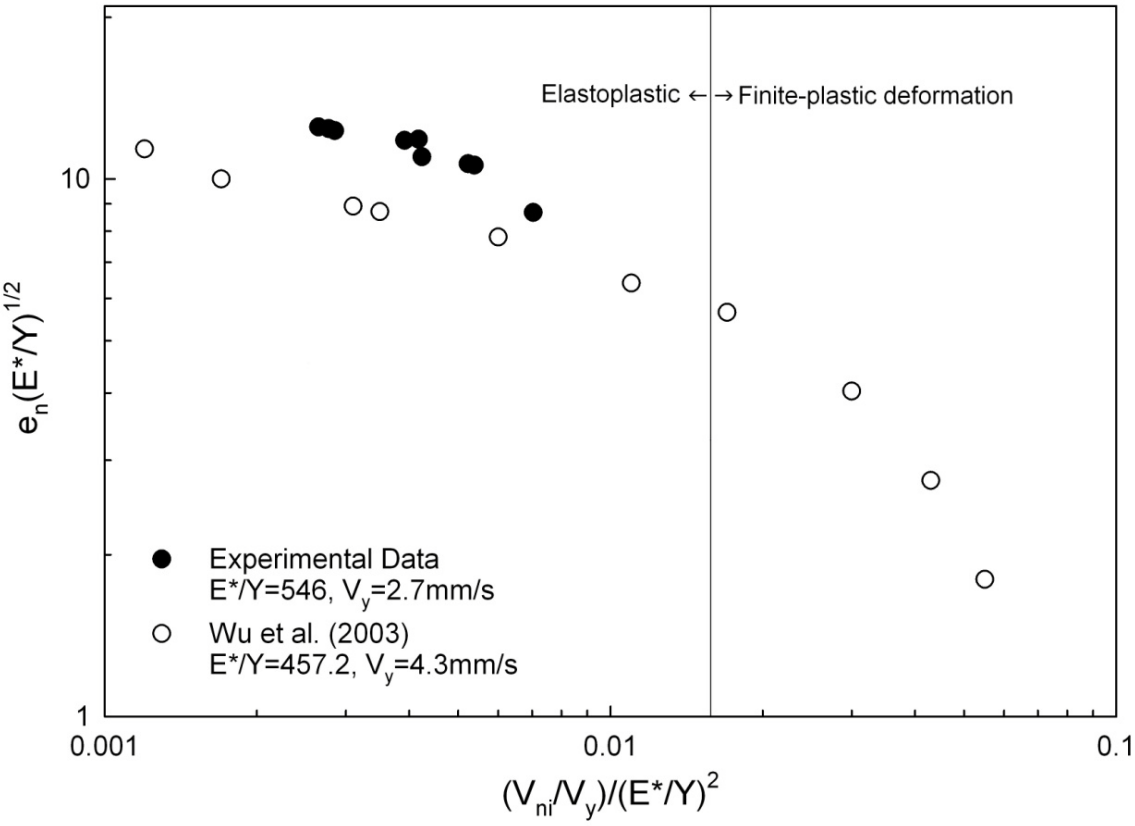

Figure 3-4 Plot of $e_n(E^*/Y)^{0.5}$ against $(V_{ni}/V_y)/(E^*/Y)^2$ for determination of the plastic deformation domain along with simulation results of Wu et al [24].

Rigid body theory gives the transferred angular velocity, ω_r, as [10, 17]:

$$\omega_r = \frac{P_t R}{mk^2} \tag{3.6}$$

where P_t is the tangential impulse, R is the radius of the particle, m is the particle's mass and k is the radius of gyration of the particle. In the case of spherical particles Equation 3.6 can be rewritten as:

$$\omega_r = \frac{5}{2R}\left(V_{ti} - V_{tr}\right) \tag{3.7}$$

F. Mohammadi and J. Luo,Corros. Sci. 52 (2010) 2994-3001.

Figure 3.5 shows a plot of e_t against particle impact angle. It is observed that the tangential coefficient of restitution reaches a minimum at impact angles around 60° and later increases as the impact angle increases to normal. This indicates that a higher percentage of energy was dissipated due to particle velocity in the tangential direction at impact angles around 60 °. Since the shapes of the craters from different impact angles are not different, this can be attributed to the frictional forces in the contact patch. These forces are still not high enough to extensively deform the surface in the tangential direction and create a lip on the samples; however, they are large enough to depassivate the surface and damage the thin oxide layer on the surface. As the impact angle increases, the applied force on the surface in the normal direction increases. This increases the frictional resistance of the contact patch and it becomes more difficult for the particle to overcome this resistance and slide; thus more energy is dissipated in the tangential direction and the coefficient of restitution is decreased. Using Equation 3.7 the transferred tangential velocity to the particle was calculated for different impact conditions and the results are plotted in Figure 3.5.

From Equation 3.6 and results shown in Figure 3.5, it can be concluded that the tangential impulse that worked along the contact area between the particle and the surface reaches its maximum at an impact angle around 60°. Knowing this, when at lower impact angles the sliding between particle and surface is considered, the normal and tangential impulses can be correlated as [28]:

$$P_t = \mu . P_n \tag{3.8}$$

F. Mohammadi and J. Luo,Corros. Sci. 52 (2010) 2994-3001.

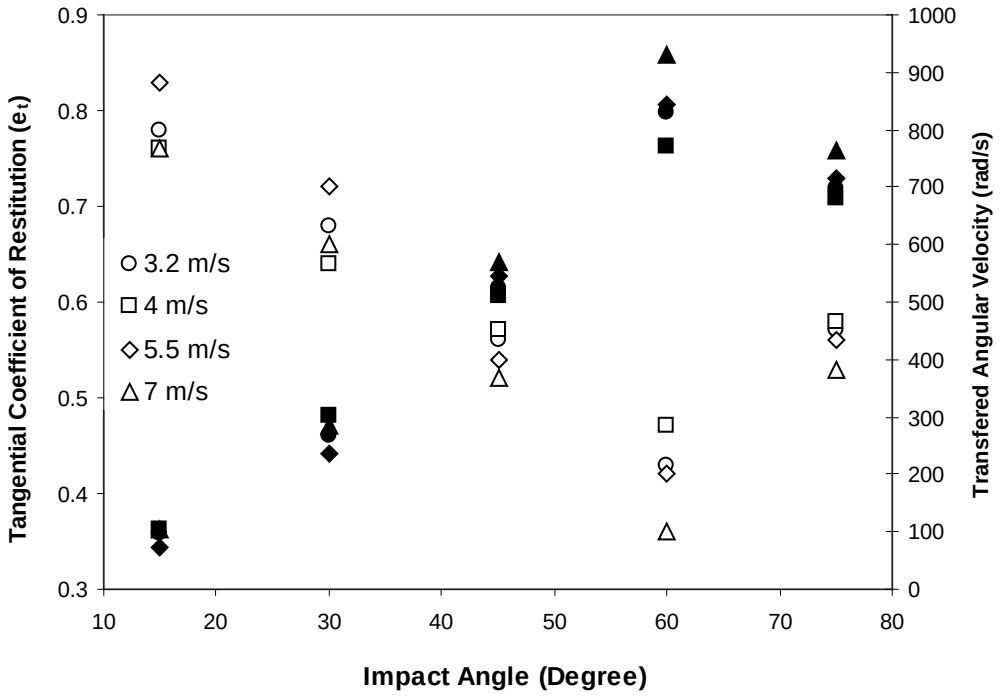

Figure 3-5 Tangential coefficient of restitution and transferred angular velocity as a function of impact angle for zirconia particles impacting 304 stainless steel surface at different velocities (points with dark background represent the transferred angular velocity).

where P_n is the impulse in the normal direction and μ is the ratio of the tangential to normal impulses. Equation 3.8 can be rewritten as [17]:

$$\mu = \left(\frac{1 - e_t}{1 + e_n} \right) . \cot \theta_i \qquad (3.9)$$

Figure 3.6 is a plot of e_t against $(1+e_n).\mathrm{tg}\vartheta_i$ for zirconia particles. As shown in this plot, for the results obtained at 3.2 m/s impact velocity of zirconia particles, a line was perfectly fitted to the first three data points, which correspond to impact angles up to 45 °.

F. Mohammadi and J. Luo,Corros. Sci. 52 (2010) 2994-3001.

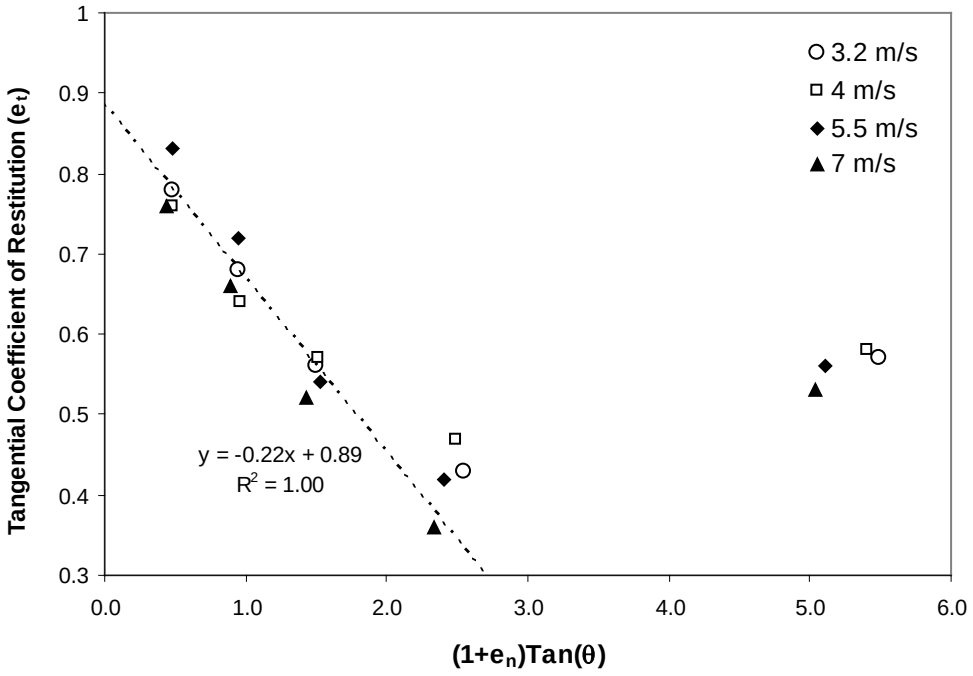

Figure 3-6 Tangential coefficient of restitution as a function of (1+en).tgϑ for zirconia particles impacting 304 stainless steel surface at different velocities.

Lines, with very similar slopes, can be fitted to the first three data points for other impact velocities shown in Figure 3.6. When the impact angle was further increased to 60 ^{o} the experimental points started to deviate from the linear fit. This plot reveals that the slope of the line that fits data points up to 45 ^{o} did not differ very much for the different velocities that were used in these experiments. According to Equation 3.8, the slope of this line can be referred to as the ratio of the tangential and normal impulses or in the case of sliding, the coefficient of friction.

F. Mohammadi and J. Luo,Corros. Sci. 52 (2010) 2994-3001.

3.3.2 Electrochemical response of the material to the impacts

To study the electrochemical response of the surface to a single particle impact, samples were held at 200 mV (vs. SCE) for 600 seconds before single particle impacts. Current transients were recorded as a function of time; thus the area below the current transient curve represents the consumed charge during repassivation. The larger the peaks of the current transients, the larger the consumed charges during repassivation. Figure 3.7 shows the current transient peak values as a function of the particle impact angle at different velocities for zirconia and silicon nitride particles. As apparent from Figure 3.7 the maximum amount of charge that was consumed during repassivation was detected at 30^{o} impact angle for all four impact conditions.

The passive film on 304 stainless steel is a very thin layer with a thickness in the order of nanometres [29, 30]. Thus, it is very reasonable that the tangential force, acting on the surface during the impact, can be responsible for the passive film partial damage or its complete removal from the surface in the contact area. Also the particle angular velocity before impact may have an effect on the extent of depassivation and so it may influence the erosion enhanced corrosion rate.

A simple comparison between Figure 3.5 and Figure 3.7 indicates that although the maximum impulse that was transferred to the particle during impact was noticed at a 60^{o} impact angle, the charge that was consumed during repassivation was not maximum at this impact angle. This implies that the extent of impulse on the surface was not the only parameter that was affecting the surface depassivation.

F. Mohammadi and J. Luo,Corros. Sci. 52 (2010) 2994-3001.

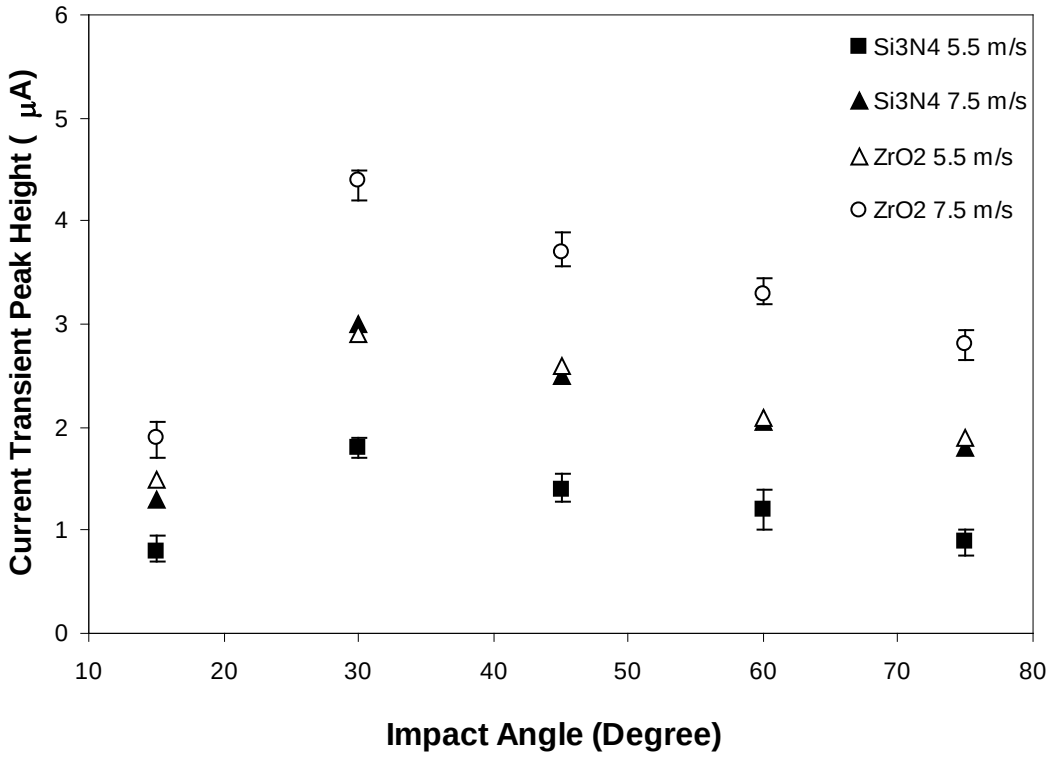

Figure 3-7 **Current transient height as a function of impact angle for zirconia and silicon nitride particles impacting 304 stainless steel surface at 200mV$_{SCE}$ at different velocities.**

In pursuance of investigating the effect of particle pre-impact angular velocity on depassivation of the surface, the graph in Figure 3.8 can be used. Because of the design method and characteristics of the single impingement device that was used in these experiments, single particles that were impacting the surface had different angular velocities before impact.

Two pistons were used to introduce the single particles into the fluid stream. Because this process was not automated, the periods in which the particles were being pushed to the stream by pressing the piston were slightly different.

F. Mohammadi and J. Luo,Corros. Sci. 52 (2010) 2994-3001.

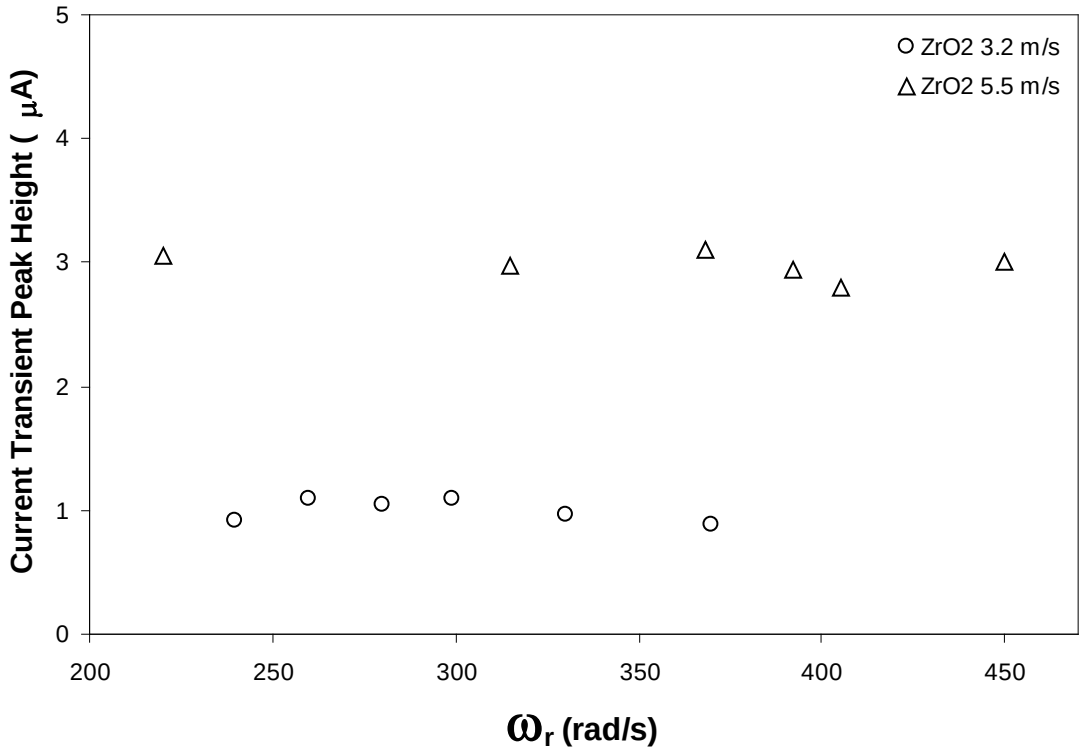

Figure 3-8 Current transient height as a function of particle's pre impact angular velocity for zirconia particles impacting 304 stainless steel surface at different velocities.

This difference in pressing time caused different pre-impact angular velocities in different particles. This created the opportunity of having single impacts with different pre-impact angular velocities, but similar linear velocities and impact angles. Some of the particles were marked before experiments which made it possible to experimentally measure pre-impact and after-impact angular velocities.

Figure 3.8 depicts several impacts at 30^{o} impact angle with 3.2 m/s and 5.5 m/s linear impact velocities; however, the pre-impact angular velocities were different. It can be concluded from Figure 3.8 that the pre-impact angular velocity did not have a

F. Mohammadi and J. Luo,Corros. Sci. 52 (2010) 2994-3001.

significant effect on the depassivation process at the low impact velocities that were used in these experiments.

3.3.3 Assumption of the average forces and the dissipated kinetic energy during the impact

According to Figure 3.6, the ratio of the tangential and normal impulses in all four cases of the impact did not change significantly with changing impact velocity. From 3.5 m/s to 7.5 m/s the current transient peaks increase three times while μ remains almost constant. In chapter 2, it was shown that for a constant particle impact angle, during a single particle impact the consumed charge during repassivation had a linear correlation with the kinetic energy of the particle at lower velocities up to 10 m/s. Figure 3.9 is a plot of the consumed charge during repassivation against the lost kinetic energy of the particle due to the change of velocity in the normal direction. It is apparent from this plot that more charge is consumed during repassivation as a particle loses more kinetic energy during the impact. This part of the particle kinetic energy is mostly lost due to plastic deformation occurring on the surface. It was also shown that lip formation during the impact is negligible because of the low velocity range that is used. Thus the crater formation can be attributed to the normal component of the velocity and the corresponding kinetic energy loss. Assuming an average flow pressure σ_n due to the change of velocity in the normal direction during plastic deformation of the surface, one can write:

F. Mohammadi and J. Luo,Corros. Sci. 52 (2010) 2994-3001.

$$\Delta K_n = \int_0^{V_C} \sigma_n .\mathrm{d}v = \frac{1}{2} m\left(V_{\mathrm{ni}}{}^2 - V_{\mathrm{nr}}{}^2\right) \qquad (3.10)$$

where ΔK_n is the lost kinetic energy due to the change of particle velocity in the normal direction, V_C is the final crater volume and dv is the change in the crater volume.

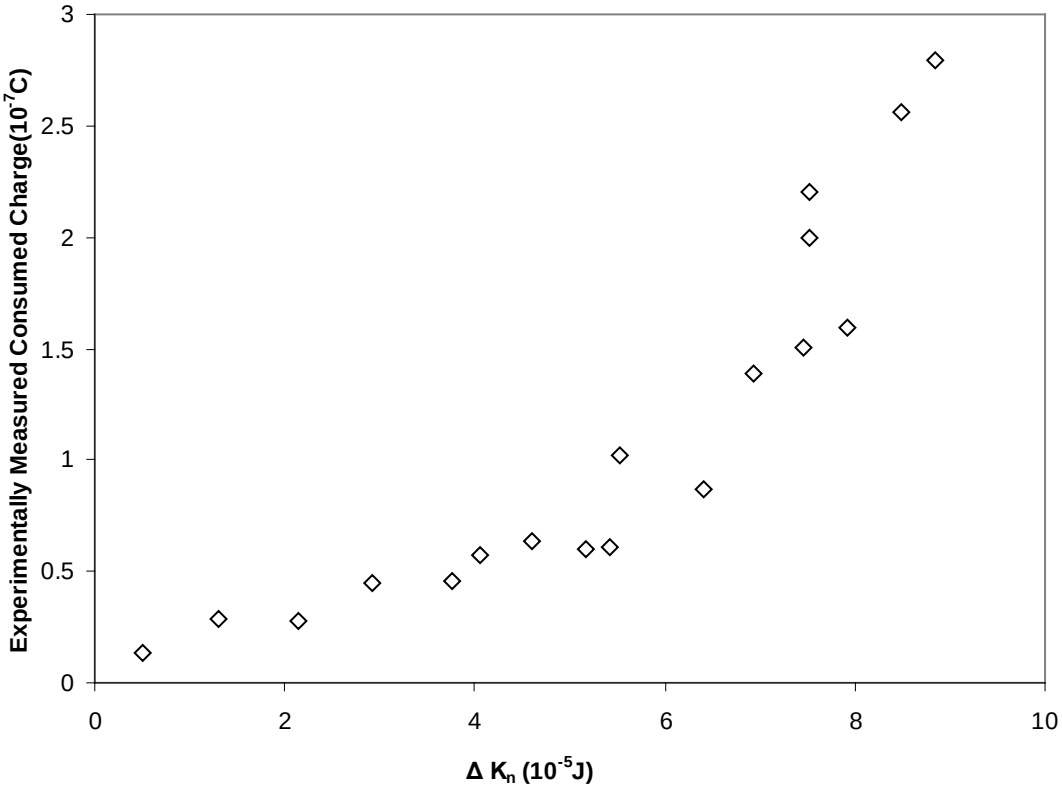

Figure 3-9 Experimentally measured consumed charge during repassivation vs. ΔK_n for zirconia and silicon nitride particles at different impact velocities.

If an average force in the normal direction is assumed to be present between the surface and the particle along the contact patch during impact, ΔK_n can be referred to as the work done by the average normal force during crater formation along its path which will be the crater's depth, h_C;

F. Mohammadi and J. Luo,Corros. Sci. 52 (2010) 2994-3001.

$$\Delta K_n = \int_0^{h_C} F_n . \mathrm{d}h = \overline{F_n} . h \qquad (3.11)$$

where d*h* is the change in the depth of the crater, F_n is the force in the normal direction and $\overline{F_n}$ is the average force in the normal direction. Both the average force and the scar depth change by altering the lost kinetic energy. In this study, it was possible to determine how the scar depth changed with the lost kinetic energy. Thus, experimental results of the depth of the crater formed after impact against the lost kinetic energy were plotted in Figure 3.10.

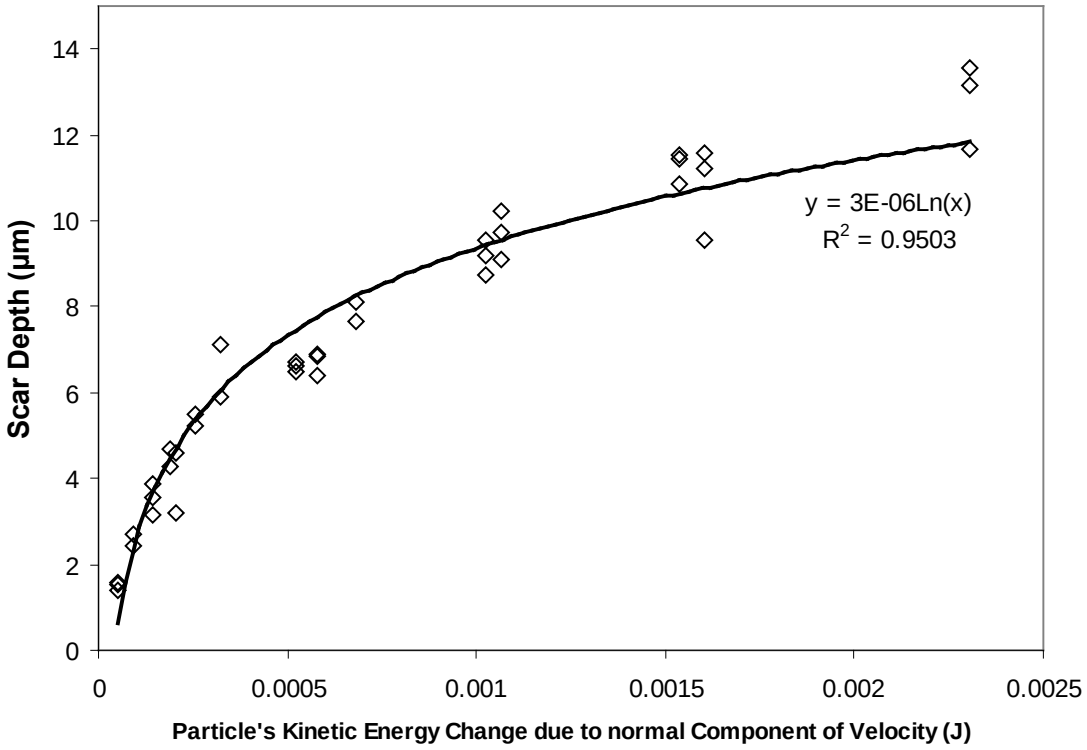

Figure 3-10 Scar depth as a function of particle kinetic energy due to the velocity change in the normal direction for impact of silicon nitride and zirconia particles with 2.38mm diameter at velocities from 5m/s to 12m/s.

F. Mohammadi and J. Luo,Corros. Sci. 52 (2010) 2994-3001.

These results imply that regardless of the impact angle and the velocity of the impact, the crater's depth has an exponential correlation with ΔK_n. When *h* in Equation 3.11 is replaced with its experimental substitute according to Figure 3.10, then;

$$\bar{F}_n = 3.33 * 10^5 \frac{\Delta K_n}{\ln \Delta K_n} \qquad (3.12)$$

From the form of Equation 3.12 it is apparent that at values for ΔK_n sufficiently less than unity, the term $\Delta K_n / \ln \Delta K_n$ will take the form of a line which is tangent to the horizontal axis. Since the values of ΔK_n for the single impacts in this study were very small due to the low impact velocities and the small sizes of the particles, a linear correlation between lost kinetic energy of the particles and $\overline{F}_n$ was expected. Figure 3.11 depicts a plot of the experimental data points for the average forces calculated through Equation 3.11 and the lost kinetic energy that was experimentally measured using the high speed camera. As apparent from Figure 3.11, a perfectly linear correlation was observed between the two quantities. Note that the amounts of ΔK_n in Figure 3.11 are very small and this chart is only a small region of the $\Delta K_n / \ln \Delta K_n$ curve.

$\overline{F}_n$ can be used to calculate a corresponding average tangential force, $\overline{F}_t$, which will act along the contact area between the particle and the surface in the tangential direction. Thus, according to Equation 3.8, and since μ was shown to be a constant in Figure 3.6, a linear correlation between the two average forces in the normal and tangential directions exists. Thus, the correlation between ΔK_n and the average tangential force will also be linear.

F. Mohammadi and J. Luo,Corros. Sci. 52 (2010) 2994-3001.

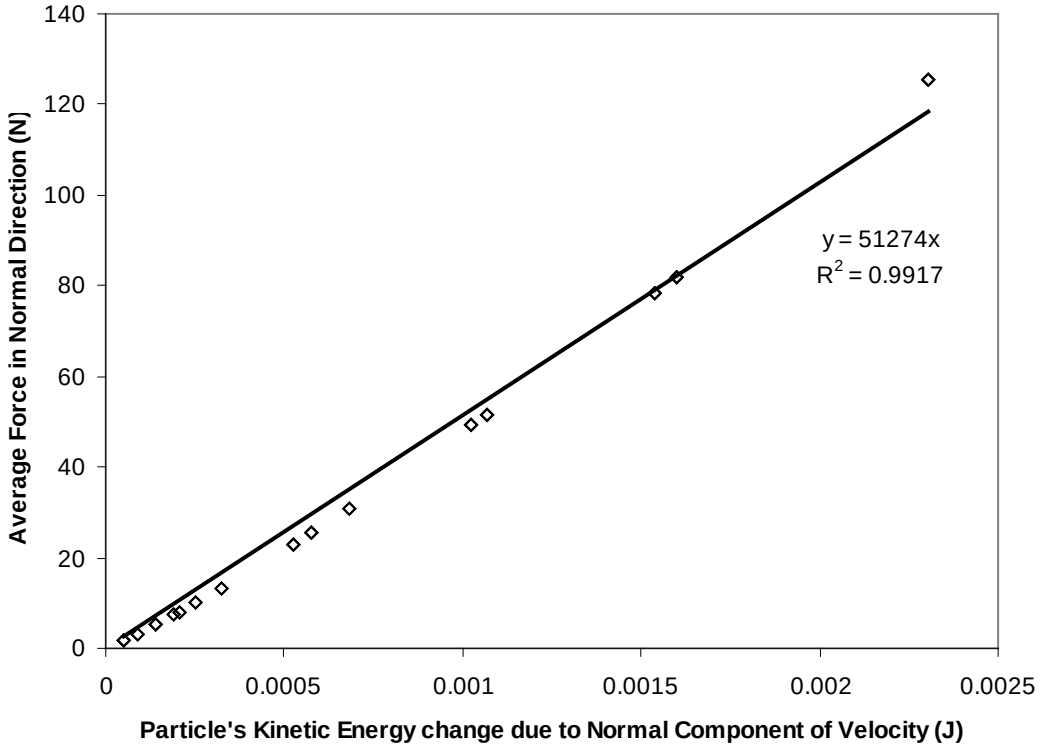

Figure 3-11 Average force applied in the normal direction during impact of zirconia and silicon nitride particles with 2.38mm diameter on 304 stainless steel surface as a function of particle's kinetic energy change due to change of velocity in the normal direction at impact velocities from 5m/s to 12m/s.

Since the extent of the plastic deformation that occurs on the surface is low according to Figure 3.4 and μ is a constant according to Figure 3.6, hereinafter, μ is considered to be an equivalent of the coefficient of friction between the two surfaces and thus the tangential force will be a designation of the friction force [28].

Figure 3.9 shows the correlation between the consumed charge during repassivation and ΔK_n of the impacting particles at lower velocities. This finding along with the results shown in Figure 3.11 indicate that, at a constant particle impact angle, consumed charge during repassivation increases with an increase in the average friction

F. Mohammadi and J. Luo,Corros. Sci. 52 (2010) 2994-3001.

force acting on the surface during the particle impact. Keeping this concept in mind, it can be concluded that the friction force between the particle and the surface becomes maximum at higher impact velocities for a constant impact angle. Two contradictory results are at hand:

(1) By comparing Figures 3.7, 3.9 and 3.11, an increase in friction force with the lost kinetic energy of the particles at a constant impact angle is observed, which implies that friction force significantly affects depassivation of the surface.

(2) By comparing Figures 3.5 and 3.7, it is found that friction force at a constant impact velocity becomes maximum at higher impact angles while the consumed charge during repassivation reaches its maximum at 30^{o} impact angle. This implies that the effect of friction force on the depassivation process may not be significant.

The above mentioned contradictions indicate that, other than a friction force, a different factor is present that simultaneously affects the extent of depassivation of the surface. In view of the above observations, the following approach was used to further analyze and clarify the correlation between the friction force and depassivation.

Formerly, $\overline{F}_t$ was assumed to be acting along the contact area between the particle and the surface. It was also previously noted that the nature of the impact of a single particle on the surface is very complicated and the details of the contact patch at different intervals after the start of the impact are even more difficult to define. Thus, it is more convenient to deal with this problem by assuming an effective action path, d_{eff}, for $\overline{F}_t$. This means that the relative displacement of the particle during the sticking, sliding and rolling periods of the contact event between the particle and the surface is

F. Mohammadi and J. Luo,Corros. Sci. 52 (2010) 2994-3001.

averaged to an effective path of action for the average friction force. This assumption is based on an experimental finding in chapter 2 implying that sinking in and piling up are negligible at the lower velocities used in these experiments.

Based on the previous assumptions, the change in the kinetic energy due to the variation of the velocity in the tangential direction or, in other words, the lost kinetic energy due to the change of velocity in the tangential direction, ΔK_t, can be accounted for by the work that is done by $\overline{F}_t$ along the effective particle-surface contact path during the impact. The effective contact path is different from the scar dimension and is calculated by dividing ΔK_t by $\overline{F}_t$, Thus two correlations exist as follows:

$$\Delta K_t = \int_0^{d_{eff}} F_t . \mathrm{d}x = \overline{F_t} . d_{eff} \qquad (3.13)$$

$$\Delta K_t = \frac{1}{2} m \left(V_{ti}^{\ 2} - V_{tr}^{\ 2} \right) \qquad (3.14)$$

where dx is the change in the effective path of action for the friction force and F_t is the friction force. Since ΔK_t is known due to the high speed camera velocity measurements and $\overline{F}_t$ is the product of the friction coefficient and average force in the normal direction that was shown in Figure 3.11, d_{eff} can be calculated for different impact angles by solving Equations 3.13 and 3.14 simultaneously. Figure 3.12 is a plot of the effective particle-surface contact path against the particle impact angle. It can be seen that the effective contact path was a maximum at 15^o impact angle and decreased to a minimum value towards normal angles.

F. Mohammadi and J. Luo,Corros. Sci. 52 (2010) 2994-3001.

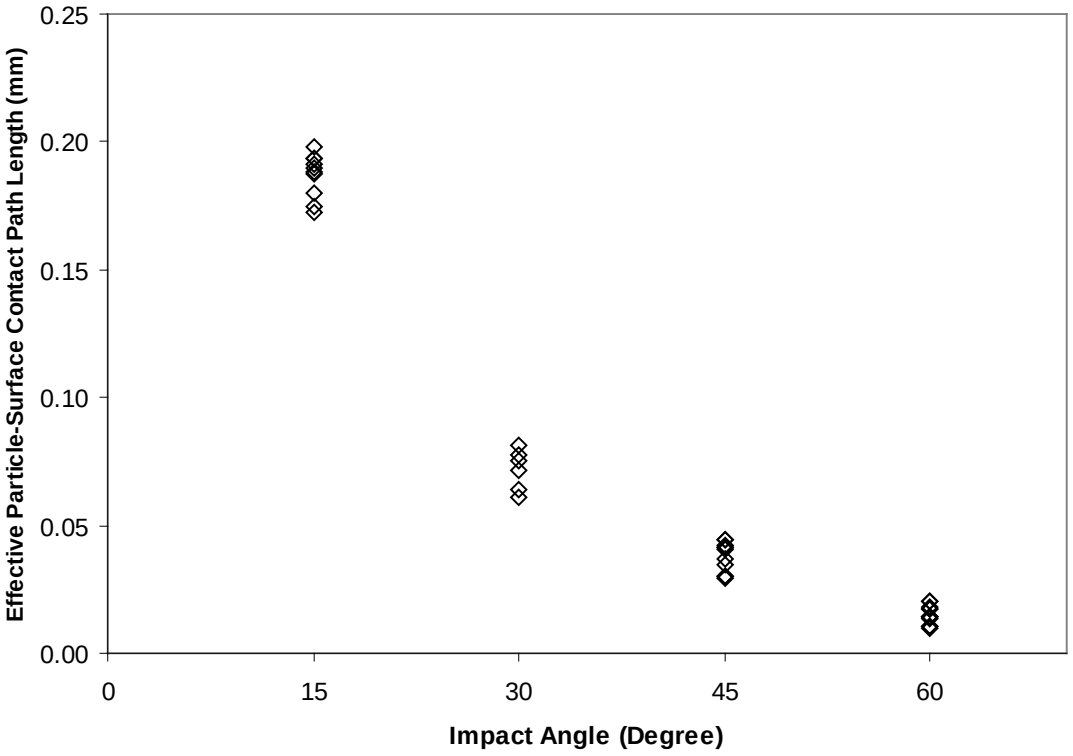

Figure 3-12 Effective particle-surface contact path length vs. particle's impact angle for zirconia particles impacting on 304 stainless steel surface at different velocities.

3.3.4 Depassivation mechanism

Considering the former concepts and discussions, the following mechanism can be proposed for the phenomenon that was observed in Figure 3.7.

At the low impact velocities experienced in this study, as the particle impact angle increases from 0^o to 90^o according to Figure 3.13:

(1) The friction force acting along the contact path increases from zero to larger values, but it is still not high enough to effectively depassivate the surface along the contact path.

F. Mohammadi and J. Luo,Corros. Sci. 52 (2010) 2994-3001.

(2) The contact path length decreases from its maximum to shorter lengths.

(3) At a critical impact angle between 15^{o} and 30^{o}, the friction force becomes high enough to effectively depassivate the surface along the contact path while this path is still larger than that at higher impact angles. Thus, the most surface area is affected at this impact angle while the effective force is reached and so the maximum depassivation and erosion enhanced corrosion rate is observed.

(4) As the impact angle is increased from its critical value, the friction force is increased, but its effectiveness does not change very much. At the same time the contact path is decreased and a lower surface area is affected by the friction force compared to the critical impact angle. Thus lower depassivation occurs and the erosion enhanced corrosion rate is decreased.

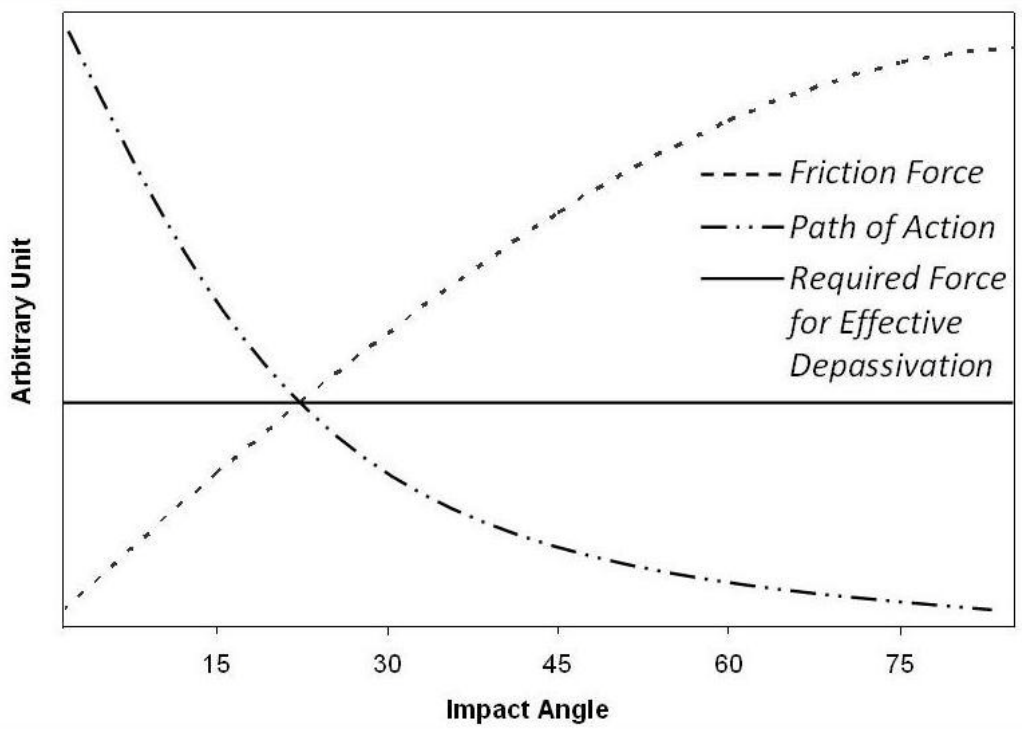

Figure 3-13 Schematic representation of the proposed mechanism for surface depassivation.

F. Mohammadi and J. Luo,Corros. Sci. 52 (2010) 2994-3001.

It can be concluded that by changing the particle impact angle from normal angles to oblique angles, the magnitude of the average friction force between the particle and the surface during the impact is decreased; however, the average path that this force acts along the surface is increased. This means that one efficient way of reducing the erosion enhanced corrosion is through reduction of the friction force between the two surfaces in contact.

3.4 Conclusions

(1) Normal and tangential coefficients of restitution and their dependence on the particle impact angle were calculated for a single particle impacting a flat passive metal surface under flow of an aqueous solution.

(2) It was found that the maximum tangential impulse was transferred to particles at impact angles around 60^{o}.

(3) Based on the results of this study, it is apparent that the pre-impact angular velocity of the particle does not have a significant effect on the extent of the consumed charge during repassivation and thus erosion enhanced corrosion of the surface.

(4) The charge consumed during the repassivation process increases by an increase in the average normal force present at the contact patch between the particle and the surface during the particle impact.

(5) An average friction force acts along an average contact path between the particle and the surface during the impact, and the length of this action path becomes larger at lower impact angles where depassivation of the surface is more pronounced.

F. Mohammadi and J. Luo,Corros. Sci. 52 (2010) 2994-3001.

3.5 References

[1] R.J.K. Wood, Erosion–corrosion interactions and their effect on marine and offshore materials, Wear 261 (2006) 1012-1023.

[2] I. Finnie, The mechanism of erosion of ductile metals, Proc. of 3rd U.S. Natl. Congr. of Appl. Mech. ASME, NewYork (1958) 527–532.

[3] I. Finnie, G.R. Stevick and J.R. Ridgely, The influence of impingement angle on the erosion of ductile metals by angular abrasive particles, Wear 152 (1992) 91–98.

[4] J.G. Chacon Nava, F.H. Stott and M.M. Stack, The effect of substrate hardness on the erosion-corrosion resistance of materials in low-velocity conditions, Corros. Sci. 35 (1993) 1045-1051.

[5] J.B. Zu, I.M. Hutchings and G.T. Burstein, Design of a slurry erosion test rig, Wear 140 (1990) 331–344.

[6] Y. Li, G.T. Burstein and I.M. Hutchings, The influence of corrosion on the erosion of aluminium by aqueous silica slurries, Wear 186–187 (1995) 515–522.

[7] G.T. Burstein and K. Sasaki, Effect of impact angle on the slurry erosion–corrosion of 304L stainless steel, Wear 240 (2000) 80-94.

[8] P. Novak and A. Macenauer, Erosion-corrosion of passive metals by solid particles, Corros. Sci. 35 (1993) 635-640.

[9] K. Sasaki and G.T. Burstein, Erosion–corrosion of stainless steel under impingement by a fluid jet, Corros. Sci. 49 (2007) 92-102.

[10] F. Mohammadi, J. Luo, B. Lu and A. Afacan, Single particle impingement current transients for prediction of erosion-enhanced corrosion on 304 stainless steel, Corros. Sci. (2010), doi:10.1016/j.corsci.2010.03.007.

[11] A.J. Smitha, M. Stratmann and A. W. Hassel, Investigation of the effect of impingement angle on tribocorrosion using single impacts, Electrochim. Acta 51 (2006) 6521-6526.

[12] G.T. Burstein and K. Sasaki, Detecting electrochemical transients generated by erosion–corrosion, Electrochim. Acta 46 (2001) 3675–3683.

[13] A.W. Hassel and A. J. Smith, Single particle impact experiments for studying particle induced flow corrosion, Corros. Sci. 49 (2007) 231–239.

[14] A.H. Kharaz, D. A. Gorham and A. D. Salman, An experimental study of the elastic rebound of spheres, Powder Technol. 120 (2001) 281-291.

[15] D.A. Gorham and A. H. Kharaz, The measurement of particle rebound characteristics, Powder Technol. 112 (2000) 193-202.

[16] A.H. Kharaz, D. A. Gorham and A. D. Salman, Accurate measurement of particle impact parameters, Meas. Sci. Technol. 10 (1999) 31-35.

[17] R. sondergaard, K. Chaney and C. E. Brennen, Measurements of solid spheres bouncing off flat plates, J. Appl. Mech., Transactions ASME 57 (1990) 694-699.

[18] H. Dong and M. H. Moys, Experimental study of oblique impacts with initial spin, Powder Technol. 161 (2006) 22-31.

[19] W.J. Stronge, R. James and B. Ravani, Oblique impact with friction and tangential compliance, Philos. Trans. R. Soc. London, Ser. A 359 (2001) 2447-2465.

[20] G.T. Burstein and K. Sasaki, Detecting electrochemical transients generated by erosion-corrosion, Electrochim. Acta 46 (2001) 3675-3683.

[21] M. Matsumura, Y. Oka, H. Hiura and M Yano, The role of passivating film in preventing slurry erosion-corrosion of austenitic stainless steel, ISIJ Int. 31 (1991) 168-176.

[22] X. Tanga, L.Y. Xua and Y.F. Cheng, Electrochemical corrosion behavior of X-65 steel in the simulated oil sand slurry. II: Synergism of erosion and corrosion, Corros. Sci. 50 (2008) 1469-1474.

[23] A.A. Torrance, An explanation of the hardness differential needed for abrasion, Wear 68 (1981) 263-266.

[24] L-Y. Li, C-Y. Wu and C. Thornton, A theoretical model for the contact of elastoplastic bodies, J. Mech. Eng. Sci. 216 (2002) 421-431.

[25] C-Y. Wu, C. Thornton and L-Y. Li, A semi-analytical model for oblique impacts of elastoplastic spheres, Proc. R. Soc. London, Ser. A 465 (2009) 937-960.

[26] C-Y. Wu, L-Y. Li and C. Thornton, Rebound behaviour of spheres for plastic impacts, Int. J. Impact Eng. 28 (2003) 929-946.

[27] L. Labous, A. D. Rosato and R. N. Dave, Measurements of collisional properties of spheres using high speed video analysis, Phys. Rev. E 56 (1997) 5717-5725.

[28] R.M. Brach, Mechanical Impact Dynamics: Rigid Body Collision, John Wiley & Sons, New York, 1991.

[29] G.M. Bulman and A.C.C. Tseung, An ellipsometric study of passive film growth on stainless steel, Corros. Sci. 13 (1973) 531-544.

[30] M.E. Curley-Fiorino and G.M. Schmid, The effect of the Cl ion on the passive film on anodically polarized 304 stainless steel, Corros. Sci. 20 (1980) 313-329.

4 Effect of cold work on erosion-corrosion of 304 stainless steel

4.1 Introduction

Degradation of materials due to erosion-corrosion is a major problem in many industries especially those involved with fossil fuel transportation and processing. In comparison to erosion and corrosion individually, the synergistic action of their combination can increase the degradation rate of materials up to two times [1]. Both erosion and corrosion enhance each other; thus, the erosion-corrosion synergism can be divided into two parts: erosion enhanced corrosion and corrosion enhanced erosion. Many factors that influence the wear due to erosion-corrosion have been previously studied such as impact angle, impact velocity, solid loading in the slurry, corrosivity of the slurry, and shape and hardness of the materials in contact [2-7].

In previous chapters, it was determined that the consumed charge during repassivation of 304 stainless steel caused by single particle impact, indicative of erosion enhanced corrosion, was linearly correlated to the kinetic energy of that particle at low impact velocities. The consumed charge during repassivation was used to predict the erosion enhanced corrosion of 304 stainless steel, which was exposed to low velocity slurries with low sand concentrations where the particle interactions are not significant [8]. Burstein and Sasaki reported a threshold kinetic energy for the impacting particles below which passive film rupture was not observed during flow of slurry on the surface of 304 stainless steel [9].

F. Mohammadi and J.L. Luo, Corros. Sci., doi:10.1016/j.corsci.2010.09.059.

We have previously shown that the friction force acting on the surface during the impact and its effective path of action played a significant role in determining the extent of depassivation and erosion enhanced corrosion. The normal component of impact velocity, which is the indenting component, was shown to be mostly responsible for the shape and the size of the scars at the low velocities that were used. It was also shown that the depth of the scars formed due to single impact is correlated logarithmically to the change in the particle kinetic energy due to the change of the normal component of its velocity [10].

It has been previously proposed that the energy required for indentation of materials is a constant and does not depend on the impact velocity [11]. In their recently published book, Kleis and Kulu reintroduced this concept [12]. Based on many experimental results, they proposed that this specific energy is a constant and characteristic of materials and can be used to characterize the dynamic hardness of materials. The specific energies required for crater formation are defined as:

$$e_0 = \frac{W_0}{V} \qquad (4.1)$$

where e_0 is the specific energy for crater formation, W_0 with units of Joules (J) is the initial kinetic energy of the particle before impacting the surface and V is the volume of the crater formed after the impact with units of mm^3.

It has been previously shown that the erosion and erosion-corrosion rate of a specific material depend on the relative hardness of that material and the abrasive. Furthermore, although different factors affect the erosion-corrosion of materials with different hardness, harder materials are shown to usually be more resistant to erosion

F. Mohammadi and J.L. Luo, Corros. Sci., doi:10.1016/j.corsci.2010.09.059.

and erosion-corrosion [2, 13]. As a result, different surface treatments and strengthening mechanisms have been previously employed to enhance the erosion-corrosion resistance of materials [13-17]. The single particle impingement method has been previously used to study the effects of impact dynamics, hydrodynamics, corrosivity of the medium and impact angle on the depassivation and erosion-corrosion of passive materials [18, 19].

In the present chapter, both single particle and slurry jet impingement methods were used to quantitatively study the effect of cold work and hardness on the erosion-corrosion of 304 stainless steel.

4.2 Experimental methods

Particle size, impact angle on the surface, velocity of the impact and the medium in which the impacts were occurring could be changed with the use of the single impingement device. A gear pump was used to provide fluid flow at constant pressure. The flow of the fluid was measured by a rotary flow meter and could be adjusted by a controller that was attached to the motor. Particles were introduced to the fluid flow through two pistons; one of them blocked the back flow of the fluid while a particle was loaded from the other. Details of this design were described in chapter 2.

A PCI 8000 Motion Scope high speed camera was coupled to this system. The camera is capable of recording up to 8000 fps; however, a frame rate of 2000 Hz was used in these experiments. Impact and rebound velocities and angles were calculated by analyzing the photo frames that were captured with the camera. Image J software was

F. Mohammadi and J.L. Luo, Corros. Sci., doi:10.1016/j.corsci.2010.09.059.

used to analyze the high speed camera pictures. Sequential photo frames of a single particle impact on the surface and more specific details on the velocity calculations were provided in chapter 3 [8].

A TA-215 Stanat rolling machine was used to perform work hardening by reducing the sample thicknesses to obtain desired reduction percentages. Furthermore, a MVK-H1 Mitutoyo micro-hardness testing machine was used to measure the hardness of the specimens before and after the cold work was applied.

In order to perform the experiments in environments that were similar to the conditions experienced during service, a slurry jet machine was used to impinge water-sand slurries on the surface of the samples [20]. These experiments were performed using slurries at velocities between 5 m/s and 14 m/s. For weight loss comparison, a slurry velocity of 14 m/s was chosen. The fixed solid loading of 5 wt% was also used in all of the slurry erosion-corrosion tests.

All the potentials in these experiments were measured with respect to the saturated calomel electrode (vs. SCE). Also a 4 x 6 cm platinum mesh was used as the counter electrode in all experiments. All of the experiments in this study were conducted at room temperature (22 ˚C).

A three electrode potentiostat, REF 600 Gamry, was attached to the system. The samples were held at desired potentials (200 mV vs. SCE for erosion-corrosion experiments and -850 mV vs. SCE for erosion experiments) and the potentiostat recorded the current transients arising from the surface in response to single and multiple particle impacts. A data acquisition rate of 1000 Hz was chosen since

F. Mohammadi and J.L. Luo, Corros. Sci., doi:10.1016/j.corsci.2010.09.059.

depassivation and repassivation of the surface happen very fast and a large number of data points are required in order to record accurate current transients. One current transient along with the scar that formed on the surface of the sample due to single particle impact were presented in chapter 2.

Samples of 3 x 18 mm were used to perform single particle impact tests and 5 x 8 cm samples were used to perform slurry jet impingement tests. The sample holder in the slurry jet device was specifically designed so that only a circular area of the sample with a diameter equal to the nozzle, 0.25 inch, was exposed to the environment. Thus, only this area was used in the calculation of current densities in slurry jet experiments. All of the samples were cut from original 304 stainless steel sheets that were purchased from AK Steel Corporation. The chemical composition of the steel is shown in Table 4.1. Before running each experiment, samples were ground with a P1200 grit sand paper, washed with distilled water and air dried.

Table 4-1 Alloy composition for 304 stainless steel (wt%)

C	Mn	P	S	Si	Cr	Ni	N
0.08	2	0.045	0.03	0.75	18	8	0.1

Spherical zirconia particles with the average diameter of 2.38 mm were used to perform single particle impingement tests. More details on the size and characteristics of the particles are provided in chapter 2. Silica sand from Lane Mountain Company was mixed with tap water with a pH of 7.7 in order to prepare the slurries for the slurry jet impingement experiments. The reason for choosing tap water for slurry preparation was

F. Mohammadi and J.L. Luo, Corros. Sci., doi:10.1016/j.corsci.2010.09.059.

that it contained similar chemical components as the water used in common oil sands extraction processes. The composition of the water is reported in Table 4.2.

Table 4-2 Composition of the tap water (mg/L).

Al	0.051	Cu	0.003
Cl^-	4.19	Fe	< 0.002
F^-	0.76	Pb	< 0.0005
Cr	< 0.001	Mn	< 0.001

Stable passive films were formed on the sample surfaces after they were held at 200 mV (vs. SCE) which lies in the mid range of passive potential according to the dynamic polarization curve for 304 stainless steel. After 10 minutes of passivation, a current density of 2 $\mu A/cm^2$ was recorded and no further decrease in this current was observed. In order to eliminate the effect of corrosion, some of the experiments were performed at -850 mV (vs. SCE), which is in the cathodic region of the dynamic polarization curve for 304 stainless steel.

4.3 Results and discussion

Similar to many other alloys, 304 stainless steel is susceptible to sensitization and should be corrected especially if the material is to be used in corrosive environments. When a sensitized material is exposed to erosive corrosive conditions, intergranular corrosion along with the difference between the mechanical properties of the grain boundaries and the rest of the material can cause a reduction in the material strength and affect the erosion-corrosion resistance of the material. Therefore, before running experiments, samples were analyzed and X-ray maps of the surface were provided in

F. Mohammadi and J.L. Luo, Corros. Sci., doi:10.1016/j.corsci.2010.09.059.

order to investigate the possible sensitization of samples. The results are shown in Figure 4.1 which shows that samples were not sensitized.

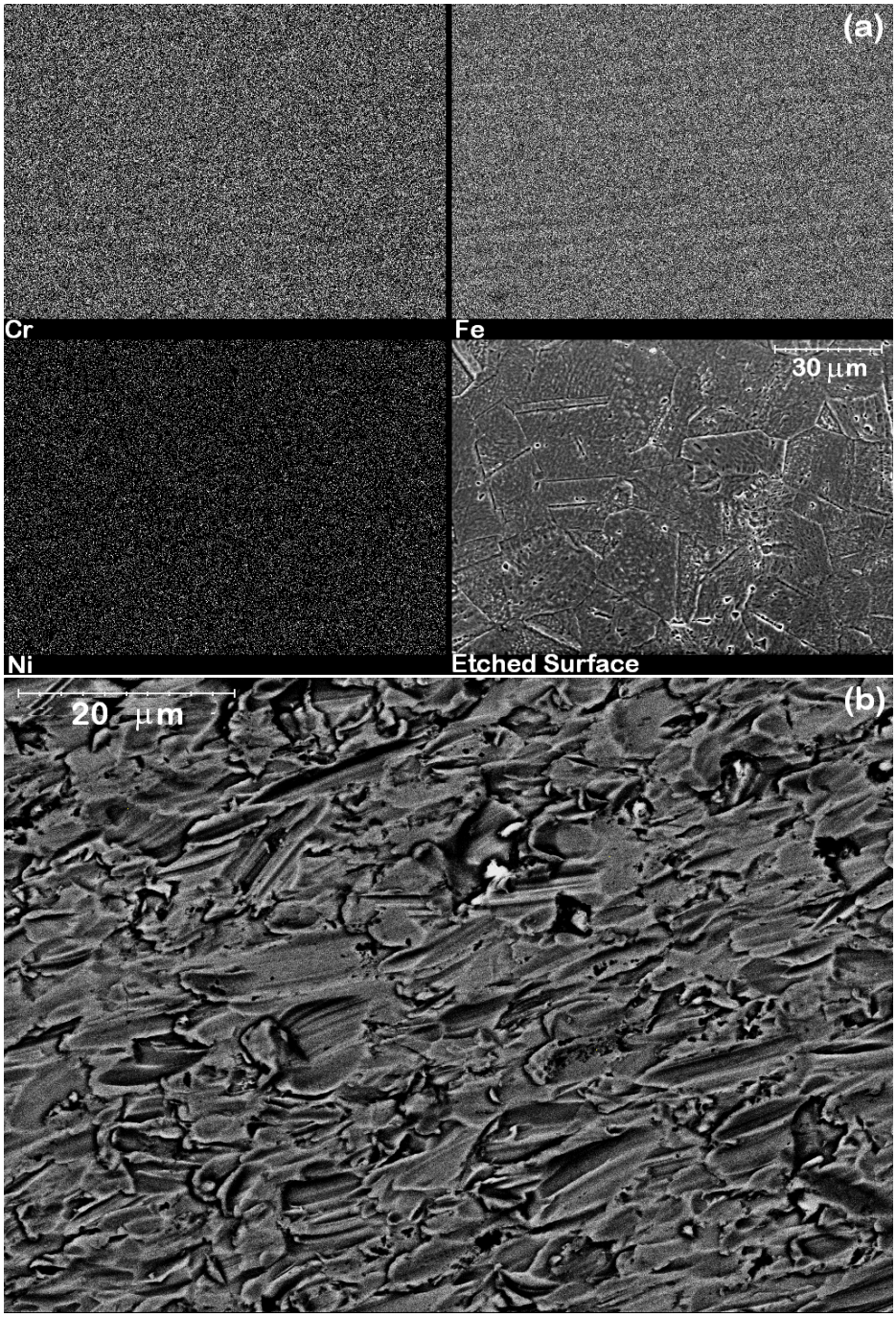

Figure 4-1 (a) X-ray map of Fe, Ni, and Cr for 304 stainless steel samples. (b) SEM of the eroded surface of 304 stainless steel at 30˚ impact angle and 14 m/s slurry velocity.

F. Mohammadi and J.L. Luo, Corros. Sci., doi:10.1016/j.corsci.2010.09.059.

4.3.1 Single particle impact analysis

4.3.1.1 Effects of cold work and hardness

Sheets of 304 stainless steel were cold rolled so that the thickness was reduced by 2.5%, 5%, 10%, 20% and 33% relative to their original thickness. Hereinafter, the thickness reduction percentage will be referred to as the cold work percentage. The Vickers hardness measurements after the rolling process showed an increase in the hardness of the samples as expected. This effect is shown in Figure 4.2.

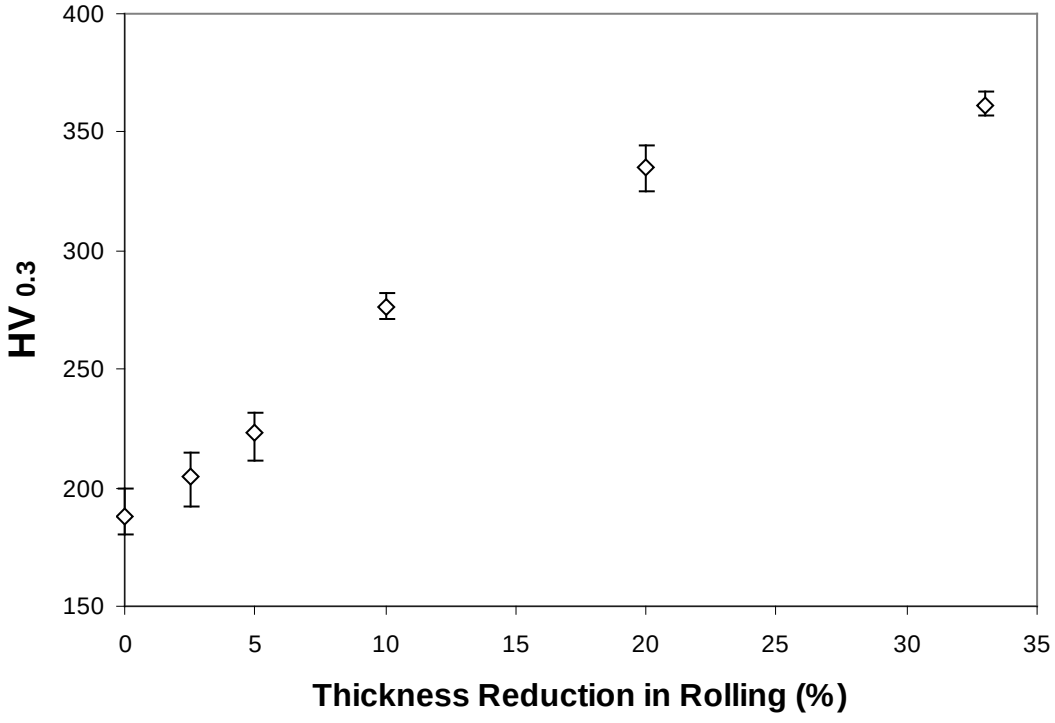

Figure 4-2 Vickers micro hardness of 304 stainless steel samples as a function of cold work percentage (applied load of 0.3 kg for 10 seconds).

Specimens were prepared from as-received and work hardened sheets and single particle impact experiments were performed in aqueous solutions. The kinetic energy of the impacting particle was measured through the analysis of the images that were

F. Mohammadi and J.L. Luo, Corros. Sci., doi:10.1016/j.corsci.2010.09.059.

captured by the high speed camera. On the other hand, optical micrographs of the scars that formed on the surface due to single impacts were used to determine the scar sizes. The specific energies required for crater formation were calculated according to Equation 4.1. Figure 4.3 shows the specific energies of crater formation as a function of impact velocity for samples with different cold work percentages. It is evident that as long as the amount of cold work is not changed, the specific energy of crater formation is not affected by the impact velocity and hence remains constant. These results support the proposal of Kleis and Kulu [12] mentioning that the specific energy of crater formation seems to be a characteristic of the material.

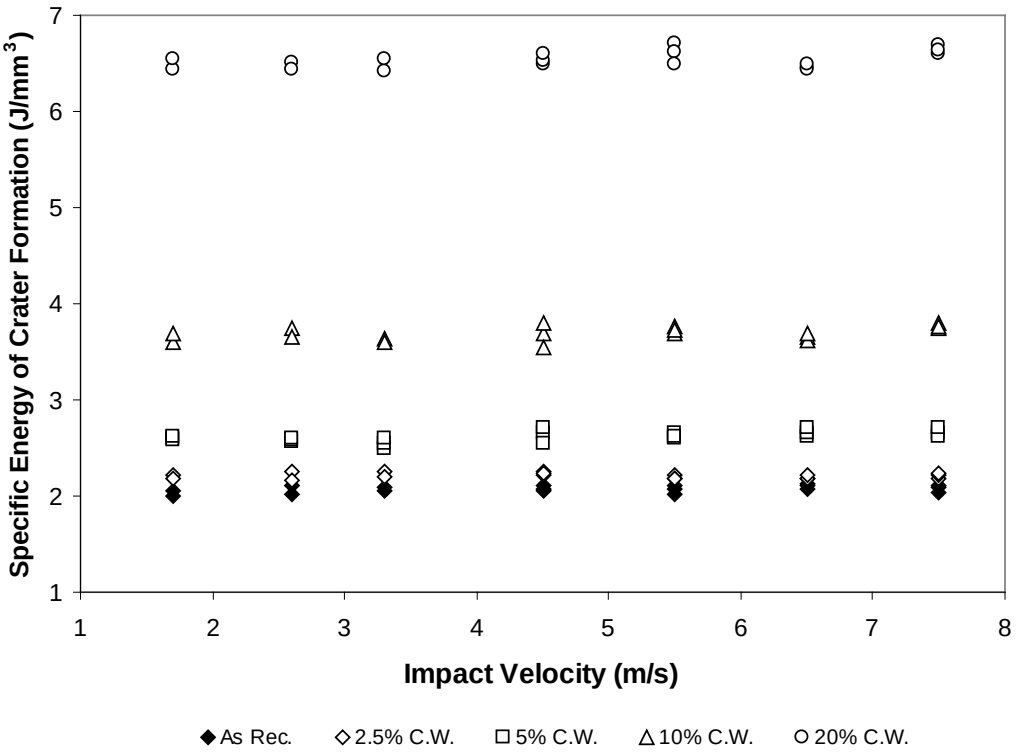

Figure 4-3 Specific energy of crater formation plotted for different cold work percentages as a function of impact velocity.

F. Mohammadi and J.L. Luo, Corros. Sci., doi:10.1016/j.corsci.2010.09.059.

Before particle impact, samples were held at 200 mV (vs. SCE) for 10 minutes while the current passing through their surface was recorded using a REF 600 Gamry. As impact occurs on the surface, the passive film is damaged and a current transient is observed. This current transient can be due to both metallic dissolution and repassivation of the surface; however, the magnitude of this current transient is representative of erosion enhanced corrosion. Figure 4.4 shows the magnitude of current transients as a function of impact angle for samples with different amounts of applied cold work.

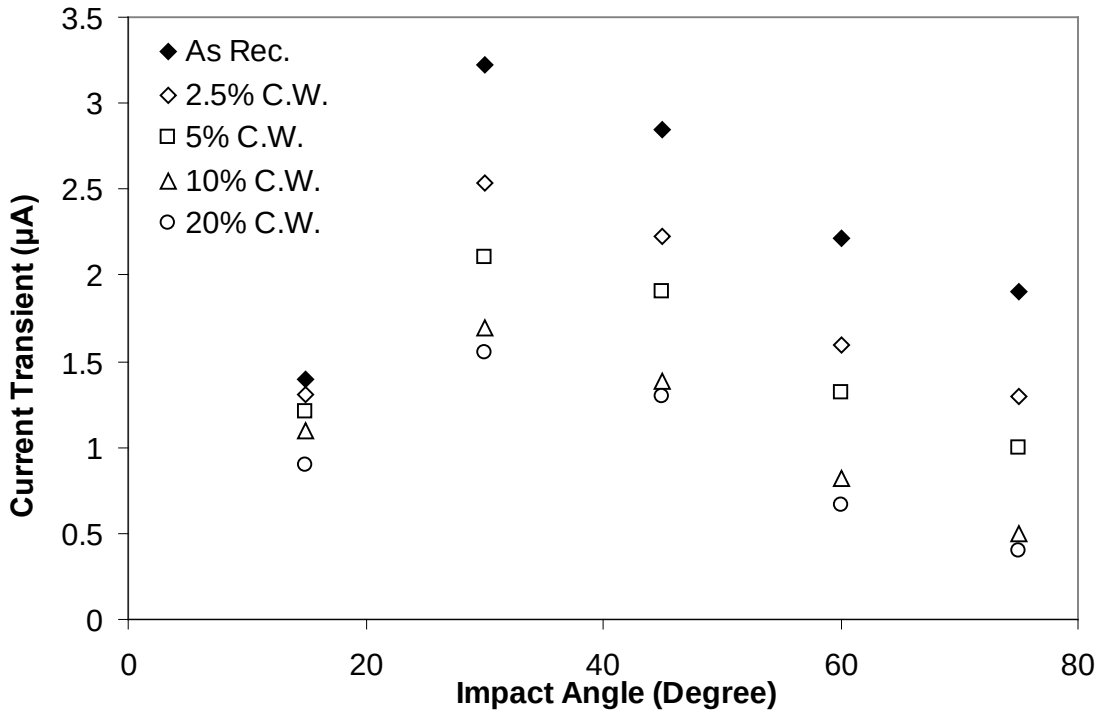

Figure 4-4 Current transients due to zirconia single particle impacts at 6m/s and 200 mV (vs. SCE) for samples with different percentages of cold work as a function of impact angle.

Zirconia particles were impinged on the surface of 304 stainless steel samples at a velocity of 6m/s while the samples were held at 200 mV (vs. SCE). It can be seen that

F. Mohammadi and J.L. Luo, Corros. Sci., doi:10.1016/j.corsci.2010.09.059.

increasing the extent of work hardening decreases the magnitude of current transients. It was previously shown that the shapes of the craters are almost spherical and identical for different impact angles, which is caused by the low velocities used in these studies.

In chapter 2, both the friction force and its effective path of action were shown responsible for the amount of depassivation that occurs on the sample surface. The effective path of action, d_{eff}, was defined as the length of the path along the surface that the friction force acts during the particle impact. As mentioned earlier, since the impact velocities in these experiments were low, the shape of the craters formed due to single particle impacts were almost identical at different impact angles and thus, the effect of tangential force on plastic deformation was not significant. It was also reported that the consumed charge during repassivation is linearly correlated to the kinetic energy of the impacting particles; however, kinetic energy can be consumed in the forms of plastic deformation, friction force and elastic waves; all three can generate heat on the surface during the impact. The effect of elastic waves was previously studied and shown to be insignificant relative to this study. Also it was shown that the calculated repassivation charge due to plastic deformation of the surface is much smaller than the experimentally measured charge consumed during repassivation [8]. Therefore, friction force was considered for depassivation, which then was shown to not be solely responsible for the depassivation. Therefore, the path of its action on the surface during the depassivation process was also studied [10]. Furthermore, the amount of erosion enhanced corrosion of passive materials is affected by the friction force and the effective path.

F. Mohammadi and J.L. Luo, Corros. Sci., doi:10.1016/j.corsci.2010.09.059.

The ratio of the tangential impulse to the normal impulse is defined as the coefficient of friction, μ, and it can be calculated through Equation 4.2 [21]:

$$\mu = \left(\frac{1 - e_t}{1 + e_n} \right) \cot \theta_i \qquad (4.2)$$

where e_n and e_t are the coefficients of restitution in the normal and tangential directions, respectively, and are calculated through Equations 4.3 and 4.4, ϑ is the particle impact angle or more specifically, the angle between the surface and the direction of particle impact.

$$e_n = \frac{V_{nr}}{V_{ni}} \qquad (4.3)$$

$$e_t = \frac{V_{tr}}{V_{ti}} \qquad (4.4)$$

In Equations 4.3 and 4.4, V_{nr} and V_{ni} are the normal components of the rebound and impact velocities, and V_{tr} and V_{ti} are the tangential components of the rebound and impact velocities, respectively. The amount of energy that is dissipated on the surface during the impact is represented by e_n and e_t. Thus, in Figure 4.5, the slopes of the lines are the coefficients of friction for sheets with different amounts of cold work. It is observed that the coefficient of friction is independent of the amount of work hardening that is applied to the material. The decrease in the magnitude of current transients observed in Figure 4.4 can be due to either the friction force or the path over which it acts on the surface. Since the coefficient of friction remains almost constant and does not change with cold work, it can be concluded that the effective path of

F. Mohammadi and J.L. Luo, Corros. Sci., doi:10.1016/j.corsci.2010.09.059.

action of this force changes with cold work and subsequently influences the extent of depassivation of the surface.

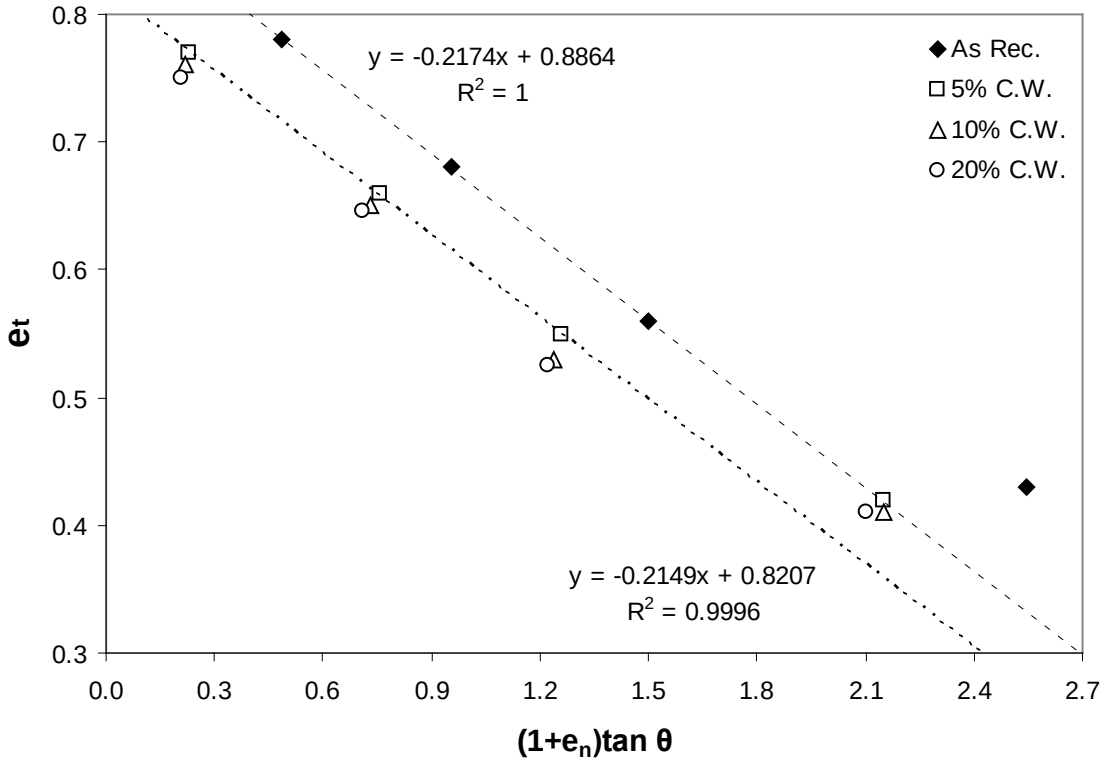

Figure 4-5 Tangential coefficient of restitution as a function of (1+en).tanϑ for zirconia particles impacting 304 stainless steel surfaces with different cold work percentages (slope of the lines are -μ).

4.3.1.2 Evaluation and application of the previous model for depassivation

As described earlier, we proposed a model for depassivation of passive materials due to single particle impacts on the surface. Two average forces were assumed to act along the contact patch during the particle impact: one in the normal direction and one in the tangential direction. The normal force was calculated through experimental measurement of the scar depth and the particle kinetic energy loss due to the normal

F. Mohammadi and J.L. Luo, Corros. Sci., doi:10.1016/j.corsci.2010.09.059.

component of velocity. The coefficient of friction between the two surfaces in contact was also experimentally measured through Equation 4.2, which made calculation of the average tangential force possible. The work of this force was set equal to the experimentally measured particle kinetic energy loss due to the tangential component of velocity. An effective path of action for the average tangential force was calculated through the above procedure and it was found that the length of this path of action plays a significant role in the depassivation process. In this chapter, our previously proposed model is evaluated by more experimental results.

A closer look at Figure 4.4 reveals that, although at each impact angle the magnitude of the current transients is reduced by applying more cold work to the samples, the maxima of the peaks for cold worked samples are still observed at a 30^o impact angle similar to the as received samples. The differences between the magnitudes of the current transients of cold worked samples and the magnitudes of the current transients of as-received samples were calculated and are shown in Figure 4.6. Interestingly, the maxima of these differences are also observed at a 30^o impact angle for all the cases of work hardened steels. Considering that, according to Figure 4.5, the coefficient of friction is constant for all the cases of work hardened samples, the effective path of action for the friction force was calculated for the impacts. The change in the particle kinetic energy due to the change in the tangential component of its velocity, ΔK_f, is set equal to the work of friction force and d_{eff} is calculated.

F. Mohammadi and J.L. Luo, Corros. Sci., doi:10.1016/j.corsci.2010.09.059.

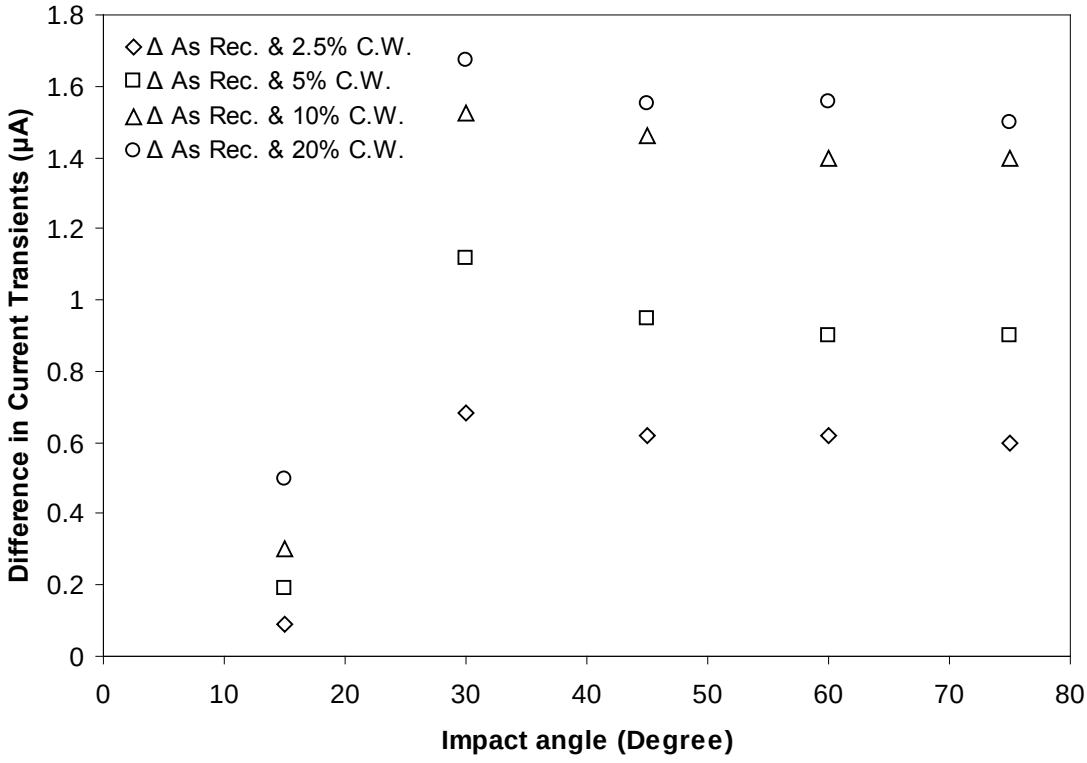

Figure 4-6 Current transient difference with as received samples for samples with different percentages of cold work as a function of impact angle.

The difference between the effective paths of action of the friction force in the impacts on as-received samples and the impacts on cold worked samples, Δd_{eff}, were calculated and are plotted in Figure 4.7. It is observed that Δd_{eff} is maximum for 15^{o} impact angle and progressively decreases at higher impact angles. It is also observed that Δd_{eff} is smaller for impact angles higher than 45^{o} compared to those lower than 45^{o}. The most obvious question is that if Δd_{eff} is mostly responsible for the reduction in current transient magnitude, why is the reduction not significant for the 15^{o} impact angle where Δd_{eff} is maximum? The proposed mechanism may be used again to answer this question.

F. Mohammadi and J.L. Luo, Corros. Sci., doi:10.1016/j.corsci.2010.09.059.

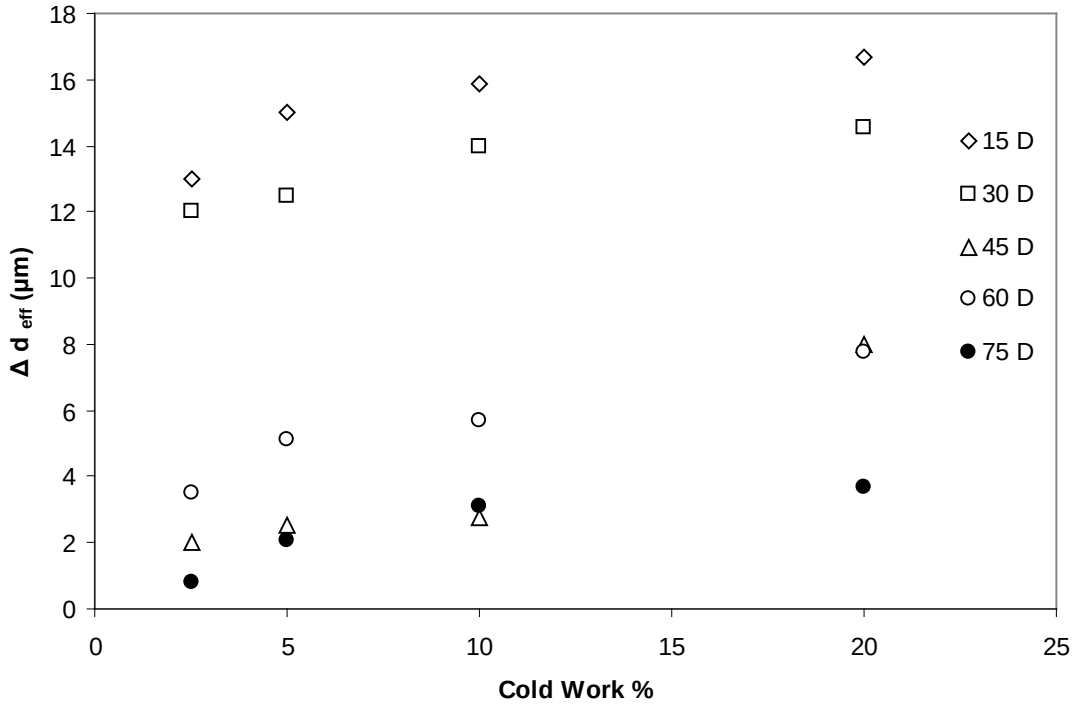

Figure 4-7 Δ d_{eff} , the difference in the effective path of action, as a function of cold work percentage at different particle impact angles.

In the range of velocities examined in this study, the friction force at 15° may not be high enough to effectively depassivate the surface and thus, the effect of Δd_{eff} may be influenced by the effectiveness of the friction force itself. Also from Figure 4.7 it is evident that at a constant impact angle, Δd_{eff} slightly increases as the amount of cold work increases. This explains the reduction in current transient magnitudes that is caused by work hardening.

4.3.2 Slurry erosion-corrosion analysis

In order to further investigate the effect of cold work on erosion-corrosion of 304 stainless steel, more experiments were performed using a slurry jet machine. An

F. Mohammadi and J.L. Luo, Corros. Sci., doi:10.1016/j.corsci.2010.09.059.

impact angle of 30° was chosen for these experiments since the most severe erosion-corrosion has been previously observed at this impact angle [4, 8]. Erosion, corrosion and their synergistic effect were studied separately and the role of the synergism was identified. The total damage was addressed as follows:

$$W_t = W_e^0 + W_c^0 + W_c^e + W_e^c \qquad (4.5)$$

where W_t is the total mass loss, W_e^0 is the mass loss due to erosion free of corrosion and is measured by holding the samples in the cathodic region and gravimetrically calculating their weight loss due to slurry erosion, W_c^0 is the mass loss due to corrosion free of erosion and is measured by measuring the current density of the samples in flowing water with no sand and calculating through the Faraday equation, W_c^e is the mass loss due to corrosion enhanced by erosion, which is calculated similar to W_c^0 only with slurry flowing on the samples, and W_e^c is the mass loss due to erosion enhanced by corrosion and is calculated by deducting the sum of three previous mass losses from the total mass loss while slurry flows on the surface. The sum of the last two parameters is the mass loss due to synergism, W_s.

An analysis of the incorporated errors in the evaluation of erosion-corrosion data is necessary. For W_s, the error can be calculated through:

$$\sigma_S = \sqrt{(\sigma_e^0)^2 + (\sigma_c^0)^2 + (\sigma_c^e)^2 + (\sigma_e^c)^2} \qquad (4.6)$$

where σ_e^0, σ_c^0, σ_c^e and σ_e^v are errors due to corrosion, erosion, corrosion enhanced erosion and erosion enhanced corrosion, respectively, and σ_S represents the error incorporated in the calculation of synergy damage rate. From Equation 4.6, it can be concluded that very accurate measurements are required in order to obtain reliable

F. Mohammadi and J.L. Luo, Corros. Sci., doi:10.1016/j.corsci.2010.09.059.

data for erosion-corrosion rate. A small amount of measurement error in may cause significant error in calculating the erosion-corrosion rate. Therefore, in order to reduce the error percentage, great care was taken in repeated measurements of the degradation rates.

Initially, the effect of cold work on the repassivation behaviour was studied. Figure 4.8 shows the passivation curves of samples with different amounts of cold work applied to them in a stagnant aqueous solution for 900 seconds.

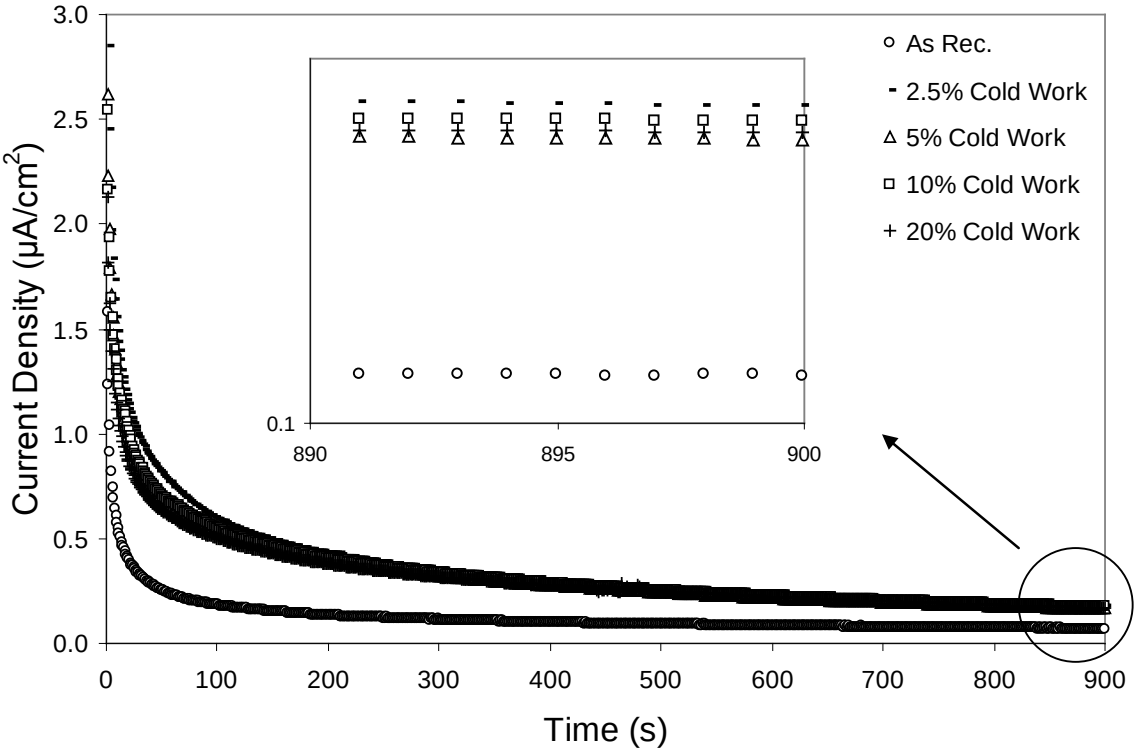

Figure 4-8 Passivation current density at 200mV (vs. SCE) in tap water solution as a function of time for samples with different amounts of cold work.

As shown in Figure 4.8, the initial application of cold work in the range of 2.5 % to 20 % increases both the repassivation time and current and thus promotes the corrosion rate of the surface; however, a further increase in the amount of cold work does not affect

F. Mohammadi and J.L. Luo, Corros. Sci., doi:10.1016/j.corsci.2010.09.059.

the repassivation behaviour of the surface any further. Many mechanisms can be mentioned that are responsible for the increase in corrosion rate upon cold working the samples. One simple explanation is that oxidation reactions on the surface occur when the metal ions move from preferred sites on the surface toward the solution. Some of these preferred sites that can be mentioned are grain boundaries, dislocations and surface imperfections, all of which are increased and altered by application of cold work to the samples.

In order to study the effect of cold work on the erosion-corrosion rate of the samples in a passive potential, W_t, the samples were held at 200 mV (vs. SCE) while the slurry was flowing on their surface. The effect of cold work on the erosion rate of the samples in a corrosion free condition, W_e^0, was studied by holding the samples at -850 mV (vs. SCE), which is in the cathodic region of the 304 stainless steel dynamic polarization curve. Figure 4.9 shows the effect of cold work on the erosion-corrosion rate of the samples at 200mV (vs. SCE). It is observed that the erosion-corrosion rate decreases with an increase in the amount of cold work; however, the extent of this decrease becomes much smaller as the applied cold work exceeds 5%.

Effect of cold work on the corrosion free erosion rate of the samples is also shown in Figure 4.9. It can be observed that by increasing the amount of applied cold work to the samples, the erosion rate decreases in the beginning; however, when the applied cold work reaches 5%, this effect becomes insignificant and no further decrease in the erosion rate of the samples is observed.

F. Mohammadi and J.L. Luo, Corros. Sci., doi:10.1016/j.corsci.2010.09.059.

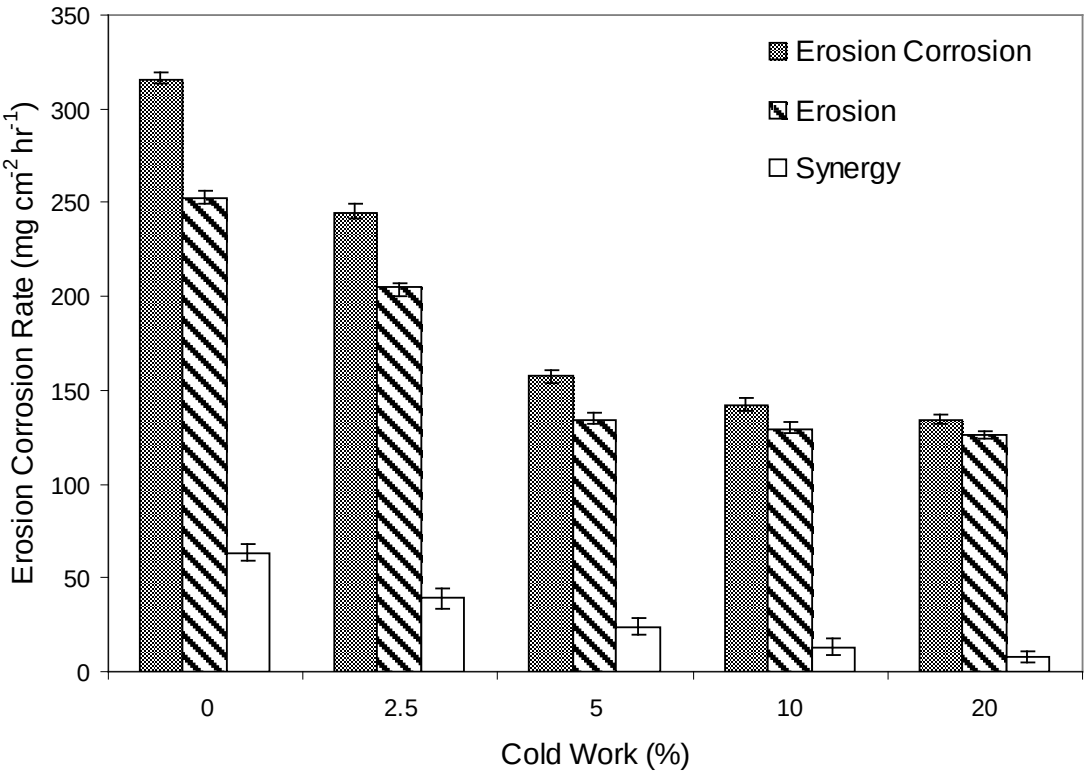

Figure 4-9 Erosion corrosion rate, pure erosion rate and the synergy contribution to erosion corrosion rate of 304 stainless steel with different applied cold work amounts.

The corrosion rate of the samples in an erosion free environment was calculated through the Faraday equation:

$$m = \frac{QM}{FZ} \qquad (4.7)$$

where *m* is the consumed mass of the substance, *Q* is the charge passed through the electrode, *M* is the molar mass of the substance, *F* is the Faraday constant, 96485 C/mol, and *Z* is the valence number of ions of the substance. Corrosion rate is increased by two simultaneous phenomena; one is the increase in the fluid velocity which is called flow induced corrosion and the other is the erosion itself. In order to separate these two effects, an experiment was performed and the results are shown in Figure 4.10 in which

F. Mohammadi and J.L. Luo, Corros. Sci., doi:10.1016/j.corsci.2010.09.059.

the as-received sample was passivated for the first 300 seconds in a stagnant solution. Once the 300 second mark was reached, the pump was turned on and the water flowed on the surface with 14 m/s velocity while the current was being recorded.

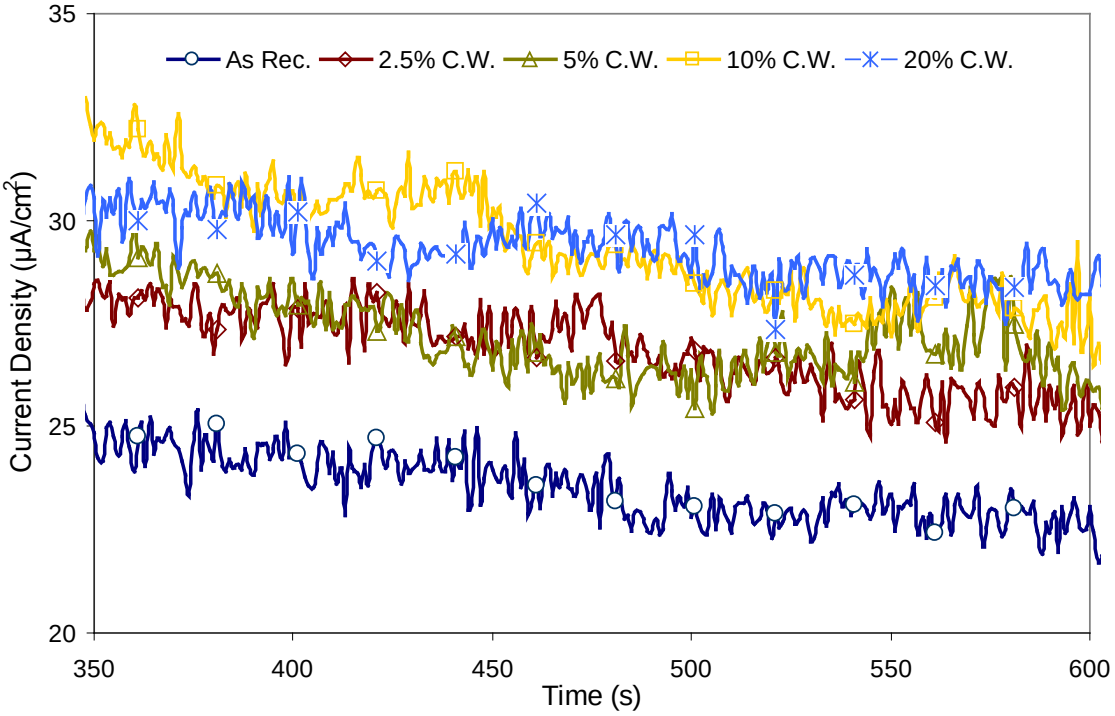

Figure 4-10 Passive current density of 304 stainless steels with different cold work amounts under flow of water with no sand at 14 m/s at 200 mV (SCE).

A stable current density of 22 µA/cm^2, observed between 350 s and 600 s in Figure 4.10, was used to calculate the values of W_c^0 through Equation 4.7. The calculations resulted in 0.015 mg cm^{-2} hr^{-1} corrosion rate on the surface in the absence of erosion, W_c^0. This is a low rate since the 200 mV (vs. SCE) potential that the samples were held at during the experiments is in the passive region of 304 stainless steel. According to Figure 4.10 the corrosion rate of different samples does not change significantly with cold work, and since the pure corrosion rate is very small compared to the other three damage rates

F. Mohammadi and J.L. Luo, Corros. Sci., doi:10.1016/j.corsci.2010.09.059.

shown in Equation 4.5, this rate was used for all the samples with different applied cold works. Since the corrosion rate is much smaller than erosion and erosion-corrosion rates, it cannot be seen in Figure 4.9; however, its amount was considered in the calculation of the synergy contribution shown in Figure 4.9.

In order to investigate the synergism of erosion and corrosion, the effect of cold work on the erosion enhanced corrosion rate of 304 stainless steel, W_c^e, was measured at various flow rates and the results are shown in Figure 4.11.

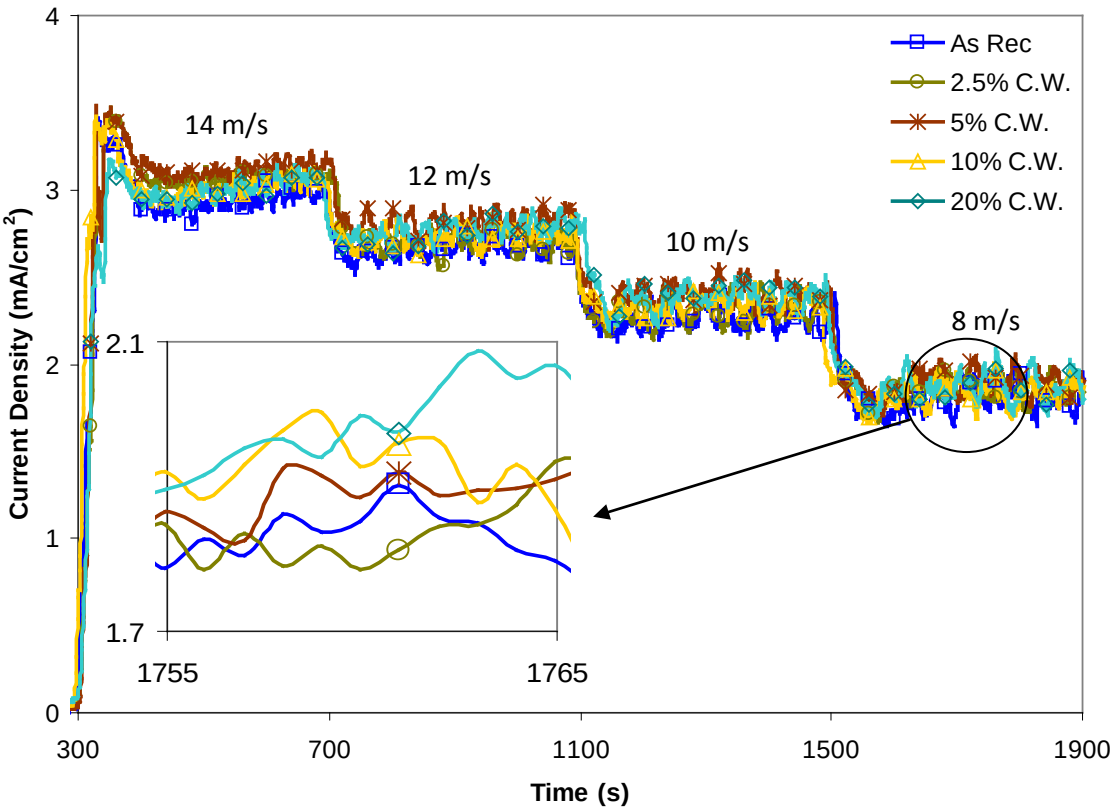

Figure 4-11 Current densities of stainless steels with different amount of cold work under flow of slurry at different velocities at 200 mV (SCE).

It can be seen that the recorded currents for all the samples with different amounts of applied cold work are almost identical at each impact velocity. These results are

F. Mohammadi and J.L. Luo, Corros. Sci., doi:10.1016/j.corsci.2010.09.059.

different from what was observed in Figure 4.4 in the case of single particle impacts. Single particle impact experiments showed that increasing the amount of cold work decreases the magnitude of current transients. Since slurry erosion is the sum of many sand particle impacts, a significant difference in the recorded currents was expected in Figure 4.11; however, these currents are almost the same. This phenomenon may be due to the effect of work hardening that is caused by multiple sand particle impacts during the slurry erosion. Regardless of the amount of cold work that is initially applied to the samples and acknowledging the fact that the samples are all made of the same material with the same work hardening ability, the work hardening characteristics of the surface layer of the samples (corrosion only affects this layer) become identical after the very first few seconds of slurry impact. This is due to the work hardening effect during the slurry erosion-corrosion, which also has been previously reported by other researchers [22]. The erosion enhanced corrosion rate of all the samples at 14m/s impact velocity was calculated through Equation 4.7 and Figure 4.11 and it was 2.04 mg cm^{-2} hr^{-1}.

Figure 4.12 shows the second component of the synergistic action of erosion and corrosion, the corrosion enhanced erosion, W_e^c. This part of the damage was calculated by deducting the sum of all other three damages from the total damage. According to Figure 4.12, the contribution of corrosion in enhancing the erosion rate of 304 stainless steel is also decreased by increasing the extent of the cold work applied to the samples. Hardness is representative of a material's mechanical properties. Normally, harder materials have higher yield stresses. In erosion-corrosion applications, harder materials

F. Mohammadi and J.L. Luo, Corros. Sci., doi:10.1016/j.corsci.2010.09.059.

which are ductile are preferred since they provide a combination of strength and formability, which enhances their properties for the service. According to the platelet mechanism [23], accumulation of strain in the roots of platelets formed due to multiple particle impacts results in their final detachment from the surface; therefore, it is important that the material can handle more deformation so that the detachment of the platelets requires more impacts. However, formation of the platelets is dependent on the material's strength in the first place. A harder material needs more energy to be deformed and platelets are more difficult to produce. In the case of cold rolled 304 stainless steel, the hardness and the strength of a ductile material are increased; therefore, the material's resistance to erosion-corrosion is increased.

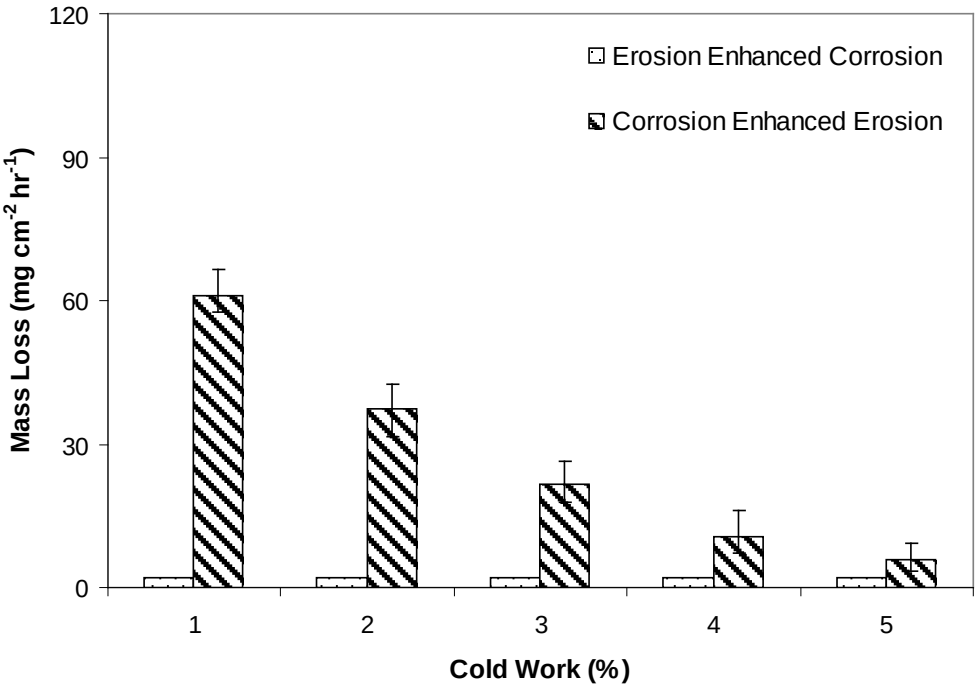

Figure 4-12 Mass loss rate of 304 stainless steel due to different synergistic actions of erosion and corrosion as a function of cold work percentage.

F. Mohammadi and J.L. Luo, Corros. Sci., doi:10.1016/j.corsci.2010.09.059.

The effect of velocity of the slurry on erosion-corrosion rate of 304 stainless steel was studied by performing more experiments at different velocities ranging from 5m/s to 14 m/s on the as-received samples (Figure 4.13). It is observed that an increase in the velocity of the slurry results in an increase in the erosion-corrosion rate of the material. However, the weight loss increase with velocity shows a semi-linear shape meaning that the weight loss due to erosion-corrosion changes in a somewhat linear manner with the kinetic energy of the particles floating in the slurry in the velocity range studied.

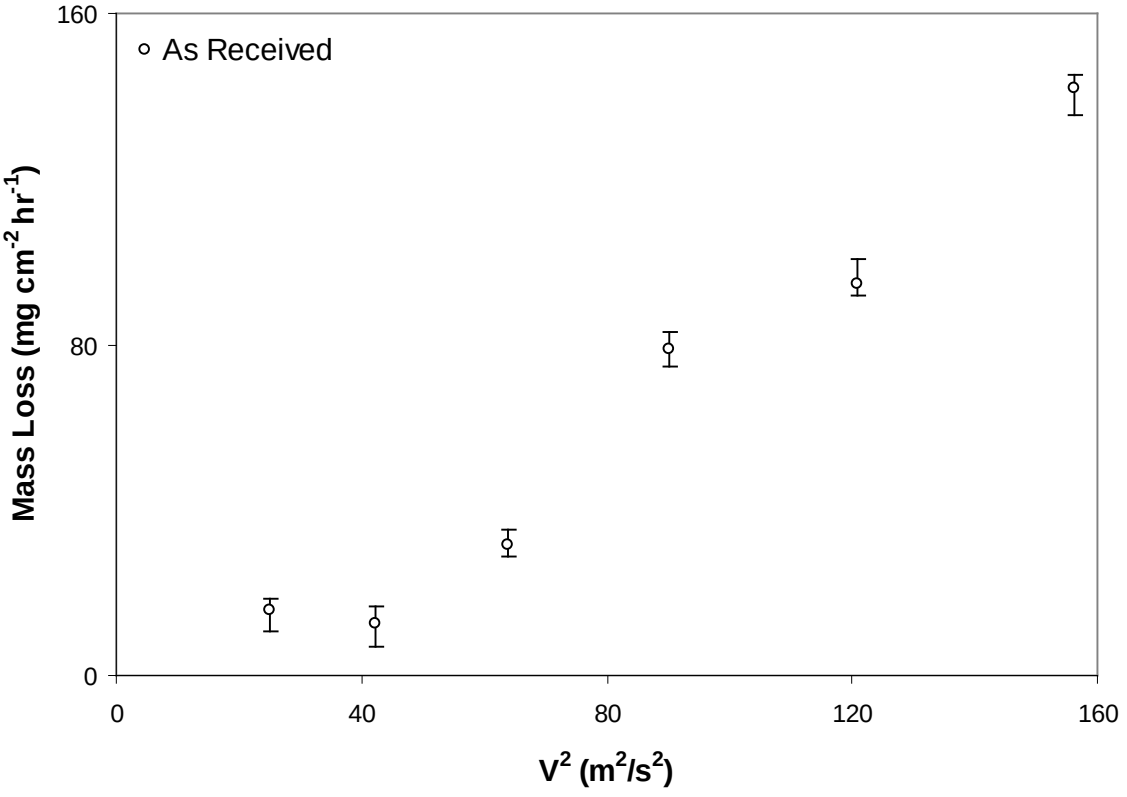

Figure 4-13 Erosion corrosion rate of 304 stainless steel as a function of slurry velocity.

It can be concluded that since the overall rate of corrosion of 304 stainless steel in the passive potential region is very low, its contribution to erosion-corrosion is not significant for softer materials where the erosion rates are significantly higher; however,

F. Mohammadi and J.L. Luo, Corros. Sci., doi:10.1016/j.corsci.2010.09.059.

for harder materials, the role of erosion enhanced corrosion becomes more pronounced as it covers 33% of the synergistic damage that is caused on the surface of the sample with 20% cold work (Figure 4.12).

4.4 Conclusions

(1) Specific energy of crater formation for 304 stainless steel was calculated and it was shown that this energy is a constant at each percentage of cold work that is applied to the material.

(2) It was found that the coefficient of friction between the surface and the impacting particle remains unchanged after application of different percentages of cold work to the sample.

(3) For materials with different amounts of cold work, the difference between the magnitudes of the current transients is a function of the difference in the length of the effective path of action for the friction force.

(4) Erosion enhanced corrosion rate of 304 stainless steel subject to the flow of water-sand slurry does not depend on the hardness of the steel, which may be due to the work hardening effect of the slurry on the surface.

4.5 References

[1] R.J.K. Wood, Erosion–corrosion interactions and their effect on marine and offshore materials, Wear 261 (2006) 1012-1023.

F. Mohammadi and J.L. Luo, Corros. Sci., doi:10.1016/j.corsci.2010.09.059.

[2] J.G. Chacon Nava, F.H. Stott and M.M. Stack, The effect of substrate hardness on the erosion-corrosion resistance of materials in low-velocity conditions, Corros. Sci. 35 (1993) 1045-1051.

[3] X. Hu and A. Neville, The electrochemical response of stainless steels in liquid solid impingement, Wear 258 (2005) 641–648.

[4] G.T. Burstein and K. Sasaki, Effect of impact angle on the slurry erosion–corrosion of 304L stainless steel, Wear 240 (2000) 80-94.

[5] P. Novak and A. Macenauer, Erosion-corrosion of passive metals by solid particles, Corros. Sci. 35 (1993) 635-640.

[6] K. Sasaki and G.T. Burstein, Erosion–corrosion of stainless steel under impingement by a fluid jet, Corros. Sci. 49 (2007) 92-102.

[7] A.W. Hassel and A. J. Smith, Single particle impact experiments for studying particle induced flow corrosion, Corros. Sci. 49 (2007) 231–239.

[8] F. Mohammadi, J. Luo, B. Lu and A. Afacan, Single particle impingement current transients for prediction of erosion-enhanced corrosion on 304 stainless steel, Corros. Sci. 52 (2010) 2331-2340.

[9] G.T. Burstein and K. Sasaki, Detecting electrochemical transients generated by erosion–corrosion, Electrochim. Acta 46 (2001) 3675–3683.

[10] F. Mohammadi and J. Luo, Effects of particle angular velocity and friction force on erosion enhanced corrosion of 304 stainless steel, Corros. Sci. (2010), doi:10.1016/j.corsci.2010.05.012.

F. Mohammadi and J.L. Luo, Corros. Sci., doi:10.1016/j.corsci.2010.09.059.

[11] H. McI. Clark, H. M. Hawthorne and Y. Xie, Wear rates and specific energies of some ceramic, cermet and metallic coatings determined in the Coriolis erosion tester, Wear 233-235 (1999) 319-327.

[12] I. Kleis and P. Kulu, Solid particle erosion: occurrence, prediction and control, Springer-Verlag, London, 2008.

[13] Sh. Endo and M. Nagae, Ferrite-Martensite dual phase anti-erosion steel, ISIJ Int. 36 (1996) 95-100.

[14] Q.L. Wang, Wear resistance of steels under wet abrasive erosion conditions, Wear 112 (1986) 207-216.

[15] X. Peng, J. Yan, Z. Dong, C. Xu and F. Wang, Discontinuous oxidation and erosion-oxidation of a CeO_2-dispersion-strengthened chromium coating, Corros. Sci. 52 (2010) 1863-1873.

[16] S. Matthews, B. James and M. Hyland, Erosion of oxide scales formed on Cr_3C_2–NiCr thermal spray coatings, Corros. Sci. 50 (2008) 3087-3094.

[17] J. Xu, Ch. Zhuo, D. Han, J. Tao, L. Liu and Sh. Jiang, Erosion–corrosion behaviour of nano-particle-reinforced Ni matrix composite alloying layer by duplex surface treatment in aqueous slurry environment, Corros. Sci. 51 (2009) 1055-1068.

[18] A.W. Hassel and A. J. Smith, Single particle impact experiments for studying particle induced flow corrosion, Corros. Sci. 49 (2007) 231–239.

[19] M. Raoa, J. Keisera, A. V. Levy and W. Buqianb, Mechanical behaviour of erosion-corrosion scales on steels as characterized by single-particle impacts, Wear 150 (1991) 135-152.

F. Mohammadi and J.L. Luo, Corros. Sci., doi:10.1016/j.corsci.2010.09.059.

[20] B.T. Lu, J.L. Luo, F. Mohammadi, K.Wang and X.M.Wan, Correlation between repassivation kinetics and corrosion rate over a passive surface in flowing slurry, Electrochim. Acta 53 (2008) 7022–7031.

[21] A.H. Kharaz, D. A. Gorham and A. D. Salman, An experimental study of the elastic rebound of spheres, Powder Technol. 120 (2001) 281-291.

[22] J. Salik and. Buckley, Effect of mechanical surface and heat treatments on erosion resistance, Proc. Int. Conf. Wear of Mater. ASME, San Francisco (1981).

[23] A.V. Levy, Solid Particle Erosion and Erosion-corrosion of materials, ASM international, Materials Park, Ohio, 1995.

F. Mohammadi and J.L. Luo, Corros. Sci., doi:10.1016/j.corsci.2010.09.059.

5 General discussion and future work recommendations

Studying the particle-surface interactions during slurry erosion-corrosion in order to have a better understanding of the erosion-corrosion mechanism was the main objective of this research study. Another objective was to be able to use single particle-surface interactions to predict the overall material response in erosive corrosive conditions. Finally, it was aimed to use the basic understanding obtained of the particle-surface interactions to study the effect of cold work on erosion-corrosion of materials.

In order to perform the single particle impingement tests, a new device was designed and constructed based on Finnie's calculations for the velocity of a spherical particle that is introduced to a flow [1]. Using this device, it was possible to impinge single particles with diameters up to 3mm while the impact angle and velocity could be changed as well as the medium (Figure 2.1). For a better observation of the particle-surface interactions, a high speed camera was coupled with this system. Also a three electrode potentiostat was attached to the system to simultaneously study the electrochemical response of the surface to single particle impacts. In order to simulate the actual service condition, a slurry jet impingement device was used, which was capable of impinging slurry at different velocities up to 30 m/s at different impact angles from 0^{o} to 90^{o}.

Preliminary studies of the single impacts of zirconia, silicon nitride and glass particles on the surface showed that the produced current transients had a maximum height at 30^{o} impact angle.

Further observations of the single particle impact velocity along with the study of the craters formed on the surface by these impacts revealed that in the velocity range between 5m/s and 11m/s, the volume of the craters is linearly correlated with the kinetic energy of the impacting particles. It was also found that in this range of impact velocity where previous erosion theories do not predict any material removal from the surface [2], some parts of the passive film are removed from the surface of the material and depassivation of the surface occurs. A comparison between the charge required for repassivation and the crater volume showed their linear correlations with each other and the impacting particle kinetic energy. It was shown that at 30° impact angle, the ratio of the depassivated surface area to the total surface area of the crater, α_{s30}, was 0.3, which means that 33% of the crater surface area was depassivated at this impact angle.

Furthermore, the charge required for repassivation of the surface due to single particle impacts were used to predict the erosion enhanced corrosion rate of the surface in a slurry. Predictions were accurate at sand concentrations up to 1 wt% where the inter-particle interactions were negligible and impacting and rebounding particles did not interfere with each other.

To further study the mechanism of impact and interactions between particle and surface during impact, the coefficient of restitution, *e*, was used as defined earlier by other researchers [3-5]. Coefficient of restitution is the ratio of the rebound velocity to impact velocity and is representative of the amount of energy that is dissipated during the impact. The experimental results showed that the coefficient of restitution in the

normal direction decreases with increasing the impact angle. It was found that the tangential coefficient of restitution also decreases with increasing the impact angle up to 60º and then increases towards normal impact angles. However, the trans ferred angular velocity to the particles is maximum at 60º impact angle. Coefficient of friction between the two surfaces was calculated from the coefficients of restitution and a value of 0.22 was defined for the coefficient of friction between the zirconia particles and 304 stainless steel. Pre-impact angular velocity of the spherical particles was experimentally measured and showed not to have a significant effect on the extent of depassivation of the surface of 304 stainless steel.

Consequently, average normal and tangential forces were assumed to be acting on the surface during the impact. It was proposed that the friction force between the two surfaces is mostly responsible for the depassivation of the surface. Also it was shown that the path that the friction force acts along the surface is important and affects the extent of depassivation of the surface. Based on these observations a mechanism was proposed for the depassivation of the surface during impact. In the proposed mechanism average normal and tangential forces are assumed to act along the surface during the impact. It is shown that the erosion enhanced corrosion rate of 304 stainless steel depends on both the magnitude of the average tangential force and the effective path that it acts along the surface during the impact.

Different amounts of cold work were applied to samples of 304 stainless steel to study its erosion-corrosion properties. It was found that the coefficient of friction between the zirconia particles and 304 stainless steel remained constant regardless of

the amount of cold work that was applied to the samples. However, cold work increased the amount of specific energy of crater formation on the surface. Specific energy for crater formation is defined as the ratio of the initial kinetic energy of the impacting particle to the crater volume.

Single impingement experiments revealed that the current transient heights decrease by increasing the amount of cold work applied to the samples. This indicated a decrease in the erosion enhanced corrosion of the surface during slurry flow. However, mass loss measurements showed that this effect is insignificant where slurry flows on the surface, which is due to the work hardening of the surface, and erosion enhanced corrosion of all the samples is almost equal. Mass loss experiments also showed that all of the erosion, corrosion and synergy rates decrease by increasing the amount of cold work applied to the samples. However, the effect of cold work on the corrosion enhanced erosion is more pronounced than other parameters. It was also found that the erosion-corrosion rate of 304 stainless steel is linearly correlated to the kinetic energy of the flowing slurry.

In summary, a basic understanding of the particle-surface interactions during slurry flow was obtained in this study. The mechanism of surface depassivation of 304 stainless steel and the factors affecting it were investigated. The effect of cold work on the erosion-corrosion rate of 304 stainless steel was investigated with specific attention to the friction force. These results will help future research in the field of erosion-corrosion move in a new direction by considering kinetic energy and friction force as two important factors that affect erosion-corrosion rate.

5.1 Future work recommendations

Based on the findings of the present work, the following subjects can be recommended in particular for further studies:

- Since one of the main conclusions of this study was that the friction force and its effective path of action on the surface are two important factors that affect the extent of depassivation of the surface:
    1. Further studies are required to investigate the depassivation mechanism from different points of view and perspectives. Also more experimental results will be beneficial for the evaluation of this mechanism. More accurate calculations of the average normal and tangential forces are possible through averaging both the normal force and the depth of the scar.
    2. Several compounds can be added to the solution to reduce the coefficient of friction between the surfaces without significantly affecting other hydrodynamic properties of the solution. This can be further studied to reduce the erosion-corrosion rate of materials.
- The proposed model for prediction of erosion enhanced corrosion of 304 stainless steel provided good predictions in lower sand concentrations where the inter-particle interactions were not significant. This model can be further modified so that it accounts for these interactions and provides more accurate predictions.

- Cold work was used to increase the hardness of the material and it was shown to improve the erosion-corrosion properties of 304 stainless steel. Application of hard coatings can be the subject of a new study in order to increase the surface hardness and improve the erosion-corrosion resistance.
- Nano-indentation studies of different spots of the crater area can be performed in order to determine the change in hardness and its correlation with the kinetic energy of impact and its effect on the erosion-corrosion rate.

Moreover and in general, inasmuch as there is still no successful model to predict the erosion-corrosion rate of the materials, research work to study and develop such a model is required.

5.2 References

[1] I. Finnie, Erosion of surfaces by solid particles, Wear 3 (1960) 87-103.

[2] I.M. Hutchings, Particle erosion of ductile metals: A mechanism of material removal, Wear 27 (1974)121-128.

[3] L-Y. Li, C-Y. Wu and C. Thornton, A theoretical model for the contact of elastoplastic bodies, J. Mech. Eng. Sci. 216 (2002) 421-431.

[4] C-Y. Wu, C. Thornton and L-Y. Li, A semi-analytical model for oblique impacts of elastoplastic spheres, Proc. R. Soc. London, Ser. A 465 (2009) 937-960.

[5] C-Y. Wu, L-Y. Li and C. Thornton, Rebound behaviour of spheres for plastic impacts, Int. J. Impact Eng. 28 (2003) 929-946.

6 Appendix A

```
'''''''''''''''''''''''' Newton Raphson ''''''''''''''''''''''''''''

Const delta = 0.00000000001

Const t0 = 1                    'Initial Guess

Function f(t, x, k, u)

   f = x - (k * u * t - Log(1 + k * u * t)) / k

End Function

Function d(t, x, k, u)

   d = (f(t + delta, x, k, u) - f(t, x, k, u)) / delta

End Function

Function nr(x, k, u)

   t = t0

   Do While Abs(f(t, x, k, u)) > delta

      t = t - f(t, x, k, u) / d(t, x, k, u)

   Loop

   nr = t

End Function
''''''''''''''''''''''''''''''''''''''''''''''''''''''''''''''''''''''''''''

Sub main()

   V = Cells(2, 2)        'Particle Velocity

   u = Cells(3, 2)        'Fluid Velocity

   DD = Cells(4, 2)       'Pipe diameter

   For x = 0 To Cells(6, 2) Step Cells(1, 2)

      Re = Abs(V - u) * Cells(8, 2) * Cells(9, 2) / Cells(10, 2)

      CD = 24 / Re * (1 + 0.197 * Re ^ 0.63 + 0.00026 * Re ^ 1.38)

      k = 3 * CD * Cells(8, 2) / 4 / Cells(7, 2) / Cells(9, 2)

      t = nr(x, k, u)

      V = k * u ^ 2 * t / (1 + k * u * t)

      DD2 = Cells(4, 2) - (Cells(4, 2) - Cells(5, 2)) / Cells(6, 2) * x
```

```
    u = u * DD ^ 2 / DD2 ^ 2
    DD = DD2
  Next x
  Cells(1, 5) = V
  Cells(2, 5) = u
End Sub

Sub main2()
j = 0
For i = 0.07 To 0.6 Step 0.01
  j = j + 1
  V = Cells(2, 2)       'Particle Velocity
  u = Cells(3, 2)       'Fluid Velocity
  DD = Cells(4, 2)      'Pipe diameter
  For x = 0 To i Step Cells(1, 2)
    Re = Abs(V - u) * Cells(8, 2) * Cells(9, 2) / Cells(10, 2)
    CD = 24 / Re * (1 + 0.197 * Re ^ 0.63 + 0.00026 * Re ^ 1.38)
    k = 3 * CD * Cells(8, 2) / 4 / Cells(7, 2) / Cells(9, 2)
    t = nr(x, k, u)
    V = k * u ^ 2 * t / (1 + k * u * t)
    DD2 = Cells(4, 2) - (Cells(4, 2) - Cells(5, 2)) / i * x
    u = u * DD ^ 2 / DD2 ^ 2
    DD = DD2
  Next x
  Cells(1 + j, 7) = i
  Cells(1 + j, 8) = V
  Cells(1 + j, 9) = u
Next i
End Sub
```

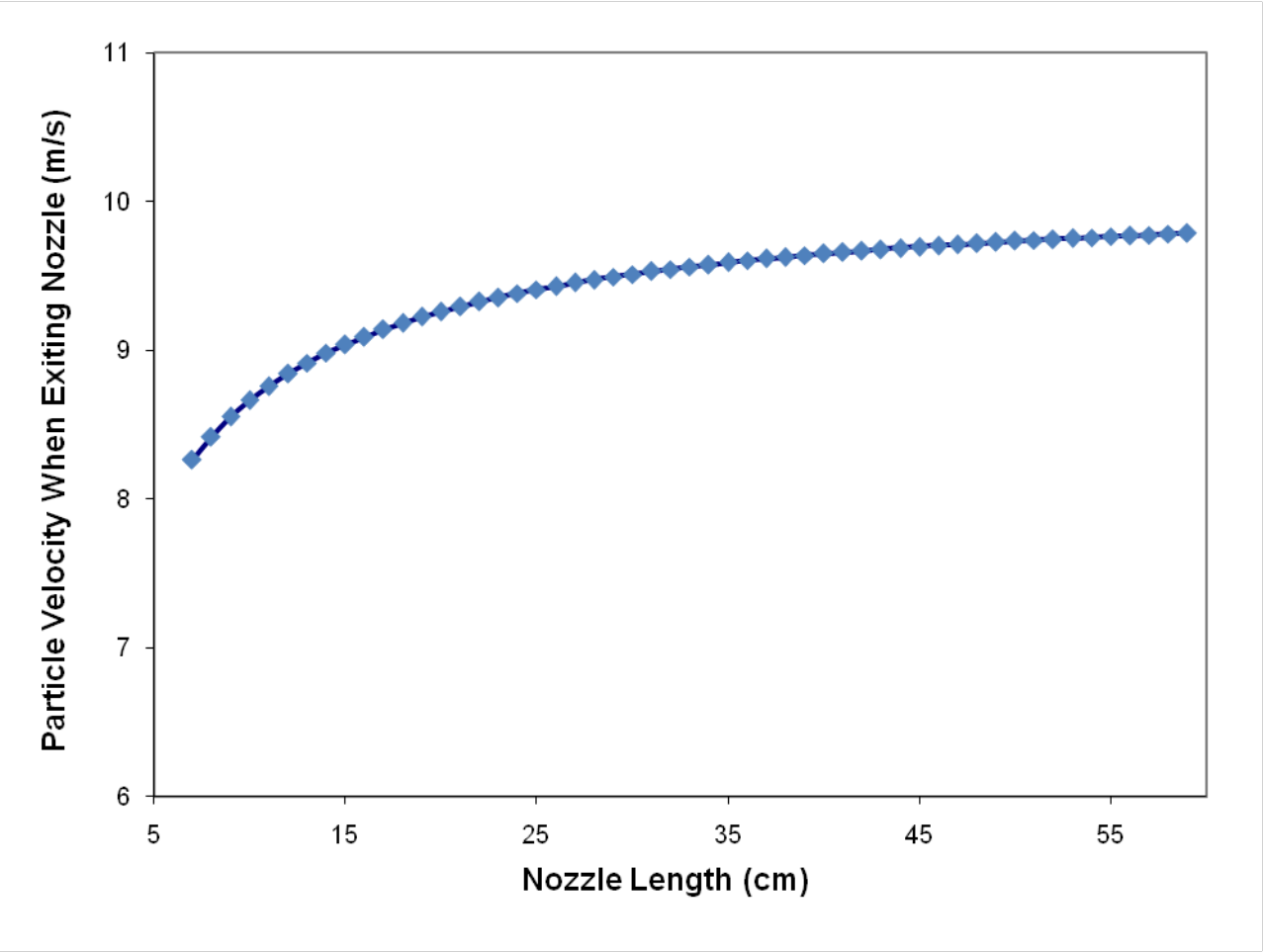

Figure 6-1 Theoretical prediction of the dependence of the velocity of a 2.38 mm zirconia particle on the nozzle length when exiting the nozzle (water velocity at the nozzle exit is 10 m/s, diameter at nozzle entrance is1/2" and diameter at nozzle exit is 1/8").